Experimental Validation of a Mixed-Flow Compressor Impeller and Cross-over Diffuser

by

Pieter Coenraad Swanepoel

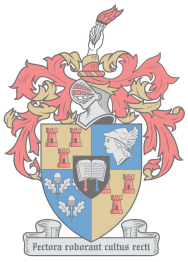

Thesis presented in partial fulfilment of the requirements for the degree of Master of Engineering (Mechanical) in the Faculty of Engineering at Stellenbosch University

Supervisor: Prof. S.J. van der Spuy
Co-supervisor: Prof. T.W. von Backström

December 2018

Declaration

By submitting this thesis electronically, I declare that the entirety of the work contained therein is my own, original work, that I am the sole author thereof (save to the extent explicitly otherwise stated), that reproduction and publication thereof by Stellenbosch University will not infringe any third party rights and that I have not previously in its entirety or in part submitted it for obtaining any qualification.

Date: December 2018

UNIVERSITEIT•STELLENBOSCH•UNIVERSITY
jou kennisvennoot • your knowledge partner

Plagiaatverklaring / Plagiarism *Declaration*

1 Plagiaat is die oorneem en gebruik van die idees, materiaal en ander intellektuele eiendom van ander persone asof dit jou eie werk is.
Plagiarism is the use of ideas, material and other intellectual property of another's work and to present it as my own.

2 Ek erken dat die pleeg van plagiaat 'n strafbare oortreding is aangesien dit 'n vorm van diefstal is.
I agree that plagiarism is a punishable offence because it constitutes theft.

3 Ek verstaan ook dat direkte vertalings plagiaat is.
I also understand that direct translations are plagiarism.

4 Dienooreenkomstig is alle aanhalings en bydraes vanuit enige bron (ingesluit die internet) volledig verwys (erken). Ek erken dat die woordelikse aanhaal van teks sonder aanhalingstekens (selfs al word die bron volledig erken) plagiaat is.
Accordingly all quotations and contributions from any source whatsoever (including the internet) have been cited fully. I understand that the reproduction of text without quotation marks (even when the source is cited) is plagiarism.

5 Ek verklaar dat die werk in hierdie skryfstuk vervat, behalwe waar anders aangedui, my eie oorspronklike werk is en dat ek dit nie vantevore in die geheel of gedeeltelik ingehandig het vir bepunting in hierdie module/werkstuk of 'n ander module/werkstuk nie.
I declare that the work contained in this assignment, except where otherwise stated, is my original work and that I have not previously (in its entirety or in part) submitted it for grading in this module/assignment or another module/assignment.

16622766 **Studentenommer / *Student number***	**Handtekening / *Signature***
P.C. Swanepoel **Voorletters en van / *Initials and surname***	2018/12/14 **Datum / *Date***

Abstract

Experimental Validation of a Mixed-Flow Compressor Impeller and Cross-over Diffuser

P.C. Swanepoel

Department of Mechanical and Mechatronic Engineering,
University of Stellenbosch,
Private Bag X1, Matieland 7602, South Africa.

Thesis: MEng (Mech)

December 2018

In the past decade Stellenbosch University has been actively involved in the development of components for Micro-gas turbines (MGTs). MGTs are particularly attractive to the energy and defence sector due to their high thrust-to-weight ratio and thus relatively high power output. The use of a mixed-flow compressor impeller is attractive for MGTs due to its mass flow vs pressure ratio characteristics. Previous researchers optimised and manufactured a mixed-flow compressor impeller and cross-over diffuser for this specific reason. The goal of this thesis is to experimentally validate the numerical predictions made for the compressor stage with the computational fluid dynamics (CFD) code NUMECA. Experimental tests were conducted with a compressor test bench in the Gas Dynamics Laboratory at Stellenbosch University. The air receiver capacity limited the operational speed of the facility to 50 000 rpm. The performance of the impeller is evaluated numerically and experimentally with both a cross-over and vaneless diffuser. The effect of trailing edge blade tip clearance on the performance of the impeller is also investigated numerically and experimentally. The assembly of the test bench allowed for design modifications to be made to the shaft, bearing housing, split ring spacer and bearing layout. The modifications proved beneficial as experimental tests were conducted successfully at 50 000 rpm. The experimental results agreed well with the numerical results with the vaneless diffuser assembly delivering a total-to-total pressure ratio of 1.57 with an efficiency of 71.0% at a mass flow rate of 0.26 kg/s. The cross-over diffuser assembly delivered a total-to-total pressure ratio of 1.63 with an efficiency of 76.3% at a mass flow rate of 0.3 kg/s. The effect of blade tip clearance on the impeller's performance was notable with the

cross-over diffuser assembly but could not be observed with the vaneless diffuser assembly. A trailing edge blade tip clearance of 0.2 mm was also achieved experimentally and proved to be feasible.

Uittreksel

Experimentele Validasie van 'n Gemengde Vloei Kompressor Stuwer en Oorgangsdifussor

(Experimental Validation of a Mixed-Flow Compressor Impeller and Cross-over Diffuser)

P.C. Swanepoel

Departement Meganiese en Megatroniese Ingenieurswese,
Universiteit van Stellenbosch,
Privaatsak X1, Matieland 7602, Suid Afrika.

Tesis: MIng (Meg)

Desember 2018

Deur die loop van die laaste dekade was die Universiteit van Stellenbosch betrokke by die ontwikkeling van komponente vir Mikro-Gas turbines (MGTs). MGTs is besonder aantreklik vir die Energie- en Verdedigingsektore a.g.v. hulle hoë energiedigtheid-teenoor-massa verhouding. Die gebruik van 'n gemengde vloei kompressor stuwer word aantreklik gevind vir applikasie in MGTs oor hul hoë drukverhouding karakter eienskappe. Vorige studente het om die rede onderskeidelik 'n gemengde vloei kompressorstuwer en oorgangsdiffusor ontwerp en vervaardig. Die doel van die tesis is om die numeriese voorpellings wat deur die Numeriese Vloei Dinamika (NVD) pakket NUMECA voorspel is eksperimenteel te bevestig. The eksperimentele toetse was gedoen op 'n kompressor toetsbank in die Gas Dinamika Labortorium by die Universiteit van Stellenbosch. Die lug voorsienings tenk het 'n beperkte kapasiteit en dus was die maksimum toets-spoed 50 000 opm. Die werksverigting en benuttingsgraad van die stuwer word numeries en eksperimenteel ge-evalueer met 'n oorgangs en 'n oop-kanaal diffusor. Die effek van lempuntspeling op die werksverigting en benuttinggraad van die kompressor word numeries en eksperimenteel ondersoek. Veranderinge aan die as, laer-huis, ring-spasie houer en laer uitleg was ook toegelaat. Die eperimente was suksesvol voltooi by 50 000 opm en dus het die ontwerp gebaat by die veranderinge. Die eksperimentele resultate stem goed ooreen met die numeriese resultate met die oop-kanaal diffusor opstelling wat n totaal-tot-totaal drukverhouding van 1.57 met 'n benuttingsgraad van 71% by 'n massavloei van 0.26 kg/s gelewer het. Die oorgangsdiffusor opstel-

ling het n totaal-tot-totaal drukverhouding van 1.63 met 'n benuttingsgraad van 76% by 'n massavloei van 0.3 kg/s gelewer. Daar was n beduidende effek op die stuwer se benuttingsgraad a.g.v. die verandering in lempuntspeling waarneembaar by die oorgangsdiffusor opstelling, maar die effek was nie waarneembaar by die oop-kanaal diffusor opstelling nie. 'n Lempuntspeling van 0.2 mm was eksperimenteel behaal en bewys as haalbaar.

Acknowledgements

I would like to express my sincere gratitude to the following people and organisations:

- To my Lord and Saviour Jesus, Whom without I would not have been here today. By His grace he has granted me on one of life's best journeys, and unconditionally leads me with love and grace.
- Words cannot express the gratitude I have towards my church family, who unconditionally stayed by my side, and always encouraged me.
- To my supervisors Prof. S.J. van der Spuy and Prof. T.W. von Backström for all their support and guidance in helping me to achieve one of my life goals.
- The CSIR and ARMSCOR for funding this project, which forms part of the CONVERGE project.
- All the workshop personnel who assisted me in manufacturing the test bench parts and doing it with pleasure.
- Susan van der Spuy who helped me to deal with international imports and to ensure the on-time delivery of components.
- A big thank you to my colleagues Mr. Jean-Gerard de la Bat, Mr. Ruan Engelbrecht and Mr. Preston Kock who were always willing to help and give advice.

Dedications

Hierdie tesis word opgedra aan my ouers; Coenie en Thea Swanepoel. Woorde is nie genoeg om die dankbaarheid te beskruif wat ek het teenoor julle ondersteuning, raad, insig en liefde het nie. Deur julle het ek deursetingsvermoë, disipline en wysheid geleer. Dankie vir wie julle vir ons is.

Contents

List of Figures

List of Tables

Nomenclature

Symboles

A	Area	$[\mathrm{m}^2]$
a	Sonic velocity	$[\mathrm{m/s}]$
B_{max}	Shannon-Nyquist sampling frequency	$[\mathrm{Hz}]$
b	Blade Height	$[\mathrm{mm}]$
C_d	Coefficient of discharge	$[\_]$
C_p	Specific heat at constant pressure	$[\mathrm{J/kg.K}]$
c	Absolute velocity	$[\mathrm{m/s}]$
D	Diameter of Large pipe	$[\mathrm{m}]$
d	Diameter of small pipe	$[\mathrm{m}^2]$
f	Friction factor	$[\_]$
f_s	Sampling frequency	$[\mathrm{Hz}]$
H	Compressor Head, actual or isentropic	$[\_]$
h	Specific enthalpy	$[\mathrm{J/kg}]$
i	Sample number	$[\_]$
k	Measurement number	$[\_]$
K	Dynamic correction factor	$[\_]$
L	Pipe length	$[\mathrm{m}]$
Ma	Mach number	$[\_]$
m	Meridional length	$[\_]$
$\dot{m}$	Mass flow rate	$[\mathrm{kg/s}]$
N	Rotational Speed	$[\mathrm{rpm}]$
n	Measurement samples	$[\_]$
P	Power	$[\mathrm{W}]$
$P_{s/t}$	Pressure	$[\mathrm{Pa}]$
PR	Pressure ratio	$[\_]$
R	Gas constant	$[\mathrm{J/kg.K}]$
Re_d	Reynolds number	$[\_]$
r	Radius	$[\mathrm{m}]$

Q	Flow rate	$[\mathrm{m}^3/s]$
s	Entrpy	$[\mathrm{J/kg.K}]$
T	Temperature	$[\mathrm{K}]$
U	Blade speed, ωr	$[\mathrm{m/s}]$
w	Relative velocity	$[\mathrm{m/s}]$
W	Specific work transfer	$[\_]$
y^+	Non-dimensional wall quantity	$[\mathrm{m}]$
Z	Blade count	$[\_]$

Greek Symbols

α	Fluid relative flow angle	$[\mathrm{rad}]$
Ω	Flow coefficient	$[\_]$
β	Relative flow angle	$[\mathrm{rad}]$
$\frac{D_1}{D_2}$	Diameter ratio	$[\_]$
ϵ	Compressibility factor	$[\_]$
η	Efficiency	$[\_]$
γ	Ratio of specific heats	$[\_]$
θ	Blade chamber angle	$[\mathrm{rad}]$
μ	Dynamic viscosity	$[\mathrm{kg/m.s}]$
ν	Kinematic viscosity	$[\mathrm{m}^2/s]$
ρ	Density	$[\mathrm{kg/m}^3]$
σ	Slip factor	$[\_]$
ω	Rotational speed	$[\mathrm{rad/s}]$

Subscripts

0	Compressor inlet condition
1	Impeller Blade inlet condition
2	Impeller Blade outlet condition
3	Diffuser Blade outlet condition
4	Pressure measurement station
amb	Ambient condition
bm	Bellmouth
c	Compressor
d	Discharge side
p	Probe condition
o	Output

t	Total (Stagnation) thermodynamic condition
$t-t$	Total-to-total quantity
$t-s$	Total-to-static quantity
s	Static thermodynamic quantity
ss	Suction side
pm	Pressure measurement station
vo	Volute outlet
x, y, z	Cartesian coordinates

Superscripts

$'$	Blade angle
$\bar{}$	Average value
$\cdot$	Time rate of change
$*$	Critical/isentropic condition

Acronyms

ANSI	American National Standards Institute
ARMSCOR	Armaments Corporation of South Africa
ASME	American Society of Mechanical Engineers
BEP	Best efficiency point
BS	British standard
CAD	Computer Aided design
CD	Channel Diffuser
CFD	Computational Fluid Dynamics
COD	Cross-Over Diffuser
CPU	Central Processing Unit
cRIO	Compact Reconfigurable I/O
CSIR	Council for Scientific and Industrial Research
DAQ	Data Acquisition
FPGA	Field Programmable Gate Array
GUI	Graphical User Interface
ISO	International Standards Organisation
MGT	Micro Gas Turbine
SAAF	South African Air Force
SM	Surge Margin
TD	Turn Down
UAV	Unmanned Aerial Vehicle

Chapter 1

Introduction

1.1 Background

In the past decade Stellenbosch University has been actively involved in the development of components for Micro-gas turbines (MGTs). The CONVERGE project was initiated by the South African Air Force with the intent to develop the South African skills set involved in the research and development of gas turbine engines. MGTs are particularly attractive to the energy and defence sector due to their high thrust-to-weight ratio and thus relatively high power output. These engines are light-weight and fuel efficient and are well suited for portable power generation and propulsion for high altitude unmanned aerial vehicles (UAVs) (Vick, 2009). The latter application is particularly attractive due to the low altitude ceiling of conventional piston driven engines.

In order to achieve a high power-to-weight ratio it is necessary for MGTs to have a high mass flow rate, which motivates the use of a mixed-flow compressor (Diener, 2016). The project will set out to test and validate the mixed-flow compressor impeller optimised and manufactured by Diener (2016) as well as the optimised cross-over diffuser designed by Kock (2016). The impeller will be housed in its own custom-built housing for both the turbine and compressor, which is attached to the test bench designed by Struwig (2014).

1.2 Problem Statement

Diener (2016) optimised a mixed-flow compressor impeller for a design point mass flow rate of 0.86 kg/s at 95 000 rpm. The compressed air test facilities at Stellenbosch University is able to conveniently achieve a rotational speed of 50 000 rpm for the size of this particular design, using compressed air. Therefore the numerical results were simulated at 50 000 rpm at corresponding atmospheric conditions.

Due to the small blade tip clearance designed by Diener, emphasis is placed on assessing the effect of blade tip clearance on the performance of the impeller and to see if it is prodically possible to achieve the design point blade tip clearance of 0.2 mm.

With regards to the compressor test bench setup, emphasis is placed on implementing key components for the test bench, namely the bearing layout on the shaft, design tolerances on the shaft and bearing housing.

1.3 Objectives

In parallel with experiments, Computational Fluid Dynamic (CFD) simulations will be done using NUMECA to determine theoretical compressor curves for the impeller and diffuser design combinations. These CFD results will then be validated by running a series of experiments with each design combination. The objectives of this project are stipulated below:

- Assemble and conduct experimental analysis on the mixed-flow impeller and cross-over and vaneless diffuser design combinations.
- Validate CFD results using experimental results.
- Construct performance maps for the mixed-flow impeller with cross-over diffuser and vaneless diffuser combinations.
- Evaluate the effect of blade tip clearance on the performance of the impeller for both diffuser configurations.

1.4 Significance of Project

Experimental results will confirm which design combination w.r.t. blade tip clearance and diffuser configuration is the most efficient and subsequently the ideal solution for achieving the determined thrust specification of the MGT under consideration. The successful operation of the impeller with a 0.2 mm blade tip clearance will prove that the design is indeed feasible and that such fine tolerances can be achieved.

Chapter 2

Literature Overview

This chapter provides a brief overview of previous work done on the design and development of micro gas turbine components. Testing has been performed in the Gas Dynamics Laboratory at the Mechanical and Mechatronic Engineering Department. The test facility operates on cold compressed air that is expanded through a turbine to attain the desired rotational speeds (Struwig, 2014). A brief overview of the Impeller and Diffuser designs by Diener (2016) and Kock (2016) respectively is also included in this chapter.

2.1 Test Facility Specifications

The test bench is operated using compressed air at 1 MPa. The air is dehumidified through two parallel coupled air driers and stored in two separate tanks with a combined capacity of 88 m^3 (Struwig, 2014). The air is then fed directly from these tanks to the Gas Dynamics Laboratory through a main supply header. Multiple air supply points stem from this main supply header to the rest of the laboratory. The main supply header uses a manual ball valve to open and close the air supply to the laboratory. The layout of the test facility designed by Struwig (2014) is shown in Figure 2.1 below.

Leading up to the turbine, the air supply that branches from the main header reduces from 200 mm to 100 mm nominal bore. Another manually operated safety ball valve is included here. Downstream of this valve the flow is measured using an orifice plate. The air supply pipe is then further reduced from 100 mm to 50 mm nominal bore. This section accommodates a butterfly valve that is controlled via a gearbox and stepper motor to regulate the flow through the turbine using a micro controller designed by Struwig (2014). After the air has passed through the turbine it is expelled into the atmosphere via a conical diffuser.

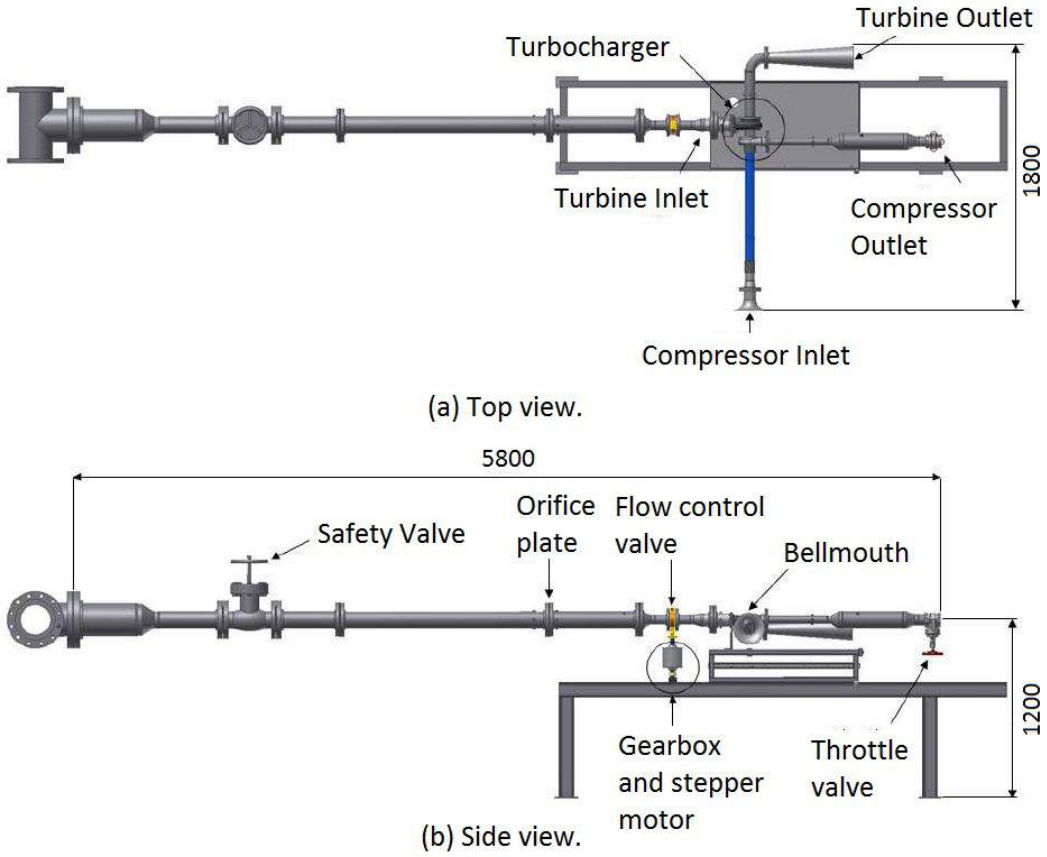

Figure 2.1: Test Facility Layout (Struwig, 2014)

The compressor is attached to the turbine section via a shaft and has a separate air flow path from the turbine section. The compressor designed by Diener (2016) is assembled having its own custom shroud that is attached to the back of the turbine shroud.

2.2 Mixed-flow Compressor Design

This section gives a brief overview of the operation of a mixed-flow compressor and the final details of the compressor designed by Diener (2016).

2.2.1 Compressor Theory

A centrifugal impeller increases the energy level of the fluid by expelling it radially outwards, thus increasing the angular momentum of the fluid (Dixon, 2005). To achieve the same pressure ratio in an axial flow compressor more rotor and stator stages are required, since the flow path remains axial and no

angular momentum is added to the fluid. Therefore in order to achieve the same pressure ratio, the length of an axial compressor is much greater than that of a radial compressor. The radial compressor stage however has a larger frontal area requirement than an axial compressor due to the inclusion of a radial diffuser downstream of the compressor. The diffuser affects a static pressure rise as it decelerates the flow, before the gas enters the combustion chamber (Diener, 2016).

Simpson (2012) optimized the endwalls of a centrifugal impeller to reduce the impeller diffusion ratio. Simpson followed the Design of Experiments (DOE) approach to build a database of CFD results and from these results were able to obtain the best theoretical solution. Dem (2004) used FINE^{TM}/Design3D to optimise an axial compressor and turbine, which is the same procedure that Diener followed to optimise the mixed-flow compressor impeller. The mixed flow compressor impeller was chosen by Diener (2016) as it is a good compromise between pressure ratio and axial and radial space constraints while achieving good mass flow rate capabilities. The optimisation techniques used by Diener (2016) are further explained in subsection 2.2.2.

The inlet and outlet velocity triangles associated with the compressor impeller are shown in figure 2.2 below.

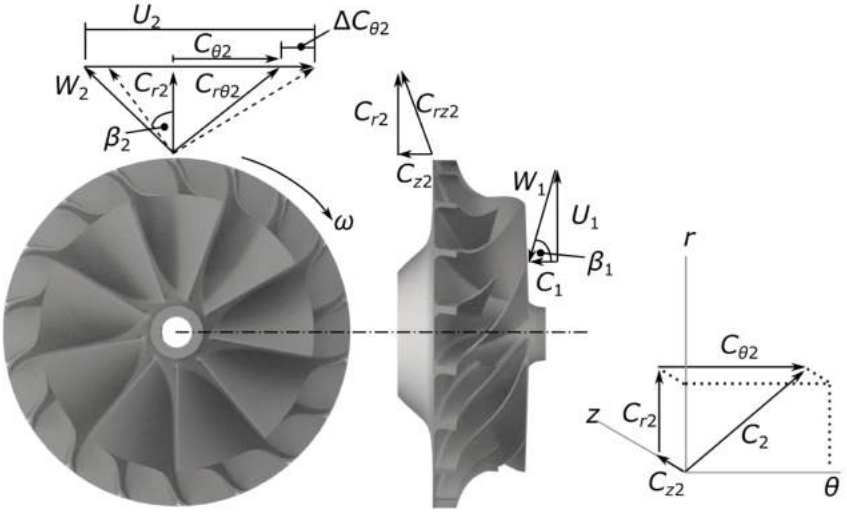

Figure 2.2: Velocity triangles of a mixed-flow compressor impeller (Diener, 2016)

For compressors the Mollier diagram is commonly used to describe the changes in enthalpy and entropy in a gas and aids the design process of turbomachines.

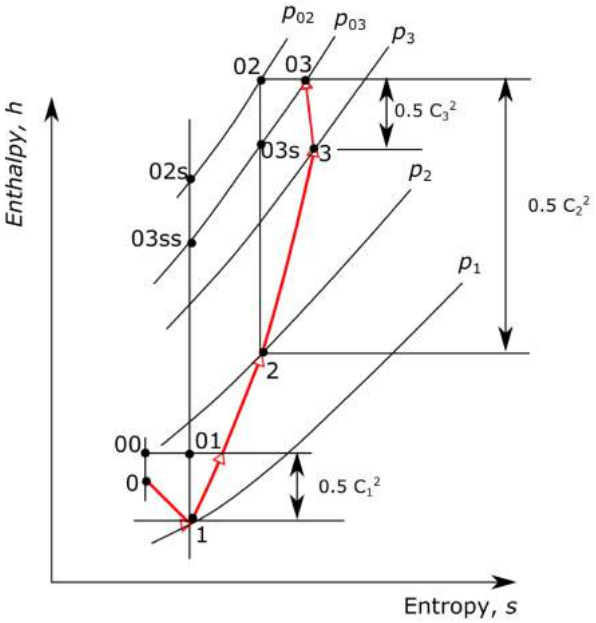

Figure 2.3: Mollier diagram of a generalised centrifugal compressor stage Dixon (2005)

The red line describes the static enthalpy states of the gas. The subscript 0 which appears before the subscript representing the station number denotes a stagnation condition.

The inlet casing of a turbomachine accelerates the gas from point 0 to 1 while the stagnation enthalpy remains constant. Then both the static and stagnation enthalpy is increased via the compressor from state 1 to 2. Static pressure is then recovered via a diffuser from point 2 to 3 while the stagnation enthalpy remains constant due to no added shaft work and assumed adiabatic flow (Diener, 2016). However there is a total pressure decrease of $p_{02} - p_{03}$ due to friction losses (Struwig, 2014).

In the experimental set-up a turbine is driven by cold compressed air. The turbine is directly coupled to the compressor, therefore the power absorbed by the compressor is determined by calculating the energy the turbine extracts from the cold compressed air. The turbine work delivered is determined by (Hall, 2015):

$$P_T = \eta_t C_p T_{ti} (1 - \frac{T_{to}}{T_{ti}})^{\frac{\gamma}{\gamma - 1}} \tag{2.2.1}$$

It is necessary to evaluate the performance of the complete compressor in terms of total-to-total quantities. The total-to-total quantities are determined by the sum of the static pressure and kinetic energy head. The ratio of total isentropic enthalpy rise to actual enthalpy rise is defined as the isentropic efficiency and is given by (Dixon, 2005):

$$\eta_{t-t} = \frac{C_p T_{01}(T_{03ss}/T_{01}) - 1}{U_2 C_{\theta 2}} \tag{2.2.2}$$

The pressure ratio across the impeller and diffuser is given as Dixon (2005):

$$\frac{p_{03}}{p_{01}} = (\frac{T_{03ss}}{T_{01}})^{\frac{\gamma}{\gamma-1}} \tag{2.2.3}$$

By rearranging equation 2.2.2 and substituting into equation 2.2.3 we find an expression for the totat-to-total pressure ratio as Dixon (2005):

$$PR_{t-t} = [1 + \frac{\eta_{t-t} U_2 C_{\theta 2}}{C_p T_{01}}]^{\frac{\gamma}{\gamma-1}} \tag{2.2.4}$$

The mixed-flow compressor is evaluated using the total-to-total pressure ratio and total-to-total isentropic efficiency along with the following normalized parameters (Struwig, 2014):

- Corrected mass flow, $\frac{\dot{m}\sqrt{T_{01}}}{p_0 1}$
- Total-to-total Pressure ratio, PR_{t-t}
- Corrected rotational speed, $\frac{N}{\sqrt{T_{01}}}$
- Total-to-total isentropic efficiency, η_{t-t}.

These parameters are used to draw-up a performance map of the compressor at different speeds. These maps are used to indicate choke and surge margins, efficiency islands and pressure ratios at given mass flow rates. An example of such a map is given from Dixon (2005) in figure 2.4 below:

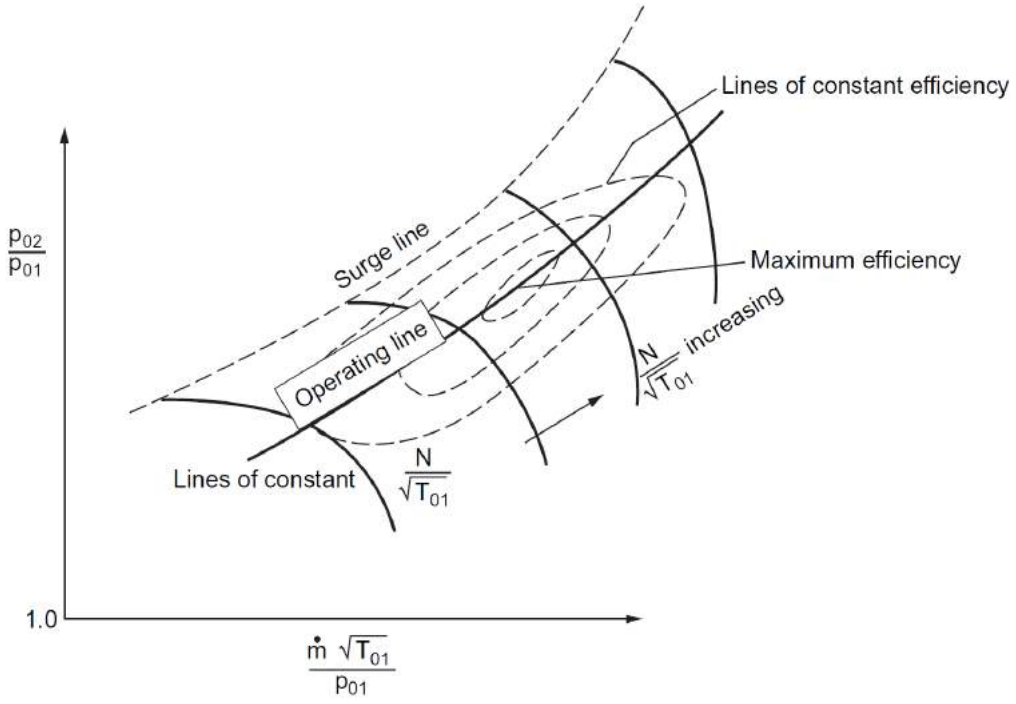

Figure 2.4: Performance Map of a Typical Centrifugal Compressor (Dixon, 2005)

Surge and choke are two phenomena that limit the safe operating range of compressors. The effect of surge is a sudden drop in discharge pressure and induced aerodynamic vibrations within the blade channels which are transferred through the blades to the rest of the test bench. Choke on the other hand occurs when the flow becomes sonic in certain regions of the compressor. The flow can become choked in either the inlet, the rotating impeller blades or within the diffuser passages. The flow is choked when there is no further increase in mass flow rate through the compressor as the pressure over the compressor is reduced. Brun and Nored (2006) offers two methods to determine the safe operating range of centrifugal compressors. These methods are called surge margin and compressor turndown. The surge margin determines how close the operating point of the compressor is to surge and is expressed as follows:

$$SM\% = |\frac{Q_{design} - Q_{surge}}{Q_{design}}| \times 100|_{N=constant} \tag{2.2.5}$$

Dixon (2005) expressed it as:

$$SM\% = \frac{PR_{design} - PR_{surge}}{PR_{design}} \tag{2.2.6}$$

The turndown defines the compressor's operating range at a given rotational speed for a fixed pressure ratio (Struwig, 2014) and is expressed as follows:

$$TD\% = |\frac{Q_{choke} - Q_{surge}}{Q_{choke}}| \times 100|_{H=constant} \tag{2.2.7}$$

2.2.2 Impeller design

The features that are considered during the design of a mixed-flow compressor impeller are shown in Figure 2.5 below. The following symbols are used to define the features on the impeller:

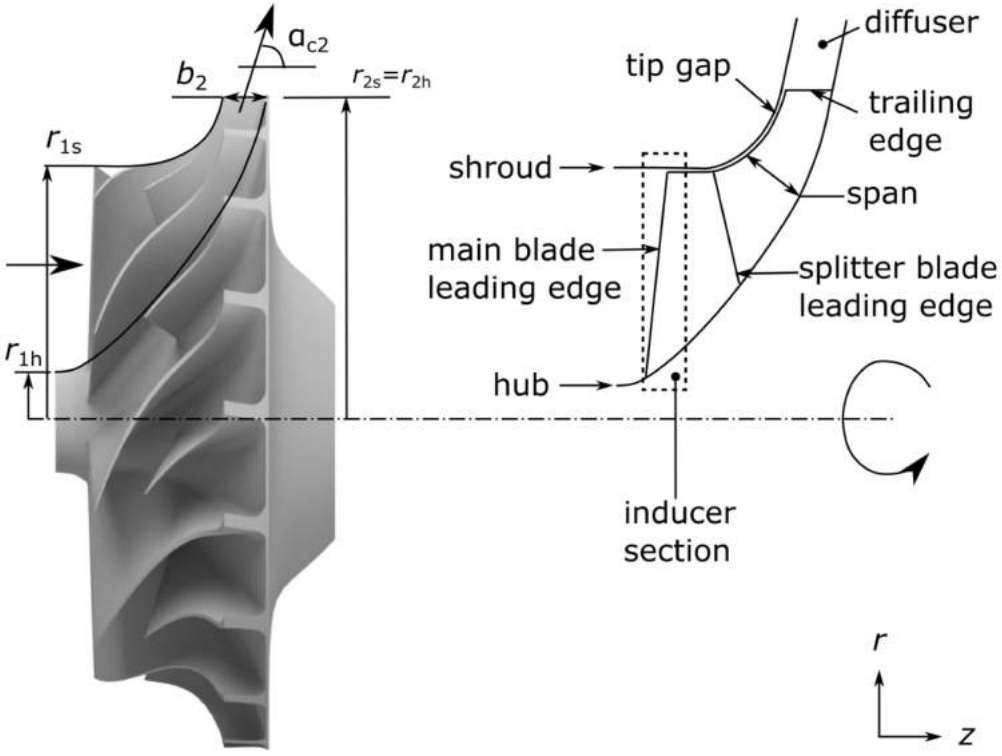

Figure 2.5: Meridional View of Compressor Features (Diener, 2016)

The hub, shroud, main and splitter blades are all defined according to the guidelines in NUMECA, as seen on the right of Figure 2.5. The shroud is the casing that encloses the impeller and incorporates a tip gap between the blades

and casing. Referring to Figure 2.2, while the impeller is rotating the atmospheric air meets the leading edge of the blades at a relative velocity of W_1 and absolute velocity of C_1 with a blade tip speed of U_1. The flow then follows the blade passage where it is expelled from the trailing edge of blades. The flow now has a tangential velocity $C_{\theta 2}$, radial velocity C_{r2} and axial velocity C_{z2} component. Due to slip the flow does not leave the trailing edge of the blades at the blade angle β_2. This decreases the ideal tangential velocity component $C_{\theta 2}$.

While in operation the blades undergo loading due to the acceleration of air against the blades, which is known as the Coriolis effect. By changing the meridional outlet angle from radial (90^o) to smaller, with the same flow path length, the Coriolis forces are relaxed and thus slip is reduced (Diener, 2016). Based on literature, Diener (2016) specifies that for a compressor to be recognised as a mixed-flow compressor the meridional exit blade angle needs to be between 22^o and 65^o from the axial plane. Nevertheless, he designed the rotor to have a meridional angle of 74.5 degrees at the outlet.

Diener (2016) was given specific engine size constraints and compressor performance requirements to adhere to. These constraints were defined by an engine thermodynamic cycle analysis code (ECA) which was then transfered to a 1-dimensional mean-line design code for compressors. GasTurb12 was used as the ECA code and CFturbo as the 1-dimensional mean-line code. The 1-dimensional mean-line code applies turbomachinery theory and empirical data to a mean flow path to determine the geometry of the compressor (Diener, 2016). The design generated by the mean-line code is then validated using 3-dimensional flow simulation software (CFD). In this case NUMECA FINE^{TM} was used.

Diener performed an aero-mechanical optimization using CFD coupled with FEA (Finite element analysis). After the design had been finalised, Diener (2016) then validated the FEA results from NUMECA using MSC SimXpert, completing the process with a modal analysis of the rotor. The design procedure used by Diener is shown graphically in Figure 2.6 below.

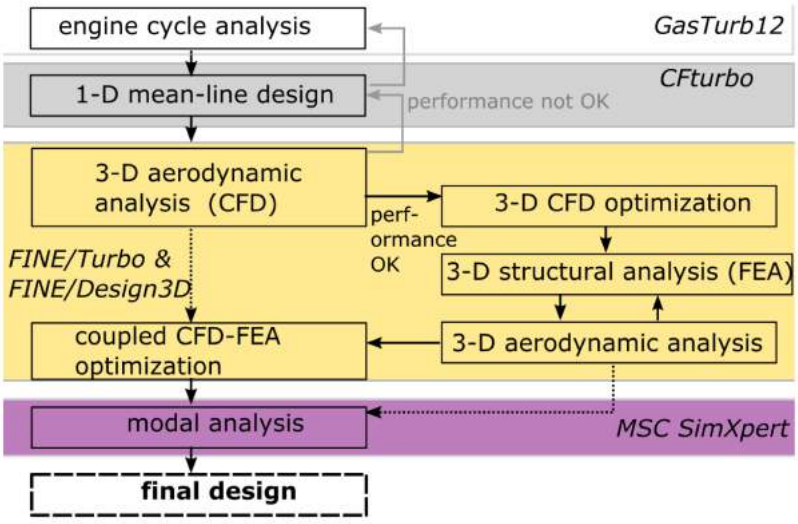

Figure 2.6: Compressor Design Procedure Outline (Diener, 2016)

The final optimized impeller results found by Diener are displayed in table 2.1 below. The theoretical impeller designed by Diener incorporates a surge margin of 12% and a choke margin of 3.8%. The Von Misses stresses for the design are 30% below that of the yield limit of aluminum. The design has a blade tip clearance of 0.2 mm from the casing, which is the minimum distance allowed as the peak radial displacement of the trailing edge is 0.12 mm. Diener's investigation revealed that there are a number of resonant frequencies associated with the impeller. These are to be avoided during the experimental phase. These resonant frequencies become critical at speeds from 70 to 90 krpm, causing a flapping excitation of the main blades.

It is interesting to note that Diener modelled the impeller with a straight vaneless diffuser angled at the same hub exit angle of the impeller, which might cause the results to deviate when a curved diffuser is used.

Table 2.1: Impeller Performance Quantities (Diener, 2016)

Quantity	Final Design
$\dot{m}_{design}(kg/s)$	0.844
PR_{t-t}	5.25
η_{t-t}	86%
$\sigma_{VM,max}(MPA)$	344
Tip Gap (mm)	0.2

2.2.3 Influence of Tip Clearance

Danish (2006) investigated compressor stage performance for 9 tip clearance levels from no gap to 1 mm at a mass flow rate of 0.35 kg/s. Danish (2006) observed that a stage pressure ratio loss of 15% and a peak efficiency loss of 10% as the blade tip clearance is increased from zero to 1 mm. The maximum impeller efficiency was found between 0.1 mm and 0.2 mm.

Pandurangadu (2014) investigated the flow field of a low speed centrifugal compressor experimentally by using a partial shroud attached to the rotor blade tip at three levels of blade tip clearances. 2.2%, 5.1% and 7.9% of blade height at the trailing edge were examined. Pandurangadu (2014) found the loss in static pressure and total pressure coefficient with increase in blade tip clearance to be at it's highest at the tip of the blade due to high pressure fluid leakage.

From the observations of Danish (2006) and Pandurangadu (2014) it is seen that adjusting the blade tip clearance does have a notable effect on the performance of the impeller. Danish (2006) observed the peak impeller stage performance to be between 0.1 mm and 0.2 mm which agrees well with the blade tip clearance of the optimised impeller designed by Diener (2016).

2.3 Diffusers

This section gives an overview of diffusers and the design created and optimized by Kock (2016).

2.3.1 Diffuser Theory

A diffuser converts the kinetic energy of the fluid leaving the impeller into pressure energy either through free diffusion in the annular space after the impeller or by incorporating a row of fixed diffuser vanes (Dixon, 2005). There are two types of diffusers, namely vaned and vaneless diffusers. Vaned diffusers are normally used when space is limited and incorporate guide vanes. Vaneless diffusers only rely on the increase in radial cross-sectional area to decelerate the air flow. Vaned diffusers guide the flow to a specific outlet angle. For a vaned diffuser, similar velocity triangles than the impeller is used to analytically evaluate the flow as shown in Figure 2.7 below.

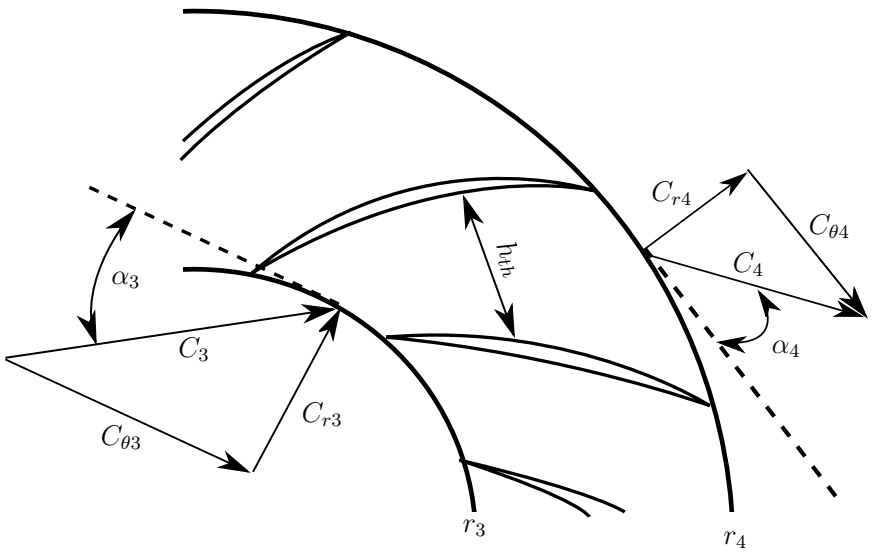

Figure 2.7: Vaned Diffuser Velocity Triangles (adapted from Kock (2016))

The thermodynamic path that is followed is from point 2 to 3 on the Mollier Digram in Figure 2.3. The flow exits the impeller at its appropriate blade angle into a small annular space before entering the diffuser. The fluid enters the diffuser with an absolute velocity of C_3 which consists of a tangential and radial velocity, $C_{\theta 3}$ and C_{r3} respectively. The fluid flow is then diffused through the passages due to the natural radial increase in cross-sectional area. The velocity slows down, which increases the static pressure. The fluid flow now exits the diffusers with an absolute velocity of C_4. As mentioned in section 2.2.1, the enthalpy stays constant throughout the diffuser as no shaft work is being done on it and can therefore be expressed as:

$$h_{02} = h_{03} \tag{2.3.1}$$

The total-to-total pressure ratio is taken across the impeller and diffuser and is expressed as:

$$PR_{t-t} = \frac{p_{03}}{p_{01}} \tag{2.3.2}$$

The total-to-total isentropic efficiency across the impeller and diffuser is expressed as:

$$\eta_{t-t} = \frac{(h_{03s} - h_{00})}{(h_{03} - h_{00})} = \frac{\left(\frac{p_{03}}{p_{00}}\right)^{\frac{\gamma-1}{\gamma}} - 1}{\frac{T_{03}}{T_{00}} - 1} \tag{2.3.3}$$

2.3.2 Diffuser Formats

Vaneless Diffusers

There are three main aspects to consider when designing a diffuser, divergence angle (2θ), non-dimensional length (L/W) and area ratio (AR). The divergence angle indicates the angle at which the walls depart from each other (Kock, 2016). The non-dimensional length which is the ratio of the length (L) to the width (W) of the diffuser is used as a performance measure. Reneau *et al.* (1967) specifies that the optimal divergence angle is between $7^o < 2\theta < 12^o$, with a non-dimensional width to be between $6.5 < L/W < 17$. Using the above mentioned performance measures, Reneau *et al.* (1967) mapped the flow regimes of channel diffusers into a useful plot shown in Figure 2.8 below.

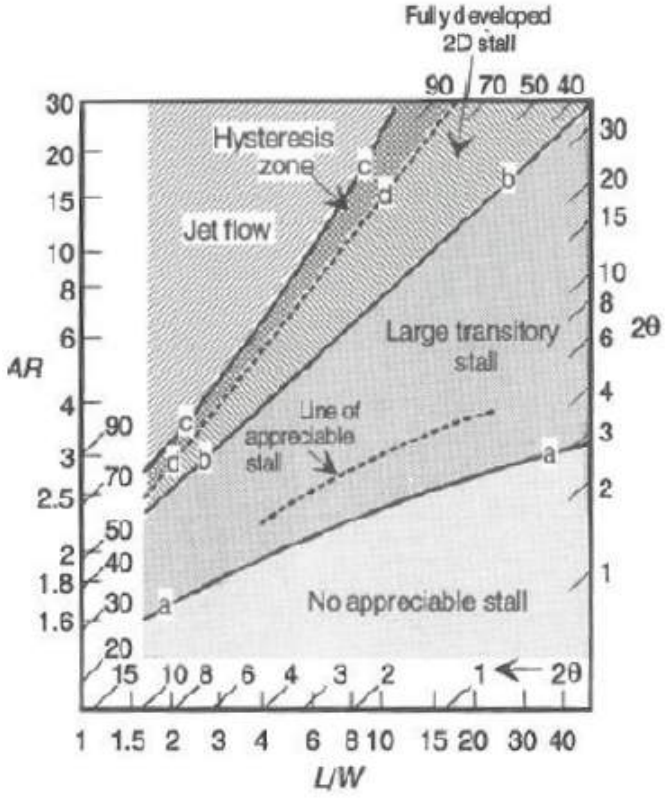

Figure 2.8: Channel Diffuser Flow Regimes (Japikse and Baines, 1994)

The lines a-a to d-d represent stall conditions. As the area ratio or divergence angle is increased these stall conditions are approached. Above the first stall condition a-a the line of appreciable stall is reached. According to Japikse and Baines (1994), 50% of transitional stall is allowed, surrounding the area of appreciable stall, but only in one corner or one side of the wall. The diffuser is

still able to deliver an acceptable static rise under these conditions. Increasing the area ratio or divergence angle any further will cause the performance of the diffuser to decrease. Therefore the peak performance area of diffusers lies within the region denoted "Large Transitory Stall" (Japikse and Baines, 1994).

Vaned Diffusers

Vaned diffusers are normally preferred when there is limited space available. They allow for static pressure recovery in a shorter radial distance than that of a vaneless diffuser (Kock, 2016). Vaned diffusers use two methods to diffuse the air flow. One method is increasing the effective passage area, also known as the radial cross-sectional area ratio (AR). The second method is by increasing the blade loading (L) (Aungier, 2000). The blades help to decelerate the flow while also guiding the flow towards the exit. The static pressure recovery coefficient (C_P) is a parameter that is used in the evaluation of a diffuser. It describes what percentage of inlet energy is converted to static pressure. Typically, static pressure recovery coefficients range between 0.3 and 0.5 for vaned diffusers (Japikse and Baines, 1994). The static pressure recover coefficient is expressed as:

$$C_P = \frac{p_3 - p_2}{p_{02} - p_2} \tag{2.3.4}$$

The ideal pressure recovery coefficient is given by:

$$C_{P_{ideal}} = 1 - \frac{1}{AR^2} \tag{2.3.5}$$

Further details on the design variables used for the blade spacing and geometric blade features are given and explained in Kock (2016).

2.3.3 Diffuser design by Kock

The design process for the optimized diffuser followed by Kock (2016) used an in-house Mean Line Code (MLC), developed by Burger (2016) based on the work of Aungier (2000). The MLC is used to find a preliminary solution that is then afterwards optimized to produce the final solution. For the optimization of the diffuser, Kock (2016) used an artificial neural network (ANN) that incorporates a genetic algorithm. The genetic algorithm creates functions of all possible solutions within specific boundaries and then finds the best possible solution. Kock (2016) followed a similar design process than that of Diener (2016). Kock (2016) also found that a discharge flow angle (α_{4c}) of 60^o was the

best possible solution for the Mean Line Design Diffuser (MLDD) while obtaining an operating range of 14.2%. Kock (2016) then optimized the MLDD, which yielded a substantial increase in performance. The increase in PR_{t-t}, η_{t-t}, diffuser C_P and PR_{s-s} is shown in Table 2.2 below.

Table 2.2: Optimized performance at Design Point (Kock, 2016)

Design	PR_{t-t}	η_{t-t}	Diffuser C_P	PR_{s-s}
Mean Line Design	4.1	73%	0.43	1.6
Optimized Design	4.44	80%	0.6	2.04
Improvement	7.7%	8.75%	28.33%	21.56%

The operating range however remained the same, even though there was a substantial increase in performance. The discharge flow angle only increased by 3%. The optimized diffuser passage geometry was designed with a sharper angle after the impeller. The leading edge (LE) of the diffuser's vanes were also designed to be closer to the trailing edge (TE) of the impeller's vanes than the MLDD. It was also found that the size of the recirculation bubble was reduced when the LE of the diffuser vanes are parallel to the TE of the impeller vanes, with the sharp turn in passage geometry also contributing to the reduction. A comparison of the effect that the MLDD and optimized diffuser has on the flow within the passage geometry is shown below:

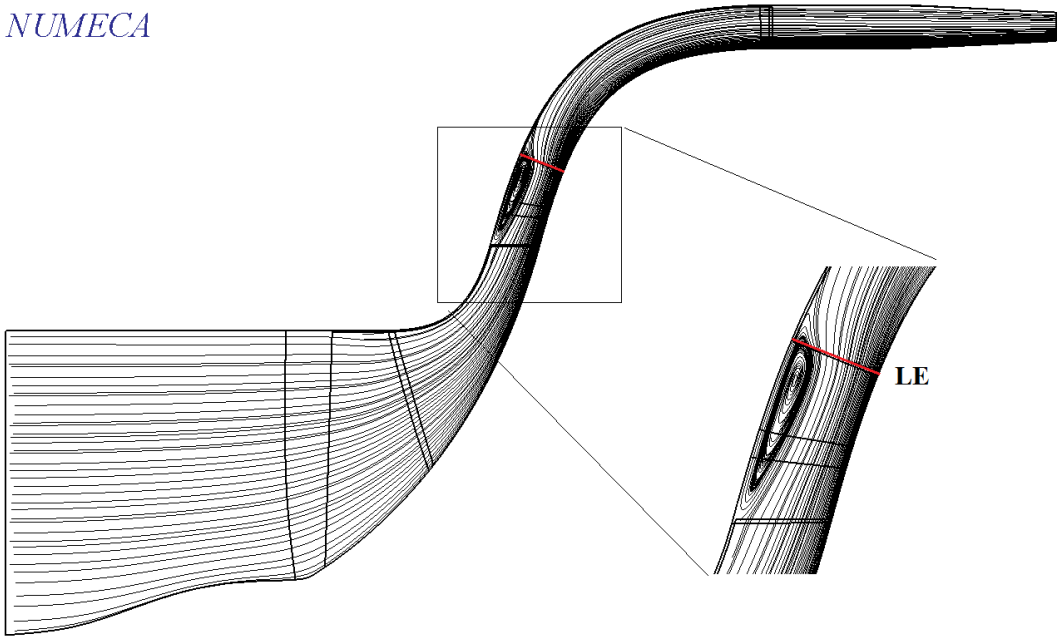

(a)

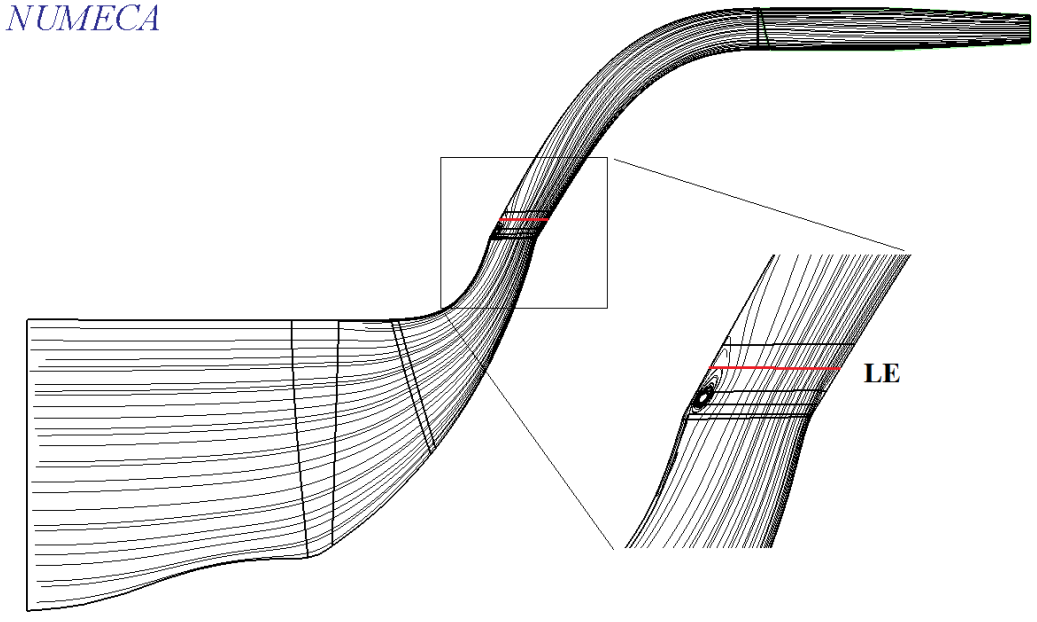

(b)

Figure 2.9: Comparison of Recirculation bubbles of a) Mean Line Design and b) Optimized Design (Kock, 2016)

Chapter 3

Numerical Evaluation

The numerical analysis tool NUMECA is used to determine the numerical performance of the impeller and diffuser designed by Diener (2016) and Kock (2016) respectively. Both the impeller and diffuser was designed through the use of a mean line code and optimized using NUMECA software. The mean line code generated the necessary *.geomTurbo* files that defines the meridional geometry for mesh generation. NUMECA AutoGrid5^{TM} is used to generate the 3D mesh to analyse the flow domain. The mesh is then exported as an *.igg* and *.trb* file to NUMECA Fine^{TM}/Turbo where the designs are numerically analyzed. Post processing of the numerical analysis is done with NUMECA CFView^{TM}. In this chapter the impeller designed by Diener is analyzed numerically, both with the radial diffuser designed by Kock and a channel diffuser manufactured by Thomas.

3.1 Mesh Generation - AutoGrid 5^{TM}

AutoGrid5^{TM} is a semi-automatic structured meshing tool which generates a rudimentary mesh which then requires user input to refine the mesh to acceptable quality. It uses conformal mapping between the three-dimensional cartesian space and the two-dimensional blade-to-blade space (Struwig, 2014). Firstly a meridional mesh is specified. The meridional mesh requires the number of flow paths (or layers) as well as control lines to be specified to aid the blade-to-blade mesh generation. The blade-to-blade mesh control is then used to specify the size and number of cells along the blade profile until a satisfactory mesh quality is achieved. Once a satisfactory mesh quality is achieved, a three-dimensional mesh is generated. The grid quality of the three-dimensional mesh is then inspected and if found satisfactory, the mesh is exported to Fine^{TM}/Turbo.

3.1.1 Meridional Mesh Setup

The control lines are used to specify the number of grid points within the flow paths upstream and downstream of the blades (Kock, 2016). The user specifies the number of control lines as well as their nature (linear/non-linear) and "Streamwise Number of Points" to determine the coarseness of the grid at the inlet and outlet respectively. The "Streamwise Number of Points" were set between 13 and 29. The number of flow paths are chosen using the *Row Wizard* where the *Spanwise Grid Point Number* is set to 73 and 57 for both the impeller and diffuser respectively. The boundary layer effects are taken into consideration by stacking the flow paths closer together near the wall to meet the y^+ requirement (Figure 3.1). These flow paths also represent the number of meridional blade layers. The *Row Wizard* also allows the user to set the *Wall Cell Width* and *Tip Gap*. The *Tip Gap* for the Impeller was varied from 0.2 mm to 0.6 mm with 0.2 mm increments at the LE and TE to simulate possible tip clearances used in the experimental setup.

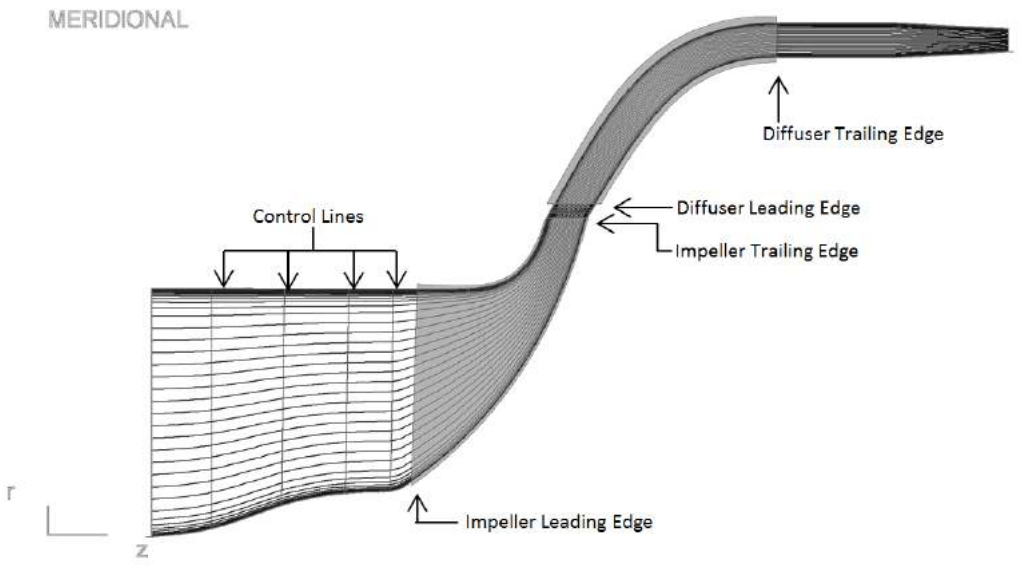

Figure 3.1: Meridional Mesh

Selecting the turbulence model for the flow solver is based on the feasibility study done by Kock (2016). Kock (2016) evaluated the Shear Stress Transport (SST($k-\omega$)) turbulence model (with extended wall functions) and $k-\epsilon$ turbulence model against the Spalart Allmaras (SA) turbulence model. Kock (2016) found that the performance of the SA model was slightly better than that of the SST model but with much smaller computational memory requirement. The SA model compared well to the performance of the $k-\epsilon$ model. However, the $k-\epsilon$ model performs poorly with rotating and swirling flow and

is deemed unsatisfactory for boundary layers with adverse pressure gradients Menter (1992). Thus the SA turbulence model is chosen as it is computationally economical for external flow boundary layers and more robust in capturing the boundary layers in adverse pressure regions.

Flow acceleration over bodies of any geometry causes the boundary layer thickness to decrease. According to NUMECA (2014a) the y^+ value need to fall between 1 and 10 for the Spalart Allmaras turbulence model to accurately solve the boundary layer. The y^+ value is a non-dimensional distance which is used to evaluate the wall cell height with respect to the boundary layer. This indicates whether the cells are able to accurately capture the boundary layer (Versteeg and Malalasekera, 2007). Equation 3.1.1 below takes the first cell height as well as the fluid velocity into account when predicting the y^+ value. The *Wall Cell Width* was set to 0.0008 mm for both the Impeller and Diffuser respectively. This value was chosen according to the prediction made using equation 3.1.1 from Versteeg and Malalasekera (2007). Using a wall cell width of 0.8 μm and average fluid speed of 500 m/s, y^+ is predicted to have a value of 6.

$$y^+ = \frac{y_{wall}}{6(\frac{V_{av}}{\nu})^{\frac{-7}{8}}(\frac{L_{av}}{2})^{\frac{1}{8}}} \tag{3.1.1}$$

3.1.2 Blade-to-Blade Mesh Setup

The structured mesh around the blades on each layer is called the blade-to-blade (B2B) mesh. This B2B mesh comprises of mesh blocks in the form of H- and O-topologies. The H&I-topology is generally used for impellers with splitter blades for mesh quality purposes (NUMECA, 2014a). The default topology was selected for the diffuser. The distribution of grid points for both the impeller and diffuser are shown in Appendix C. With regards to the impeller the H-topology at the inlet was disabled but selected for the outlet. The *High Staggered Blade Optimization* was chosen for both the main and splitter blade where the inlet and outlet angle of both are chosen. The inlet-outlet angle for the main blade was chosen to be high-normal and for the splitter blade it was chosen to be normal-normal. Further visual details are provided in Appendix C.2.

For the Diffuser, *Matching Periodicity* was selected as well as *High Staggered Blade Optimization* within the *B2B Topology* definition window. For the *High Staggered Blade Optimization* the inlet-outlet angle for the diffuser vanes was selected as low-high angle. The rest of the topology control was left unchecked. As mentioned above, the *Wall cell width* for both the Impeller and Diffuser was set at 0.0008 mm.

The following settings apply to both the Impeller and Diffuser. None of the control boxes within the *3-D Mesh Control* window was selected. The *Span Interpolation* was set at 2% of yielded grid quality. Within the *Optimization Properties* the *Optimization Steps on Fine Grid* was set at 600 and the *Gaps Optimization Steps* was set at 500. Using *Expert* mode within the properties window *Skewness Control* and *Skewness Control in Gaps* was set at Medium and Full respectively. *Multigrid Acceleration* and *Multisplitter Control* were both also selected. Figures 3.2 and 3.3 below shows the end result of the above applied settings.

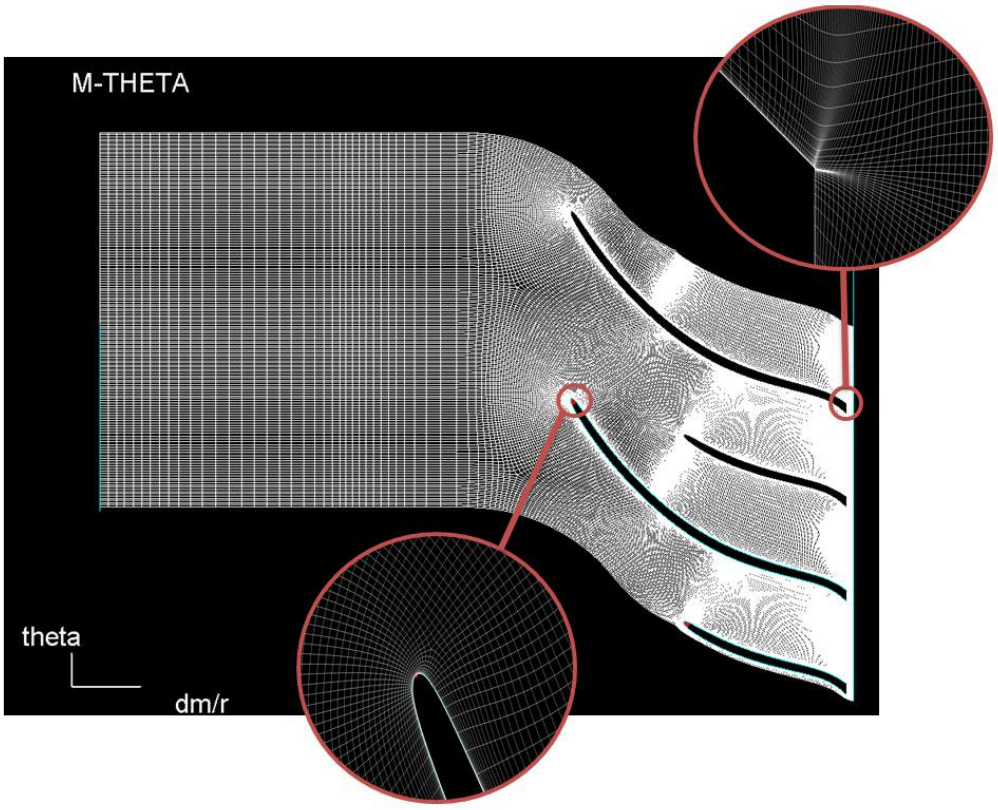

Figure 3.2: Impeller Blade-to-Blade Mesh (50% Span)

From the Impeller B2B mesh one can see that there is a small amount of clustering. The clustering can be controlled using the inlet and outlet relaxation factors which were applied to both the impeller and diffuser. Based on the work of previous authors, the clustering of the fine mesh is however deemed satisfactory. There is less clustering on the diffuser B2B mesh compared to

the B2B mesh of the impeller however. This is most likely due to the absence of splitter blades.

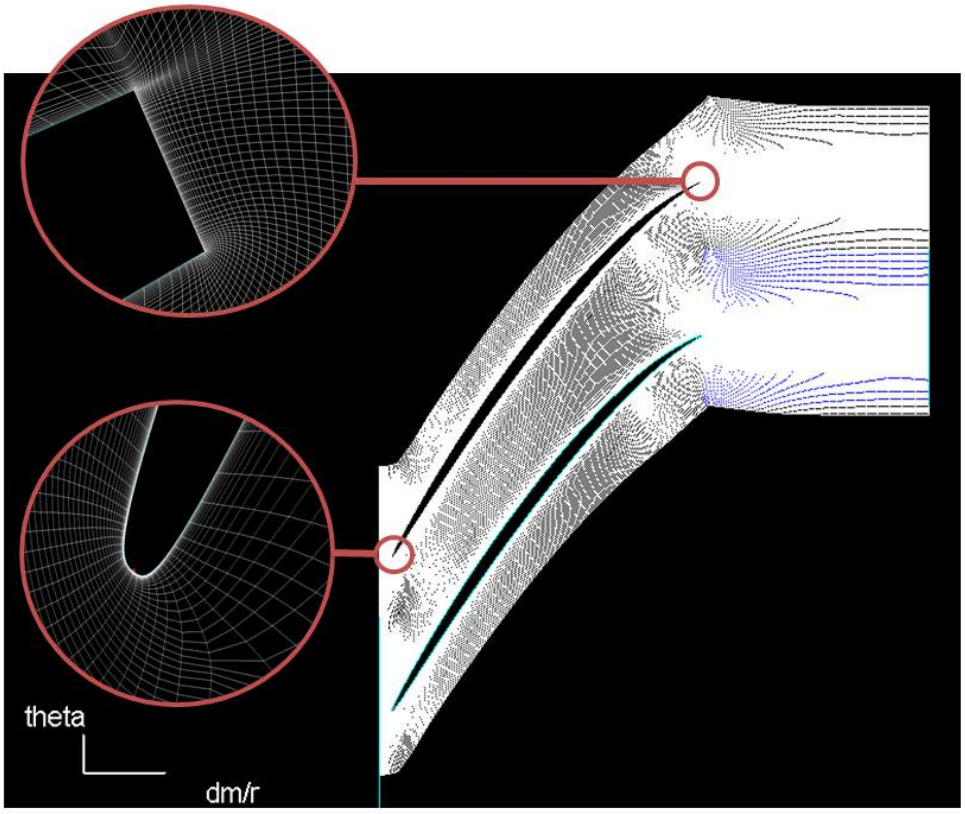

Figure 3.3: Diffuser Blade-to-Blade Mesh (50% Span)

3.1.3 Mesh Quality

In order for NUMECA to solve the 3-D grid domain the grid need to adhere to strict quality measures. These include orthogonality, expansion ration, aspect ratio, and angular deviation. The constraints on each of these are listed below (NUMECA, 2014b):

- Orthogonality should be above 18^o and below 90^o.
- The expansion ratio should be less than 3.4.
- The aspect ratio should be less than 10000.
- The angular deviation should be less than 40^o.

These constraints serve as a guideline and ensures that the solver operates with stability and reaches convergence. However these constraints become difficult to attain, depending on the blade geometry. Table 3.1 below summarizes the grid quality check for the fine mesh.

Table 3.1: Overall Grid Quality

Criterion	Impeller	Diffuser
Minimum Skewness (Deg)	20.24	19.20
Maximum Aspect Ratio	6141.6	2986.5
Maximum Expansion Ratio	3.0	3.26
Span-wise Angular Deviation	41.26	19.86

Although the angular deviation criteria is slightly out of bounds, it is regarded as acceptable and the solver remained stable. The entire fine grid consisted of 5.79 million cells, with 4.33 million attributed to the impeller and 1.46 million to the diffuser. The medium grid consists of 4.83 million and the coarse grid of 3.58 million cells.

3.2 Flow Solver

3.2.1 Flow Solver Settings - FINE^{TM}

NUMECA FINE/Turbo^{TM} is used as the numerical flow solver with the following configurations indicated in Table C.1 below. As mentioned above the Spalart-Allmaras turbulence model was selected due to the model being able to accurately capture flow with adverse pressure gradients such as high lift blade profiles. The most important settings to note are the *Boundary conditions* and discretization scheme. For the *Inlet*, *Total Quantities* were imposed in the Velocity Direction. *Pressure* was imposed for the *Outlet* and the outlet static pressure varied from $260kPa$ to $425kPa$ corresponding to the choke and surge margins at 95 krpm. For the *Periodic* boundary condition, all periodic boundaries were selected to match. The Rotor and Stator boundary conditions also need to be defined with the hub, blades and shroud having their own conditions for both the Impeller and Diffuser. A *Constant Rotational Speed* of 0 rpm was selected for all the components of the Diffuser. *Area Defined Rotational Speed* was selected for the hub of the impeller with the values indicated in Table C.1 below. The impeller shroud remains stationary with a *Constant Rotational Speed* of 0 rpm. The impeller blades were selected to have a *Constant Rotational Speed* of 95 krpm. Second-order upwind was selected as the discretization scheme as it produces larger stability bounds and better numerical resolution than symmetric schemes (Warming and Beam, 1976).

NUMECA makes use of its EURANUS flow solver which incorporates a Multi-Grid technique to minimize computational time. EURANUS first implements a coarse grid and then transfers the data to a finer grid. The grid level was set at medium (1 1 1) which resulted in two grid levels. Quantities that are to be exported from FINE^{TM} are shown in Table C.1 from the "Outputs" row in Appendix C.3. Convergence is reached when the following criteria have been met (NUMECA, 2014a):

- Inlet and Outlet mass flow rates are within 1% of each other.
- Stabilization of Global Residuals.

The convergence of mass flow rate, pressure ratio, isentropic efficiency and global residuals were observed before continuing to post processing. The convergence of these quantities show whether the solver was stable during the resolution of the computational domain.

The simulation was set to run 4000 iterations with a convergence criteria of -8 (Eight orders of magnitude) to prevent the solver from finishing prematurely.

3.2.2 Post Processing - CFView

Post processing of the Output results (*.run) generated within FINE^{TM} was done using the user interface, CFView. As mentioned above the Static Outlet Pressure was varied from 260 kPa to 425 kPa as a method to vary the mass flow rate. The output results that are of interest is pressure ratio, mass flow rate, isentropic efficiency, static and total pressure, static pressure coefficient and total temperature. From these quantities a performance map of the compressor could be determined. The quantities were obtained by taking the mass-averaged weighted integral of surfaces created at specific radial co-ordinates. Another quantity that is of importance is the y+ values on the impeller and diffuser hub, shroud and blade surfaces, which are inspected using CFView. The y+ values serve as a mesh quality indicator. Figure 3.4 below visually represents the y+ values on the Impeller main blade surface.

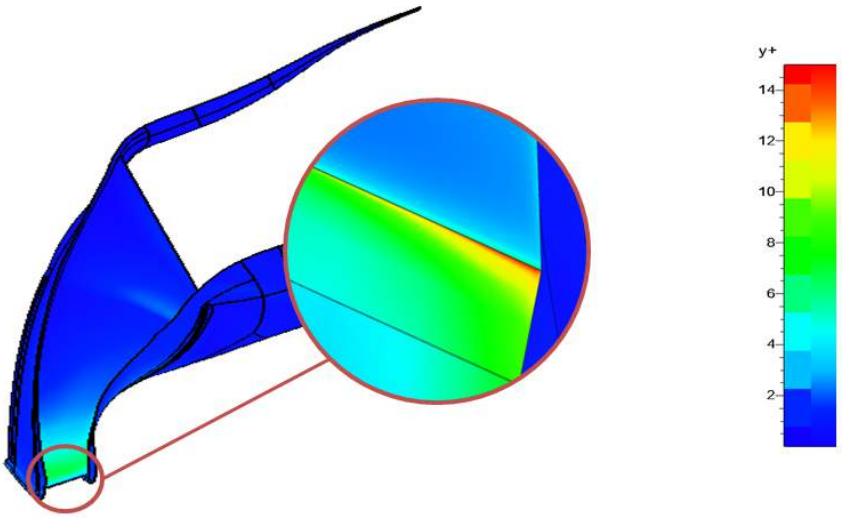

Figure 3.4: Impeller Y+ Values with Main Blade Trailing Edge enlarged

From the enlarged area at the trailing edge of the main blade, it can be seen that the y+ values are above the recommended value of 10 with a maximum value of 14.5. The most likely cause of this observation is boundary layer separation and large eddy formation due to the abrupt change in blade profile. However this is considered acceptable as this region is very small compared to the rest of the computational domain. Figure 3.5 below visually represents the y+ values on the diffuser main blade surface.

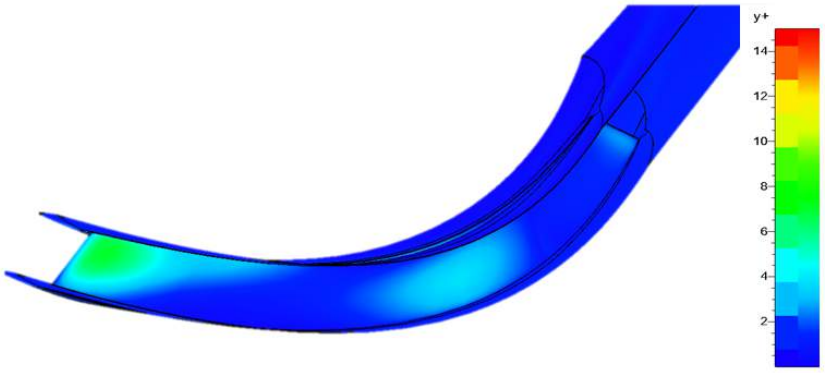

Figure 3.5: Diffuser Y+ Values

The y+ values on the diffuser surfaces were all within the recommended value of 10. A "macro" was generated to read the output result quantities and write them to a .txt file which is then imported to a Excel worksheet to draw a compressor performance map.

3.3 Results

The compressor and diffuser have previously been simulated by Diener (2016) and Kock (2016) respectively. Kock (2016) contributed to the CONVERGE project by adding the vaned diffuser to the compressor designed by Diener (2016). Figure 3.6 below shows the author's simulation results compared to the results of Kock.

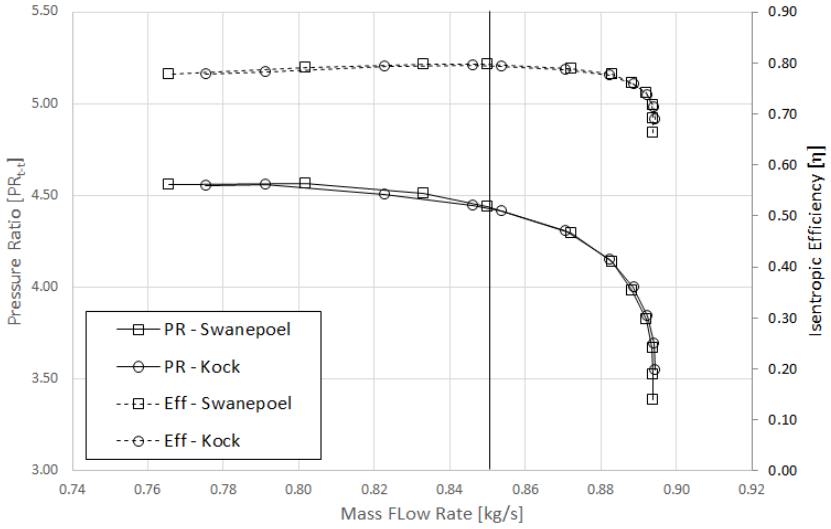

Figure 3.6: Comparison of numerical results to those of Kock (2016)

From figure 3.6 it can be seen that results are almost identical, with squares and triangles denoting the results obtained by the author and by Kock (2016) respectively. The total-to-total pressure ratio (PR_{t-t}) is displayed on the left vertical axis with the isentropic efficiency (η) displayed on the right vertical axis and mass flow rate ($\dot{m}$) displayed on the bottom axis. The solid vertical line denoting the operating point of the compressor which is at a mass flow rate of 0.85 kg/s.

Grid independence study was performed to ensure that output results remain within 3% of each other while the *Number of Grid Points* are varied. Figure 3.7 below displays the outcome of refining the grid twice from 3.58 to 5.79 million cells. It is interesting to note that the medium quality grid underperformed slightly compared to the coarse grid which could indicate that although the mesh met the criteria set out by NUMECA, it still resulted in a poorer mesh quality than that of the coarse mesh although the grid points were increased. However, the results remained within 3% of each other while refining the grid from coarse to fine quality.

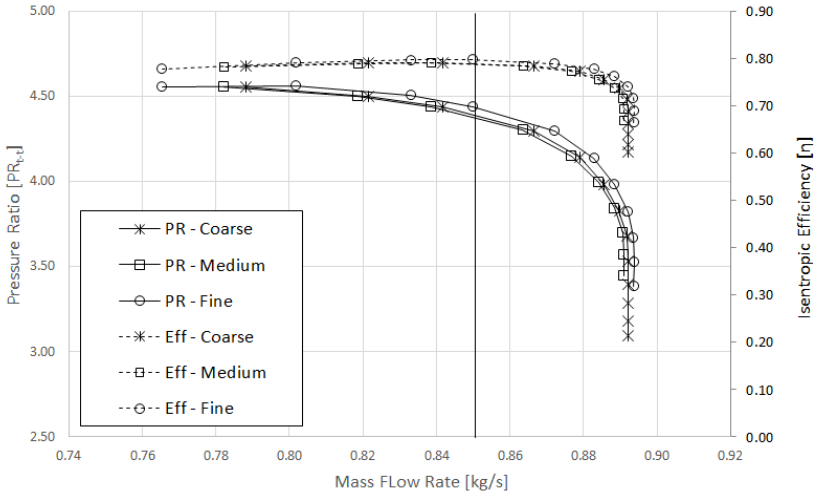

Figure 3.7: Grid Independence

A vaneless diffuser was manufactured by Thomas (2016) for the testing of the impeller in the gas dynamics laboratory. Therefore, after validating the numerical results presented above, the meridional geometry of the impeller and channel diffuser was imported into AutoGrid5^{TM}. The meridional geometry was manually edited by editing the .geomTurbo file. The diffuser was represented as an extension from the impeller outlet. The impeller and diffuser were then meshed according to the method mentioned in the above sections and solved using FINE^{TM}. The mesh consisted of 5.97 million cells and met all the prerequisites laid out by NUMECA. The results are displayed in figure 3.8 below. The performance of the vaneless diffuser was also compared to that of the vaned diffuser.

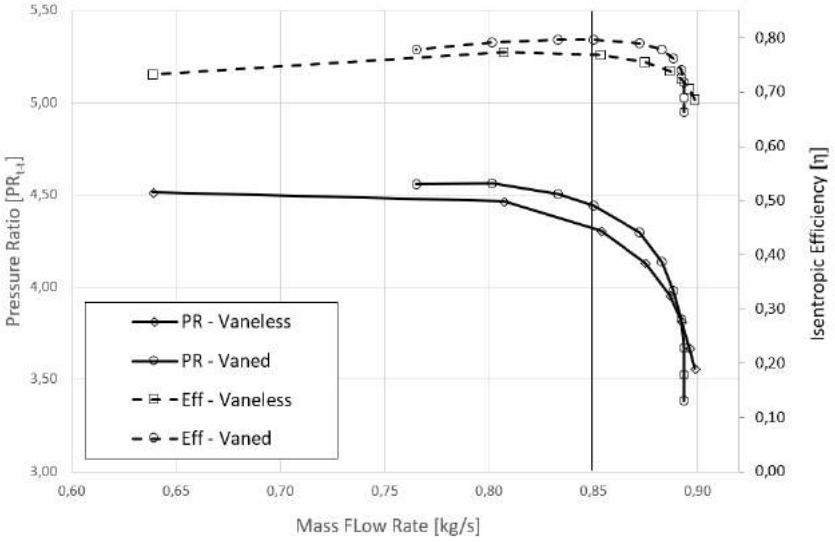

Figure 3.8: Diffuser Performance Comparison

Compared to the vaned diffuser, the vaneless diffuser only underperformed by 3% w.r.t. the total-to-total isentropic efficiency and 2.96% w.r.t. the total-to-total pressure ratio (at design flow rate) while exhibiting a larger operating margin. The vaneless diffuser has an operating static outlet pressure of 320 kPa compared to 400 kPa for the vaned diffuser. This would affect the combustion pressure and directly influence the thrust of the MGT. An advantage of the vaneless diffuser is that it provides an operating range of 28.91% compared to the vaned diffuser only providing an operating range of 14.35%. The increase in surge margin however is questionable w.r.t. numerical analysis as the surge margin is determined by solution instability. As soon as the solution becomes unstable it is regarded as the numerical surge margin.

The effect of increasing the tip gap clearance between the shroud and impeller blade tips are also inspected. The tip clearance is increased in increments of 0.2 mm, ranging from 0.2 - 0.6 mm through the *Tip Gap* option in AutoGrid5^{TM}. The graph in Figure 3.9 below illustrates how the performance of the impeller is affected negatively by the increase in tip clearance. Increasing the tip clearance to 0.4 mm decreased the performance with 4.5% and 3% in total-to-total pressure ratio and isentropic efficiency respectively with a 1.34% reduction in choke margin.

By increasing the tip clearance to 0.6 mm the performance decreased from the original design point with 8.1% and 6% in pressure ratio and isentropic efficiency respectively. The operating range also decreased by 2.1% with a 3.79% decrease in choke margin, which is attributed to the increase in blade tip leakage flow.

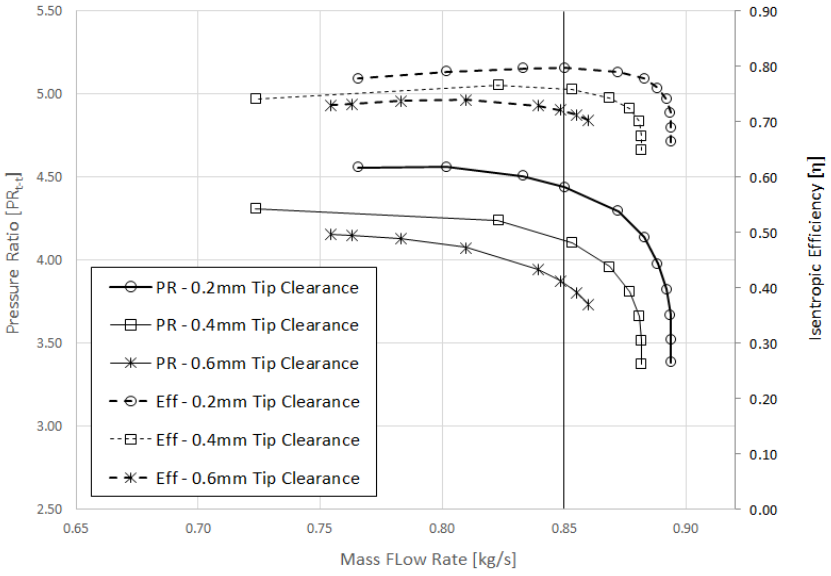

Figure 3.9: Tip Clearance Increase

Further inspection into flow patterns are done to explain the decrease in performance. Figure 3.10 displays the tangential flow pattern over the trailing edge of the blade with a 0.2 mm tip clearance. It is noted that the mass flow rate over the blade tip is limited due to the small tip clearance. The remainder of the fluid is diverted to the outlet of the impeller with a small amount of swirl in the axial direction.

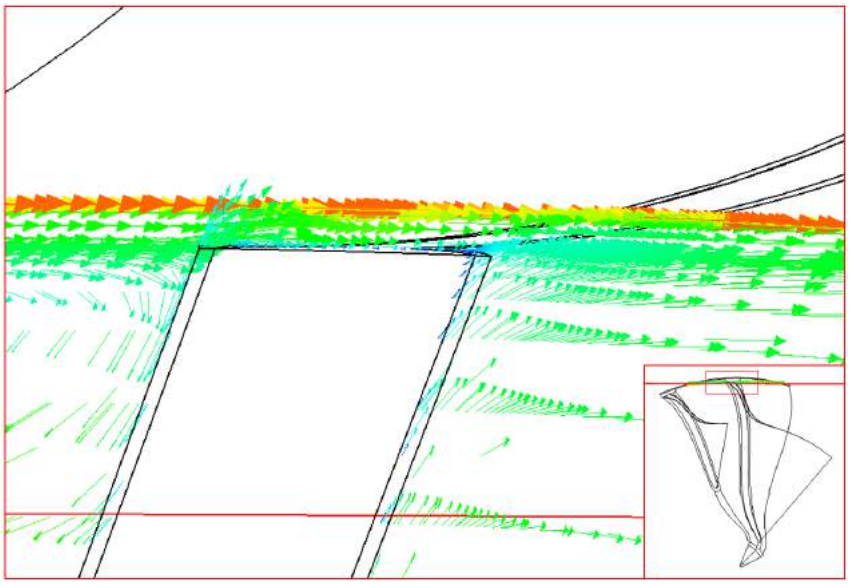

Figure 3.10: Tangential Flow Pattern over trailing edge of Main Blade with 0.2 mm Tip Clearance

Figure 3.11 illustrates the comparison in flow patterns over the trailing edge of the main blade with an increase in tip clearance. By comparing both the flow patterns at the blade trailing edge of the 0.4 mm and 0.6 mm tip clearances to that of 0.2 mm tip clearance, one can see how the increase in tip clearance affects the flow pattern over the trailing edge of the blade tip. As the tip clearance increases the flow is more disturbed due to the increase in mass flow rate over the blades. This causes greater swirl within the main blade channel as more of the flow is entrained into the bypass stream on the suction side of the blade. The swirl decreases the choke margin of the impeller due to it occupying more space midway in the channel.

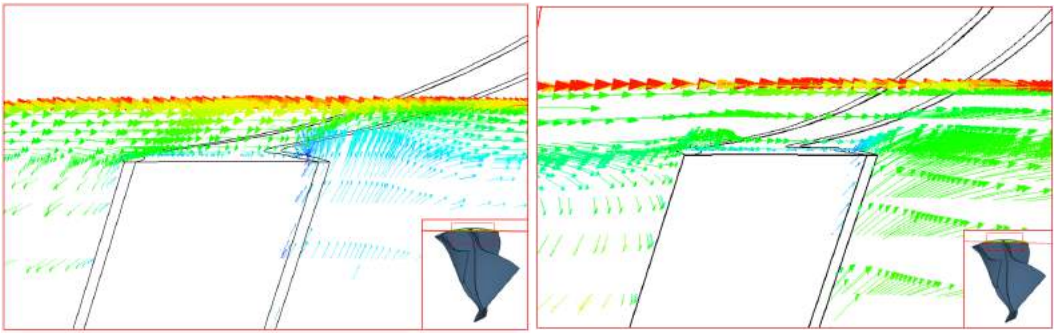

(a) (b)

Figure 3.11: Tangential Flow Pattern over trailing edge of Main Blade with a) 0.4 mm and b) 0.6 mm Tip Clearance

Figure 3.12 below illustrates the radial flow pattern past the trailing edge of the main blades at the outlet of the impeller. From the vectors it can be seen that the flow has an tangential and radial element and a significant vortex that exists right behind the trailing edge. Other than the vortex, the flow field remains fairly uniform.

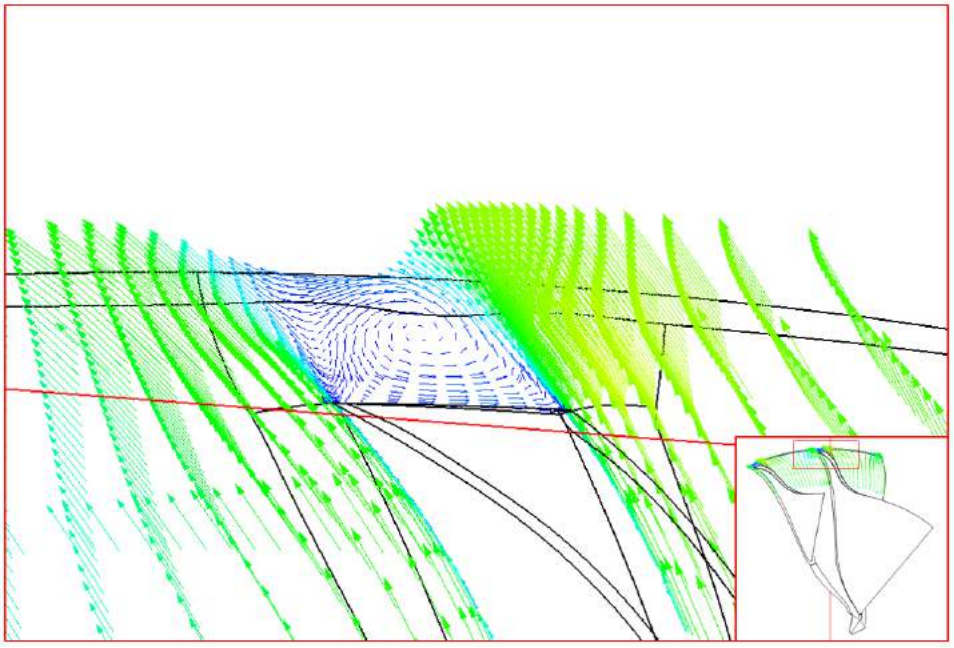

Figure 3.12: Radial Flow Pattern past the trailing edge of the Main Blade with 0.2 mm Tip Clearance

The static pressure at the impeller outlet decreases with increasing tip clearance. From Figure 3.13 below it is seen that the trailing edge vortex increases in size and also causes more of the main channel flow to be drawn in. Therefore the increase in tip clearance decreases the overall performance of the impeller by effectively reducing the deflection of the flow through the impeller.

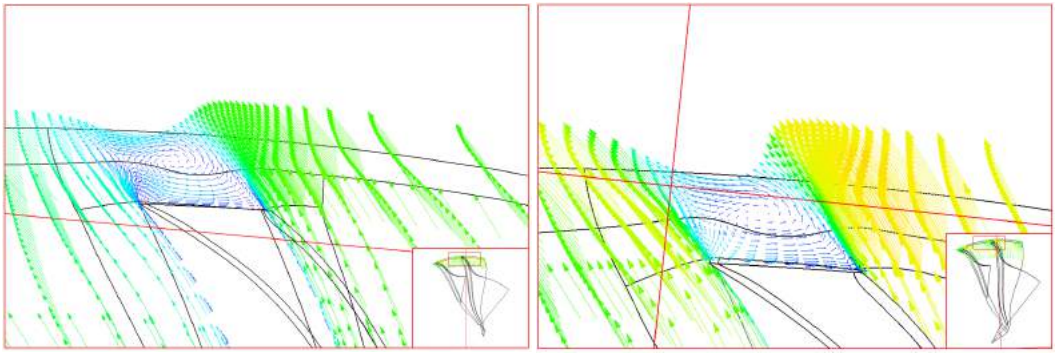

(a) (b)

Figure 3.13: Tangential Flow Pattern over trailing edge of Main Blade with a) 0.4 mm and b) 0.6 mm Tip Clearance

Table 3.2 summarizes and compares the different impeller and diffuser combinations at the impeller's operating point. During the design phase of the im-

peller, Diener designed the impeller to operate with a straight vaneless diffuser which is angled at the same meridional outlet angle of the impeller. Therefore the impeller gave exceptional results using this diffuser type. However, the diffusers used on MGTs are curved and vaned to allow uniform airflow into the combustion chamber. The radial diffuser reduced the predicted total-to-total efficiency by 6% from the original design of Diener. The vaned diffuser is used as the reference point.

Table 3.2: Summary and Comparison of Numerical Results at Operating Point

Design	PR_{t-t}	η_{t-t}	η_{t-t} Increase
Impeller with straight diffuser passage	5.25	86%	6%
Impeller with vaneless diffuser	4.31	77%	−3%
Impeller with vaned diffuser	4.44	80%	0%
Impeller(0.4 mm Clearance) with vaned diffuser	4.24	77%	−3%
Impeller(0.6 mm Clearance) with vaned diffuser	3.88	72%	−6%

Chapter 4

Experimental Phase

4.1 Instrumentation and Hardware

The following section will cover the instrumentation and data acquisition system utilised for the experimental phase of the project. The assembled test bench is shown in figures 4.1 and 4.2 below and will be used as reference throughout the entire chapter.

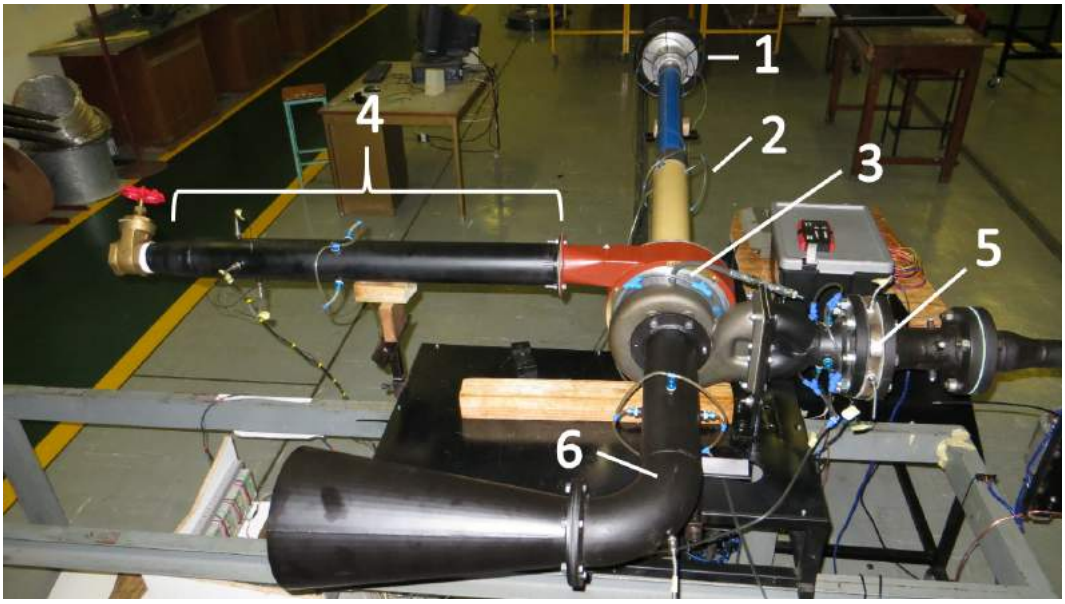

Figure 4.1: Assembled Test Bench

1. Bellmouth - Includes temperature probes (T_{0t}) and pressure taps (P_{0t}).
2. Compressor inlet - Pressure taps (P_{1s}).
3. Diffuser outlet - Pressure taps (P_{3s}).

4. Pressure Measurement station - Temperature probes (T_{4s}) and pressure taps (P_{4s}).
5. Turbine inlet - Temperature probes (T_{ti}) and pressure taps (P_{ti}).
6. Turbine outlet - Temperature probe (T_{to}) and pressure taps (P_{to}).

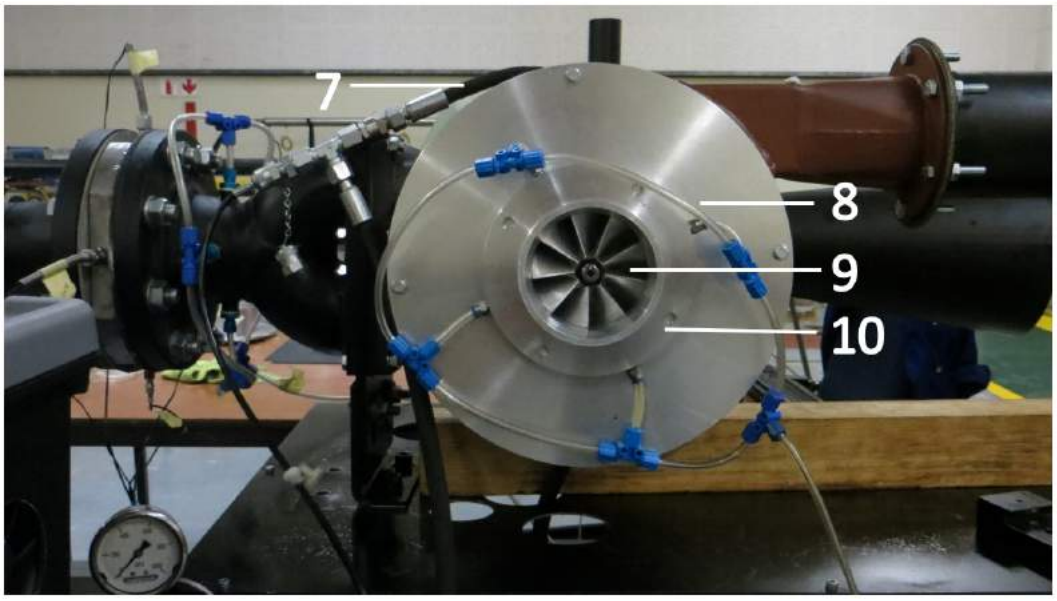

Figure 4.2: Assembled Test Bench - Compressor Intake

7. Lubrication inlet.
8. Compressor outlet - Pressure taps (P_{3s}).
9. Compressor Impeller.
10. Compressor Shroud.

4.1.1 Flow Rate Measurement

The flow rate through the compressor is measured by a bellmouth at the inlet side of the compressor. A differential pressure transducer measures the pressure at the inlet of the bellmouth, relative to the atmosphere. The transducer measures the static pressure at the throat of the bellmouth using four static pressure taps spaced 90^o apart (Struwig, 2014). The flow rate through the turbine is measured with an orifice plate upstream of the turbine. Struwig (2014) designed the orifice plate in accordance with the 1042 British Standard. Struwig (2014) found that the discharge coefficient, C_d, for both instances was 0.96. The equation governing the flow through the bellmouth is given by:

$$\dot{m} = C_d(d^2)E\epsilon\frac{\pi}{4}\sqrt{2\Delta p\rho_1} \tag{4.1.1}$$

For the design of the orifice plate, the diameter ratio β was calculated by Struwig (2014) to be $\beta = 0.526$ using the maximum available supply pressure of 1 MPa, for a mass flow rate of 1 kg/s and a pressure drop of 20 kPa.

4.1.2 Temperature Measurement

Struwig (2014) installed J-type thermocouples from Unitemp Pty (Ltd) to measure the temperature at the following locations:

- at the bell-mouth inlet (Point 1, Figure 4.1), (T_{0t}).
- at the compressor outlet (Point 4, Figure 4.1), (T_{4s}).
- at the turbine inlet (Point 5, Figure 4.1), (T_{ti}).
- at the turbine outlet (Point 6, Figure 4.1), (T_{to}).

The thermocouples are positioned on the compressor side of the test bench according to the ASME test codes which states that four thermocouples per station is required. However only one thermocouple per location was used for the turbine side. The mass flow rate through the compressor is calculated using the total temperature values. Therefore the temperature at the inlet of the compressor is calculated iteratively using the mass flow, measured compressor inlet pressure and bell-mouth inlet total temperature (Struwig, 2014). Half shielded probes are used to measure the temperature at the outlet of the compressor. It is also assumed that the air flow process from the bell-mouth through the compressor is adiabatic.

The measurements taken by the half shielded probes are not adiabatic as kinetic energy is lost due wall-boundary layer effects decelerating the flow. Therefore a dynamic correction factor K is used to correct the measurements of the real probe. The total temperature therefore is given by Benedict (1977) as:

$$T_t = T_p + (1 - K)\frac{c^2}{2C_p} \tag{4.1.2}$$

According to Struwig (2014) a half shielded probe with a dynamic correction factor of $K \approx 0.96$ would be the least sensitive to the effects explained above.

4.1.3 Pressure Measurement

Struwig (2014) configured the pressure monitoring stations according to the ASME test codes. The pressure monitoring stations include several pressure transducers at various locations which are configured in similar fashion for the current compressor test bench as indicated in Figure 4.1. The configuration of these pressure transducers allows the user to measure the static pressure at each location of the compressor test bench. The measurement stations are located at the following positions:

- Bellmouth inlet (Point 1, Figure 4.1), (P_{0t}).
- upstream of the compressor inlet (Point 2, Figure 4.1), (P_{1s})
- Impeller outlet (Point 8, Figure 4.2), (P_{2s}).
- vaneless/cross-over diffuser outlet (Point 3, Figure 4.1), (P_{3s})
- Compressor Outlet (Point 4, Figure 4.1), (P_{4s})

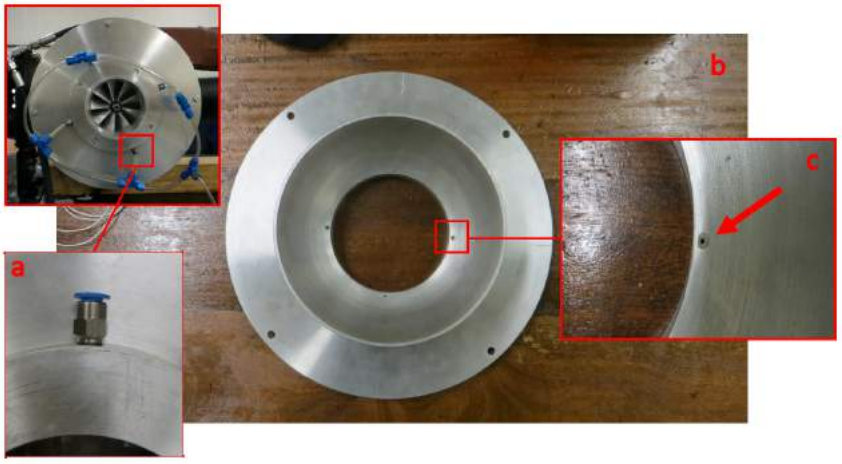

Figure 4.3: Impeller Pressure Tap Holes a) Festo Pressure Fitting b) Impeller outlet pressure tap hole inside of diffuser shroud (Point 8 - Figure 4.2 & Figure A.3) c) Enlargement of pressure tap hole

The pressure tap holes for the compressor and diffuser outlets are shown in figures 4.3 above and 4.4 below respectively. The pressure taps are spaced 90^o apart in the circumferential direction. The pressure at the bellmouth throat is measured using an Endress+Hauser PMD70 differential pressure transducer with a differential pressure range of 3 kPa. All other pressure measurements are done using HBM P8AP absolute pressure transducers which have an operating range of 1 MPa (Struwig, 2014).

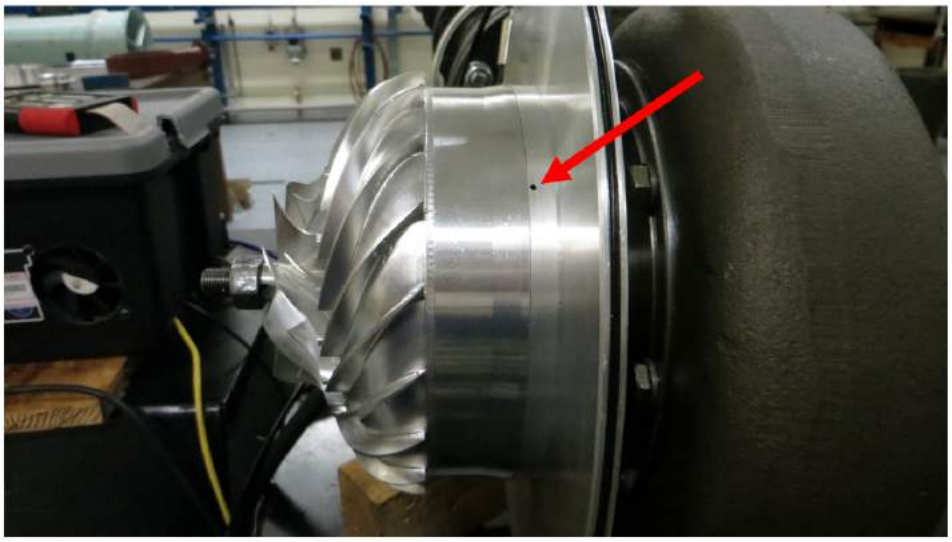

Figure 4.4: Diffuser Pressure Tap Holes

4.1.4 Speed Measurement

Due to the nature of the experiments and the assembly of the test bench it was not possible to use conventional methods of measuring rotational speed such as proximity, magnetic and inductive sensors. It is also important not to disturb the inlet flow field, which further restricted the use of conventional speed measurement devices. To measure the rotational speed of the compressor without affecting the flow field, Struwig (2014) decided on using an optical reflective measurement device to measure the speed of the rotating shaft from a distance. Optical reflective sensors operate either by infra-red or a high concentration of light which is reflected off a piece of the shaft or blade with the advantage of being placed a reasonable distance away.

Struwig (2014) looked at two important aspects to decide which reflective sensor to use, namely, sampling frequency and reflective range. For a signal to be perfectly reconstructed, the Nyquist-Shannon sampling theorem states that the sampling frequency should be greater than twice the frequency of the maximum rotating speed of the shaft, B_{max} (Struwig, 2014).

$$f_s = 2B \tag{4.1.3}$$

Struwig determined the maximum frequency for a shaft with a maximum rotational speed of 121 000 rpm to be:

$$B_{max} = \frac{rpm}{60}$$
$$B_{max} = 2.02kHz \tag{4.1.4}$$

Therefore the minimum sampling frequency was determined to be $f_s = 4.04kHz$, which is above the rotational speed requirement for the Diener (2016) compressor. The OPTEK technology OPB732 Long Distance infra-red Reflective Switch was chosen by Struwig (2014) for its small size and reflective range. The infra-red sensor is placed on the inlet side of the compressor perpendicular to the flow and reflects its signal off a reflector on the compressor nut (4.5). The transistor converts the reflected signal into an AC voltage signal which is interpreted as a positive sinusoidal signal by an oscilloscope.

Figure 4.5: Reflector for speed measurement

A stand alone electronic box was designed and constructed to measure the rotational speed. The electronic box consisted of an Arduino Uno Micro programmable board which is used to interpret the infra-red signal and liquid crystal display to display the rotational speed. Further details regarding design and construction of the electronic box are found in Appendix E

4.1.5 Speed Control

Speed control is achieved by varying the flow rate through the turbine via a control valve upstream of the turbine inlet. The control valve utilises a McLennan Servo stepper motor which is controlled by an Arduino Uno Micro controller. A manual push button is used to control the valve remotely. Manual feedback control from the operator based on the speed measurements were used to determine the positional control of the valve.

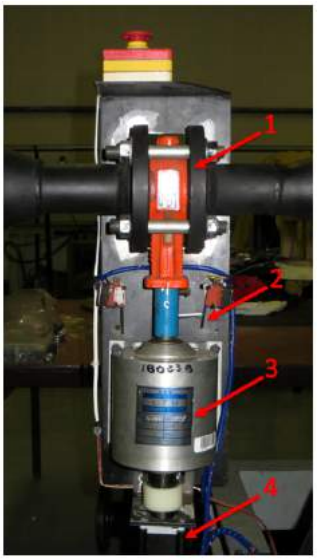

Figure 4.6: Control Valve

Lights indicate whether the control valve is completely open or closed. The control valve (1), micro switches (2) with gearbox (3) and stepper motor control (4) are shown in Figure 4.6 above.

4.1.6 Lubrication System

Lubrication and cooling of the bearings are necessary due to the high rotational speeds of the compressor. The lubrication system was based on a design by Niewoudt (1987). The bearing housing houses three bearings, two of which are angular contact bearings which face each other, which are located on the compressor side and one angular contact bearing with a larger inner diameter which is located on the turbine side. For lubrication purposes the bearings are open on the side which allow oil to be fed through them. Care should be taken to prevent any blockage of the oil feed to the bearings, which can be caused by the oil either being too viscous or containing particles. Any blockage that prevents the oil from lubricating the bearings can prove catastrophic to the test bench.

Concerns regarding the lubrication can be addressed by ensuring correct filtration and heating of the oil (Struwig, 2014). Therefore the oil temperature and pressure is closely monitored. The oil temperature and pressure readings are monitored with a thermocouple and pressure transducer respectively and are displayed on the data acquisition program for real-time feedback. As mentioned above, sufficient heating of the oil will allow for the test bench to operate correctly. To achieve the correct temperature, Niewoudt (1987) implemented a 2 kW low intensity heater to steadily heat the oil to the desired temperature

without burning it. The oil temperature is measured at the oil return side of the test bench and at the oil pump intake using T-type thermocouples. The system also incorporates a bypass to allow the test bench to operate with no lubricant.

Fuchs 15W40 heavy duty multigrade engine oil is used as lubricant, as recommended by most turbocharger suppliers (Struwig, 2014). Before operating the test bench, the oil is first circulated through the system by bypassing the test bench. While the oil is being bypassed it is heated to the desired temperature to reduce its viscosity. This is to prevent the test bench from being put under strain due to the oil viscosity being too high. For operation of the test bench oil is kept at 100 kPa and 50 ^{o}C with a flow rate of 0.5 l/min to prevent oil pressure strain on the bearings and flooding of the test bench. To further limit the possibility of flooding the test bench, the bypass valve was only opened to approximately 25%. The lubrication system is shown in figure 4.7 below:

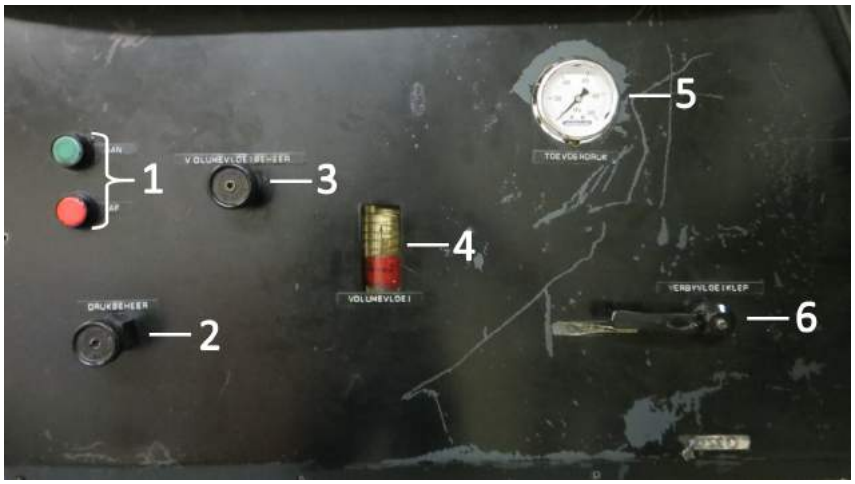

Figure 4.7: Lubrication system control

1. On/Off switch.
2. Pressure control valve.
3. Volume flow rate control valve.
4. Visual flow rate measurement.
5. Pressure gauge.
6. Bypass valve.

4.2 Acquisition of Experimental Data

Struwig (2014) configured the National Instruments^{TM} (NI) CompactRIO (cRIO) and LabVIEW^{TM} 2011 graphical development environment to perform data acquisition (DAQ) of the experiments. cRIO is a reconfigurable chassis which hosts the user field programmable gate array (FPGA) and hot swappable I/O modules. The cRIO consists of an embedded controller for communication and processing of information and is programmed with LabVIEW^{TM} and LabVIEW^{TM} Real-Time application software. Struwig (2014) designed the DAQ using a *Host and Target Application Architecture* for a real-time application laid out by National Instruments^{TM}. A personal computer is normally used as the host and the target is the NI-cRIO computer. A user interface application on the host is used to communicate with the target which receives data from the measurement instruments. Figure 4.8 below illustrates the communication process of the DAQ.

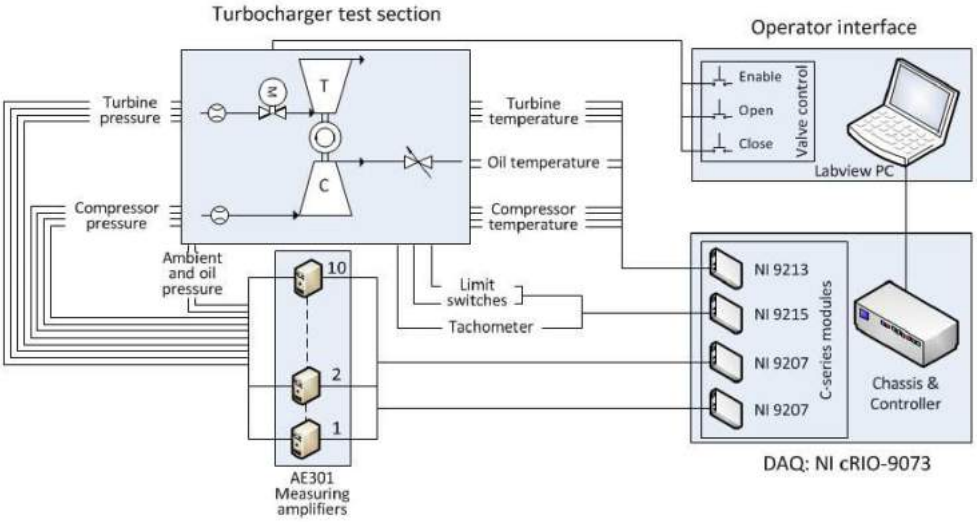

Figure 4.8: Schematic of Data Acquisition System (Struwig, 2014)

A cRIO-9073 with a 266 MHz real-time processor, an FPGA chip and eight expandable C-series module slots is used to sample information from measurement sensors (Struwig, 2014).

The following modules were used:

- 4-channel 100 kS/s, 16 bit, ±10 V Simultaneous Sampling Analogue module (NI-9215).
- An 8-channel Current (4-20 mA) and two combination 8-channel Voltage (±10 V) Analogue modules (NI-9207).

- One 16-channel Thermocouple module (NI-9213).

The target application is run from the FPGA chip and real-time processor which is embedded in the cRIO chassis and controller. The FPGA chip and real-time processor operate together to ensure correct and stable data acquisition. The FPGA samples all measurements. The FPGA allows the user to set the sample rates individually for each of the four acquisition loops, therefore allowing a higher sample rate for the speed measurement without affecting the temperature and pressure data quality (Struwig, 2014). The real-time processor then receives the raw data from the FPGA and converts it to SI units.

As mentioned above, the host application is operated from a personal computer. The application uses a Graphical User Interface (GUI) from where all measurement data can be accessed and monitored. There are two tabs on the GUI to monitor the temperature and pressure sensor readings of the compressor and turbine sides respectively. The one tab also includes the monitoring of the oil temperature and pressure of the lubrication system. Warning indicators are included to check if the oil temperature and pressure are at safe operating conditions and whether the flow control valve is fully open or closed. The ambient conditions are also displayed on the GUI. The GUI is set to save all data to Microsoft Excel .xls format taking 10 samples per second for a duration of 10 seconds (Struwig, 2014).

4.2.1 Measurements

The cRIO-9073 is used as DAQ to take all sensor measurements. Struwig (2014) calibrated the pressure measuring amplifiers (NI-9207) on a 0 - 10 V full scale output per pressure measurement. Each temperature measurement channel (NI-9213) is configured to the type of thermocouple used. LabView^{TM} automatically converts the thermocouple voltage to temperature (in Kelvin). The default polynomial functions used by LabView^{TM} to interpret the thermocouple readings are discussed in Appendix B.

To compensate for the error caused by the contact between the thermocouple and module terminal the NI-9213 comes with a built-in cold-junction compensation. The NI-9207 and NI-9213 modules sample measurements at rates of 500 Hz and 1.2 kHz respectively (Struwig, 2014). The speed measurement is sampled at a rate of 8 kHz per digital input with the Arduino. The sample speed of the Arduino is above that which is required as calculated by Struwig (2014). The rotational speed is determined by measuring the frequency of the optical switch and scaling it to rpm through the Arduino or alternatively using the oscilloscope and scaling the frequency to rpm.

4.3 Experimental Evaluation of a Compressor

The test bench was initially operated at a low rotational speed to prevent any damage to the test bench, allowing for any design or manufacturing faults. This was also necessary to determine a safe lubrication volume flow rate and correct functioning of the instrumentation. Modifications made to the initial test bench design are discussed in detail in Chapter 5.

Recommended test procedures are prescribed by Brun and Nored (2006) and in the ASME PTC-10 test codes for conducting accurate measurements. These include operating the test bench for a minimum of 30 minutes to allow a complete heat soak of the temperature probes or if the measurements have been stable for at least 10 minutes. During working hours and non working hours the air receiver is allowed to have a pressure drop of 4 MPa and 6 MPa respectively. This ensures nominal operating receiver pressure for other external operations (Struwig, 2014).

The receiver capacity does not allow the test bench to undergo a complete heat soak as prescribed by Brun and Nored (2006). It was opted to rather wait for the stabilisation of the measurements which were confirmed through the host application GUI. Before performing any tests the test bench was operated at a speed of 20 000 rpm to ensure correct operation of the assembly and instrumentation. The speed was then increased to 30 000 rpm for 5 minutes before increasing the speed to 40 000 rpm for 10 minutes and then ending the operation to refill the receiver before increasing the speed to 50 000 rpm for testing. This procedure was followed before any measurements were taken. Three sets of preliminary test were done at 30 000 and 40 000 rpm each with each set consisting of 5 test points from choke point to surge. Each test point took approximately two minutes to complete. Including the refill time of the receiver, this procedure allowed the test bench and lubrication to be thoroughly heated before final tests were conducted. Each test was done at an incremental decrease in tip clearance, starting at 0.6 mm to 0.2 mm to investigate the effect of tip clearance on the compressor performance.

The standard deviation is used to determine the validity of measured quantities. A single set of measured quantities per test point, consisting of $N = 100$ samples per test point were used to determine the statistical precision per test point. Since four temperature readings were taken per station, the mean of the pooled means were taken. The pooled mean and pooled standard deviation per test point are determined as follow:

$$\bar{x} = \frac{1}{N}\sum_{i=1}^{N} x_i \tag{4.3.1}$$

$$s = \sqrt{\frac{\sum_{i=1}^{N}(x_i - \bar{x})^2}{N-1}} \tag{4.3.2}$$

Stable compressor operation is determined by observing fluctuations in the measurement data during operation of the test bench, which are permissible when the fluctuations remain within the compressor stability criteria specified by Brun and Nored (2006) and the ASME PTC-10 codes. The compressor stability criteria is provided in table 4.1 below. The AMSE PTC-10 codes calculate the fluctuations though subtracting the minimum test sample from the maximum test sample and then dividing it by the pooled average of the test point as seen in equation 4.3.3.

$$\Delta F = \frac{100(x_{max} - x_{min})}{\frac{1}{n}\sum_{i=1}^{n} x_i} \tag{4.3.3}$$

Table 4.1: Compressor Stability Criteria

Quantity	Brun	ASME
Inlet Pressure	$\pm 1^oC$ of average value	2%
Outlet Pressure	$\pm 1^oC$ of average value	2%
Inlet Temperature	$\pm 1^oC$	0.5%
Outlet Temperature	$\pm 1^oC$	0.5%
Flow	$\pm 10rpm$	0.5%
Speed	$\pm 1^oC$	0.5%

Compressor performance is evaluated by calculating the total conditions at the pressure measurement station, following the ASME PTC-10 methodology while assuming ideal gas behaviour of the air. To calculate the total conditions, the pooled average of the measured quantities were used. The method follows an iterative approach which starts by setting the static temperature (T_{4s}) equal to that of the measured temperature at the pressure measurement station. Then the specific heat at constant pressure (C_p) at the pressure measurement station is calculated. The specific heat at constant pressure is temperature dependent and given by equation 4.3.4 (Cengel and Boles, 2006):

$$\bar{C_p} = \frac{28.11 + (0.1967 \times 10^{-2})T + (0.4802 \times 10^{-5})T^2 - (1.966 \times 10^{-9})T^3}{M} \tag{4.3.4}$$

Where M is the Molar weight of dry air. The static density (ρ_{4s}) and the ratio of specific heats (γ) are calculated at the measurement station, after which the absolute gas velocity (C_4) and Mach number (Ma_4) is calculated. These are used to calculate the total temperature at the pressure measurement station with equation 4.1.2. The new static temperature is calculated from equation 4.3.5:

$$T_{s_{new}} = \frac{T_t}{1 + \frac{(\gamma-1)M^2}{2}} \tag{4.3.5}$$

The new static temperature is compared with the initial static temperature to determine the difference between the two values. The process is iterated until there is an acceptable difference, upon which the total pressure can be calculated by equation 4.3.6:

$$p_t = p_s[1 + \frac{(\gamma-1)M^2}{2}]^{\frac{\gamma}{\gamma-1}} \tag{4.3.6}$$

Once the iterative process above has been completed, the quantities are taken as the total quantities at the pressure measurement station which is 660 mm downstream of the volute exit. In order to compare the measured data with the numerical data the total conditions at the volute exit needs to be calculated. This is done through using the equations that govern compressible adiabatic duct flow with friction also known as Fanno flow (White, 2006). The governing equation assumes that there is no heat added or lost to the system, the cross-sectional area, mass flow rate and stagnation enthalpy remains uniform while only the momentum of the fluid is affected by the internal friction of the duct. To sustain the assumption of adiabatic flow, heat loss from the pipe is assumed to be negligible. The total conditions at the volute exit are dependent on the fluid Mach number. Equation 4.3.7 below relates the fluid Mach number to the internal pipe friction:

$$\frac{\bar{f}L^*}{d} = \frac{1-M^2}{\gamma M^2} + \frac{\gamma+1}{2\gamma} ln[\frac{(\gamma+1)M^2}{2+(\gamma-1)M^2}] \tag{4.3.7}$$

And also equation 4.3.8:

$$(\frac{\bar{f}L^*}{d})_{VoluteExit} = \bar{f}\frac{\Delta L}{d} + (\frac{\bar{f}L^*}{d})_{MeasurementStation} \tag{4.3.8}$$

By substituting the calculated values from the pressure measurement station into the right hand side of equation 4.3.7 the measurement station term of equation 4.3.8 is obtained. Then substituting that term into equation 4.3.8 with the known pipe dimensions ($\Delta L, d$) and friction factor determined from the Reynolds number, one is able to determine the Volute exit term of equation 4.3.8. The volute exit term of equation 4.3.8 is then substituted back

into equation 4.3.7 to solve for the new Mach number at the volute exit. The method follows an iterative approach until the difference between the old and new Mach number at the volute exit is acceptable. The total and static conditions at the volute exit are then determined by compressible flow ratio's.

Sample calculations and MATLAB code used for solving are found in Appendix F and G respectively. The safety and testing procedures that were followed are found in Appendix H.

Chapter 5

Compressor Test Bench Modification and Components

This chapter sets out to explain key components and modifications which contributed to the successful operation of the compressor test bench.

5.1 Key Components

A graphical flow procedure is given in Figure 5.1 below to present a visual summary of the assembly procedure for the test bench. The complete assembly procedure can be found in Appendix A.

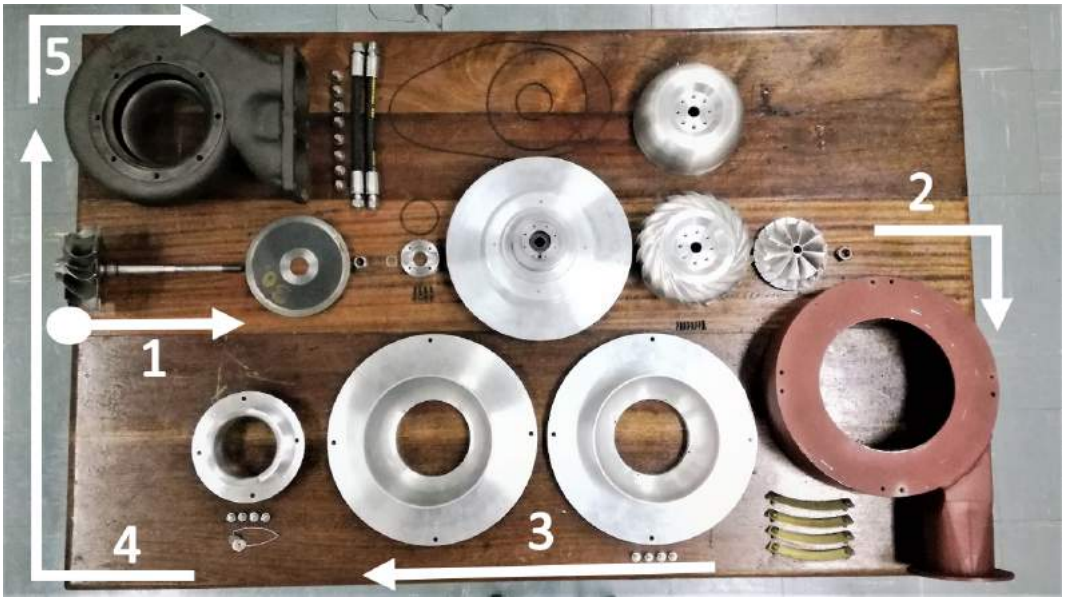

Figure 5.1: Graphical flow of Assembly

5.1.1 Impeller, Diffuser and Shroud

The impeller, diffuser and shroud are the components that make up the geometry of the compressor section of the test bench. The impeller (Figure 5.2a) imparts energy to the fluid by compressing the fluid via rotation. The compressed air is then diffused through the diffuser (Figure 5.2b). The cross-over (vaned) diffuser is specifically designed for static pressure recover, which helps to further increase the fluid's static pressure before entering the combustion chamber. The impeller and diffuser shroud (Figures 5.2c and 5.2d) form part of the geometry. The impeller shroud is adjusted to determine the blade tip clearance at the TE. All of the parts were made of Aluminium with the impeller machined from Al 7075-T6. Figure 5.2 displays all the components that form part of the channel geometry.

Figure 5.2: Compressor Test Bench Key components: a) Impeller, b) Cross-over Diffuser, c) Impeller Shroud and d) Diffuser shroud

5.1.2 Bearings

The impeller is designed to operate at 95 000 rpm and therefore the bearings will have to operate at the same rotational speed with oil lubrication. Due to the nature of the experimental setup, high speed and high precision bearings

are needed. It is anticipated that the back pressure from the compressed air feed will act as a force on to the inducer face of the turbine. This pressure force is transferred through the shaft shoulders on to the inner races of the bearings. The maximum permissible force a bearing can withstand axially on its inner race is referred to as the dynamic loading of the bearing. When the maximum loading of the bearing is exceeded, bearing failure may occur. A quick calculation shows that the bearings combined will have to endure a maximum dynamic loading of approximately 5.7 kN due to the compressed air. The *Xtreme 012 7002-15º UL/CSB P4* bearing was selected due to its speed and dynamic load rating. The *Xtreme* bearing has a dynamic load rating of 5.2 kN per bearing and an oil lubricated operating speed of 100 000 rpm. The compressor side bearings are placed facing each other to allow them to counter thrust in both directions with the turbine bearing (*GRW D6903/608147 15º*) also countering forward thrust.

5.1.3 Turbine Shaft Modification

It was discovered during the initial assembly process of the compressor test bench that the bearing layout on the shaft did not allow for the inner races of the bearings to be secured into position. Figure 5.3 shows the initial bearing layout for the test bench with point 2 indicating the missing shoulder. From the drawing it is seen that once the impeller is bolted into place, the inner races of the bearings experience a compression force towards each other as the compressor nut pulls the shaft to itself.

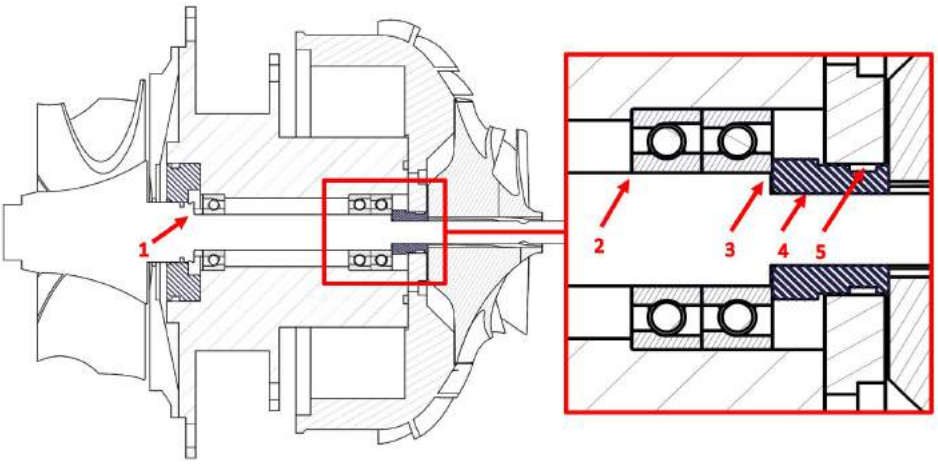

Figure 5.3: Previous Test Bench Bearing Layout

From the enlarged area it is seen that the force from the impeller bolt is transferred through the spacer (Point 4, Figure 5.3) on to the inner races of the bearings (Points 1 & 3, Figure 5.3) with no shoulder (Point 2, Figure 5.3) to counter the force. This compression force on the bearings caused them to lock, which kept the shaft from rotating freely. This was overcome by adding a shoulder (Point 3, Figure 5.4) to the shaft which pressed against the inner races of the bearings on the impeller-side, as seen on the enlarged image in Figure 5.4. The shaft is then constrained axially to the impeller-side bearings through the shaft shoulder and spacer (Point 3 and 4 respectively, Figure 5.4) which press against the inner races of the bearings. A clearance of 1 mm was left between the first shaft shoulder and spacer at point 4. A circlip (Point 5, Figure 5.4) was added to the bearing housing to constrain the impeller-side bearings in position. Figure 5.4 below displays the modified bearing layout and how the shaft is constrained axially.

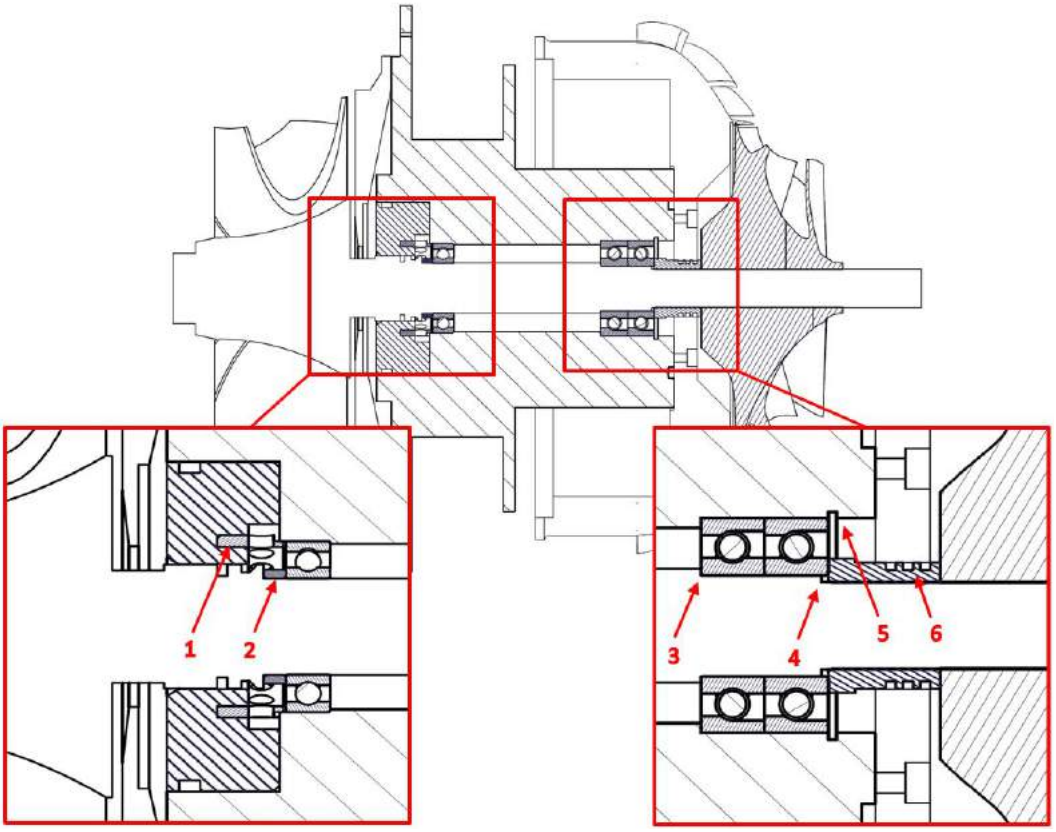

Figure 5.4: Current Test Bench Bearing Layout

The impeller-side spacer (Point 4, Figure 5.3) was also modified after the split rings (Point 5, Figure 5.3) which sealed the bearing housing seized due to interference with one another. Three individual grooves were cut into the spacer (Point 6, Figure 5.4) for the split rings not interfere with one another.

A third split ring was added to aid in the prevention of lubricant leakage. The modified compressor spacer can be seen in Figure 5.5a below.

(a)

(b)

Figure 5.5: Modifications: a) Impeller-side Spacer and b) Bearing Outer-race Securing Ring

The bearing outer race on the turbine side is kept in position through a specially designed ring (Point 1, Figure 5.4) as there was insufficient space for a circlip. The ring was designed with holes to allow lubricant to easily flow through. The turbine outer race securing ring can be seen in Figure 5.5b above. The small spacer (Point 2, Figure 5.4) on the turbine side is positioned within the assembly to further counter thrust. The old and modified shafts are displayed in the Figures 5.6a and 5.6b below. From the Figures below, the added shoulder in the middle of the new shaft can be clearly seen.

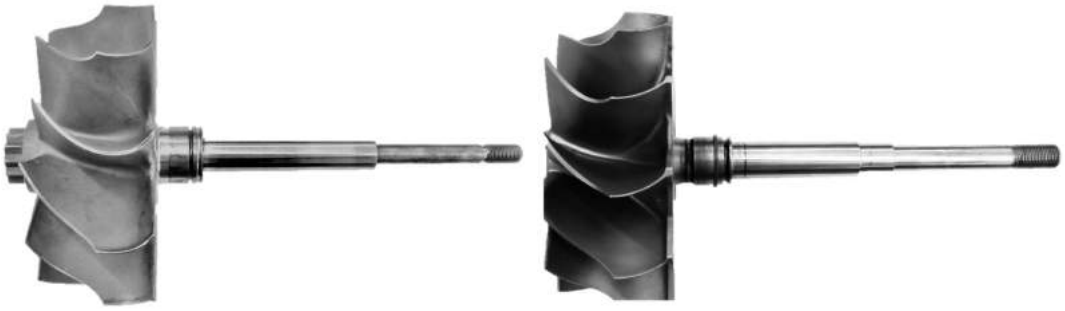

(a) (b)

Figure 5.6: Shaft Modification: a) Old Shaft and b) New Shaft

With the new modified shaft the bearing housing and turbine oil seal had to be modified as well to accommodate the modifications. The modifications to the shaft proved to be successful. The shaft is now able to rotate freely and operate under fine tolerances.

5.1.4 Modifications to Shroud Assembly

It was found that both the cross-over diffuser and vaneless diffuser was not concentric around the shaft and caused the shaft to be misaligned. This was overcome by designing an annulus that fitted between the Compressor Bearing housing (Figure A.9) and the Rear Diffuser Adapter plate (Figure A.10). The rear diffuser adapter plate is directly in contact with the diffusers. It was also realised during the assembly of the test bench that the diffuser shroud has no shoulder to align it concentrically around the scroll and therefore made it difficult to place the impeller shroud concentrically around the impeller. Concentricity was accomplished through trial and error using the 0.2 mm diameter copper strands (Figure 5.7) to ensure the impeller shroud is concentric around the blades. Adding a shoulder to the diffuser shroud will aid in maintaining the accuracy of the blade tip clearance around the LE of the impeller.

5.2 Tip Clearance Measurement

The impeller has been designed with a blade tip clearance of 0.2 mm for the compressor to achieve its design point efficiency. It is important to achieve this blade tip clearance experimentally in order to validate the numerical solution. Measuring the blade tip clearance at the trailing edge of the blade when the test bench is assembled is very difficult. This was overcome by using adhesive to fasten copper strands of 0.2 mm, 0.4 mm and 0.6 mm to the inside of the shroud (refer to Figure 5.7). By knowing the diameter of the strands it was now possible to confirm the trailing edge blade tip clearance once the blades interfere with the copper strands.

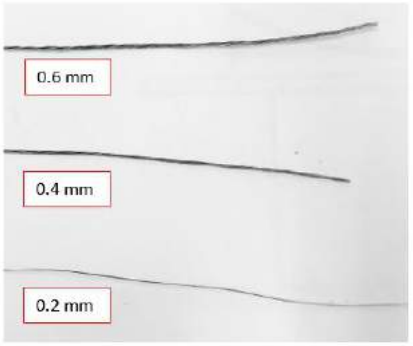

Figure 5.7: Tip Clearance Measuring strands

The shroud was assembled and the rotor turned to listen for interference between the blades and copper strand (refer to Figure 5.8). An iterative process was followed until a tip clearance of 0.2 mm was achieved through modifying and shifting the shroud. It was ensured that when the shroud was assembled that the blade tip clearance was 0.2 mm from the leading edge (LE) to the trailing edge (TE) of the blades. To achieve one of the objectives, namely investigating the effect of trailing edge blade tip clearance on impeller performance, spacers were made for the shroud assembly bolts to adjust the tip clearance at the TE in 0.2 mm increments.

Figure 5.8: Tip Clearance Measurement

5.3 Post Experimental Condition of Components

Inspection of the impeller blades, shroud and bearings was continually done throughout the experimental phase to ensure early detection of any damage that might have occurred during testing. After the first tests were conducted at 50 000 rpm, it was discovered that the leading edge of the impeller blades up to mid point had made contact with the shroud during operation. Both the main and splitter blades were affected. The effect of blade contact with the shroud can be seen in Figure 5.9 below.

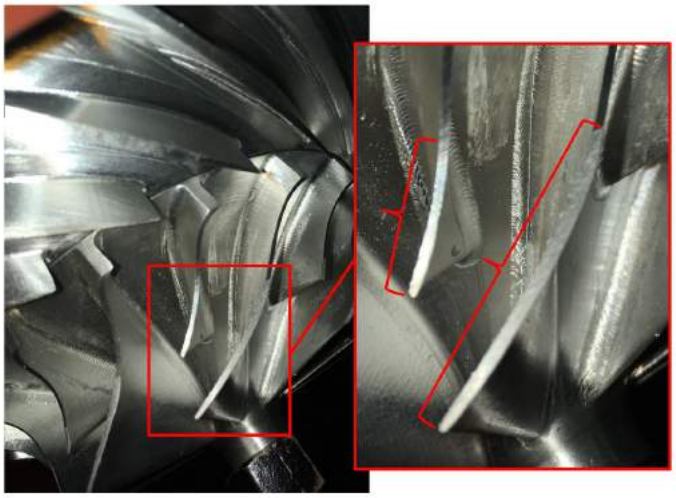

Figure 5.9: Effect of Blade interference with Shroud

From the image it is seen that the LE of the blades has been eroded, but with minimal effect on the shroud. According to the design literature, only the aero-mechanical loading of the blades were taken into consideration and no thermal loading. Under these conditions the total displacement was found to be 0.24 mm at the LE of the impeller in the negative axial direction at a rotational speed of 95 000 rpm, which was considered acceptable (Diener, 2016). At 50 000 rpm the thermal load on the blades and shroud are in the order of 60 ^oC, therefore it is concluded that both the blades and shroud simultaneously underwent thermal expansion which caused them to interfere with one another. The damage caused to the shroud interior can be seen from Figure 5.10 below. The impeller and shroud were cleaned and the scuff marks removed before further tests were conducted. An approximate 0.05 mm of the blade's leading edge was lost as a results of the interference with the shroud.

Figure 5.10: Effect of Blade interference on Shroud

The bolts securing the diffuser shroud to the scroll (see Appendix A, Figure A.1), and the impeller shroud to the diffuser shroud started to show signs of fatigue as testing continued. The cyclic fastening of the bolts and thermal expansion of the material caused the bolts to weaken and narrow as seen in Figure 5.11a. It is recommended that the bolts used for securing the shrouds be replaced regularly.

During the experimental phase it was discovered that lubricant leaks into the compressor test section while the air receiver tank is charged and during operation of the test bench. This is due to the viscosity of the oil being lower at 50 ^oC. From Figure 5.11b the extend of the accumulated lubricant can be seen between test runs. While operating at 50 000 rpm the lubricant evaporates due to the air velocity and the impeller swirling the lubricant outwards, causing the lubricant to mix with the warm pressurised air.

(a) (b)

Figure 5.11: Post Experimental Inspection: a) Fatigued Bolt b) Leaked Lubricant

The effect of the accumulated lubricant is considered negligible, however care should be taken to ensure that the pressure taps and piping leading up to the pressure transducers remain clear of lubricant as this can drastically affect the measurements.

The bearings, modified impeller-side spacer and split rings were all in perfect working condition after the testing of the impeller and cross-over diffuser was concluded. The tests were conducted successfully and indicates that the modifications made to the compressor test bench were successful.

Chapter 6

Experimental and Numerical Results

The previous chapters covered the design and numerical analysis of the impeller and diffusers, as well as the experimental set-up and evaluation of the test bench. This chapter sets out to evaluate the performance of the impeller with the respective diffusers. The results are used to validate the numerical results obtained in chapter 3. The results are divided into two sections namely tests conducted with the cross-over diffuser and tests conducted with the vaneless diffuser. Each section will discuss the experimental and numerical results, and draw up a comparison between the experimental and numerical results. The corrected mass flow parameter, $\dot{m}\sqrt{T_{t1}}/p_{t1}$ and normalised speed, $N/\sqrt{T_{t1}}$, are used as non-dimensional values to accurately compare the experimental results with the numerical results.

6.1 Cross-over Diffuser

6.1.1 Experimental Results

As mentioned in chapter 4 the compressor test bench was operated at 50 000 rpm due to the limited capacity of the air receiver. The trailing edge blade tip clearance was also adjusted as mentioned in chapter 5 from 0.2 mm to 0.6 mm to investigate the effect it has on the performance of the impeller. Given below in figures 6.1a, 6.1b and 6.1c are the total-to-static pressure ratios (PR_{t-s}) at the impeller, diffuser and volute outlet for each blade tip clearance. From the Figures a noticeable decrease in performance of the impeller is seen with each incremental increase in blade tip clearance. The effect that the trailing edge blade tip clearance has on impeller performance is more clearly observed at the diffuser outlet than at the volute exit.

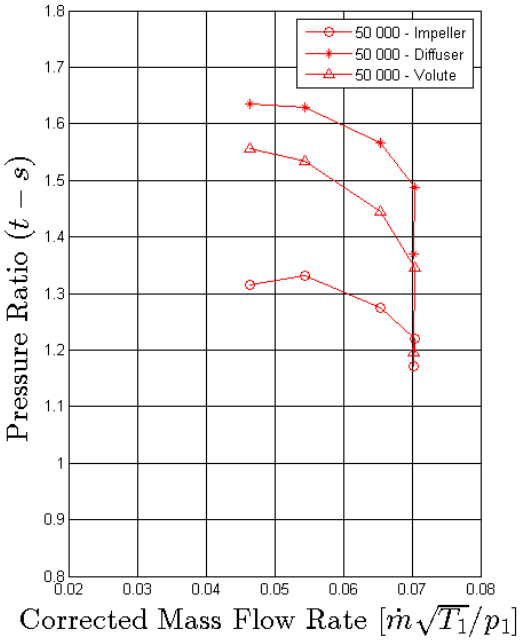

(a) 0.2 mm

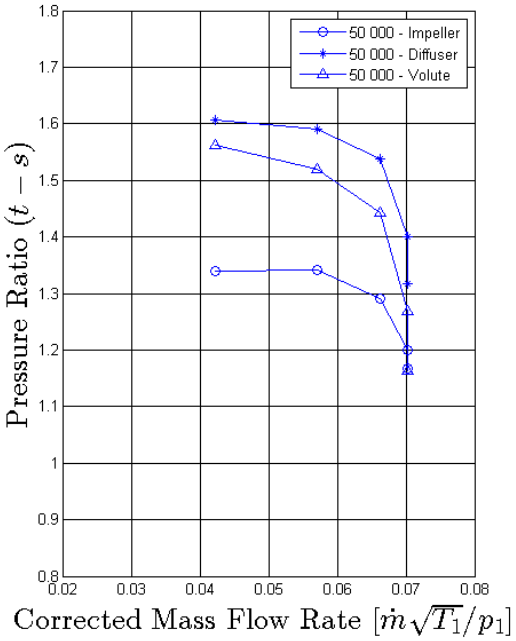

(b) 0.4 mm

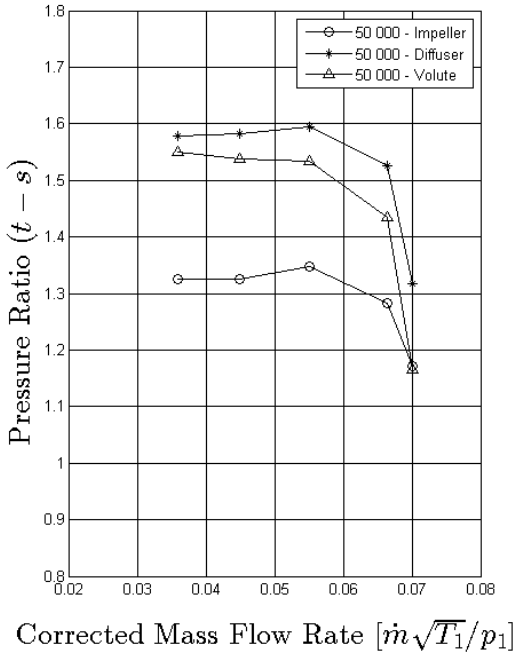

(c) 0.6 mm

Figure 6.1: Impeller with Cross-over diffuser Total-to-Static Pressure Ratio with Blade Tip Clearance of: a) 0.2 mm, b) 0.4 mm and c) 0.6 mm

Figure 6.2a below shows the decrease in total-to-total pressure ratio with each

incremental increase in blade tip clearance. There is a 1.9% decrease in total-to-total pressure ratio at the best efficiency point by increasing the tip clearance from 0.2 mm to 0.4 mm. The decrease in performance when increasing the tip clearance from 0.4 mm to 0.6 mm is not that noticeable except near the surge margin. From the figure it is seen that the choke point remains the same for each tip clearance with an increase in surge margin as the blade tip clearance is increased.

Figure 6.2b compares the isentropic efficiencies of each blade tip clearance with each other. No conclusion can be made whether the blade tip clearance has any effect on the efficiency as the only decrease in efficiency is seen with the 0.4 mm tip clearance according to Figure 6.2b.

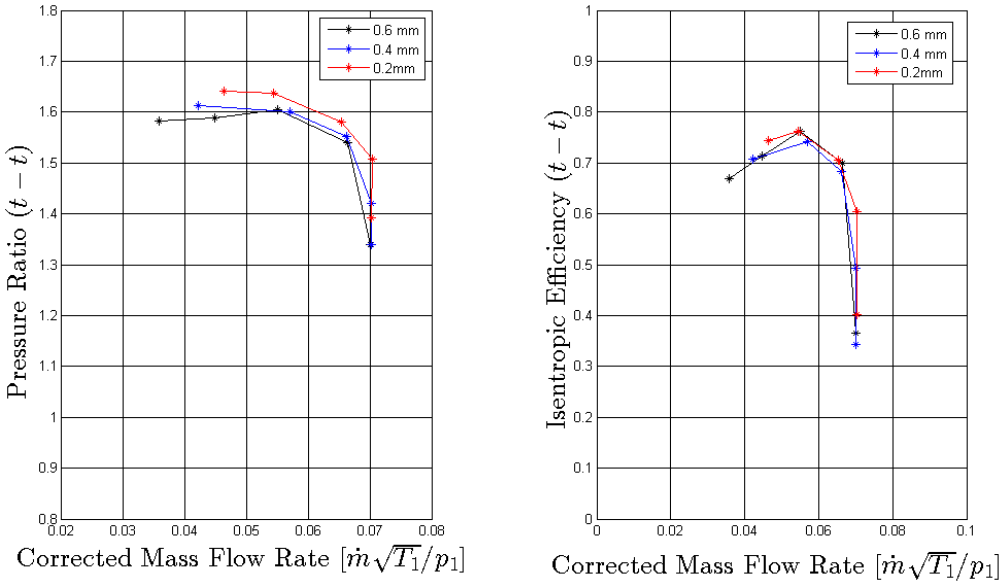

(a) (b)

Figure 6.2: Impeller with Cross-over diffuser a) Total-to-Total Pressure Ratio and b) Total-to-Total Isentropic Efficiency for 0.2 mm, 0.4 mm, 0.6 mm blade tip clearances

The effect of trailing edge blade tip clearance on the total-to-total temperature ratio (TR_{t-t}) is observed in Figure 6.3. From Figure 6.3 it is seen that the TR_{t-t} of both the 0.2 mm and 0.6 mm tip clearance are the same, but that a higher TR_{t-t} is measured for the 0.4 mm tip clearance. The discrepancy regarding the TR_{t-t} can be attributed to the change in compressor inlet temperature conditions as the same behaviour is observed when applying normalised conditions to the numerical solution. The behaviour of the TR_{t-t} with

increase in tip clearance and compressor inlet conditions coincides well with that of the numerical results as seen in Figure 6.4c.

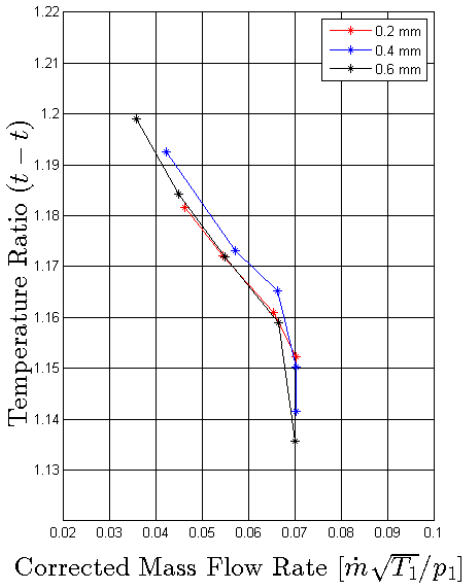

Figure 6.3: Impeller with Cross-over diffuser Total-to-Total Temperature Ratio for 0.2 mm, 0.4 mm and 0.6 mm blade tip clearance

6.1.2 Numerical Results

Numerical simulations were also performed at 50 000 rpm for the impeller with cross-over diffuser to compare the experimental results with the numerical results. Figures 6.4a, 6.4b and 6.4c below illustrate the total-to-total pressure ratios, isentropic efficiencies and temperature ratios at the diffuser outlet for the respective tip clearances.

The numerical results predict a decrease in total-to-total pressure ratio of 0.61% when increasing the tip clearance from 0.2 mm to 0.4 mm. A further decrease of 0.61% in total-to-total pressure ratio is found when increasing the tip clearance to 0.6 mm. A decrease in performance is also observed w.r.t. the total-to-total efficiencies and temperature ratios, as seen with the experimental. While the numerical results predict a linear decrease in performance, the experimental results show a non-linear decrease in performance. This, as explained above, could be attributed to the compressor inlet conditions. At lower mass flow rates the TR_{t-t} exhibits similar behaviour as the experimental results, but deviates from the experimental results at higher mass flow rates.

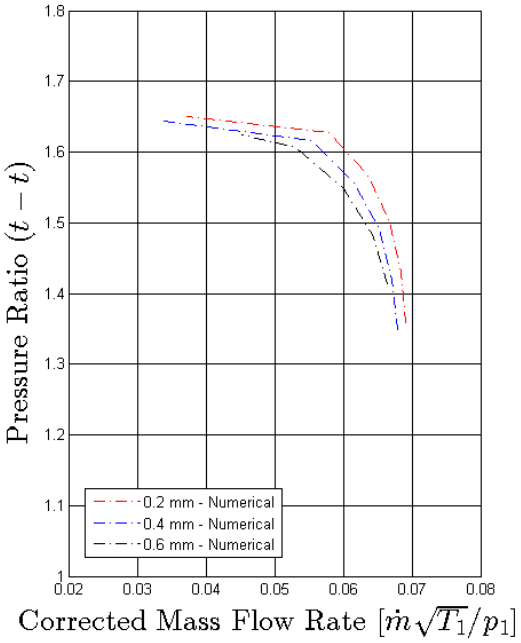

(a)

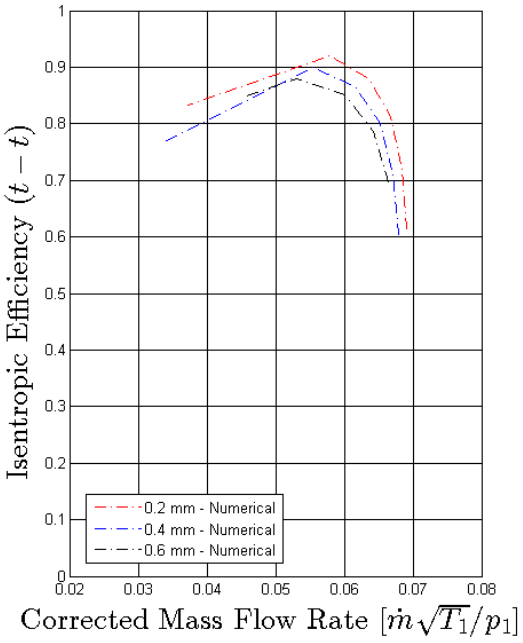

(b)

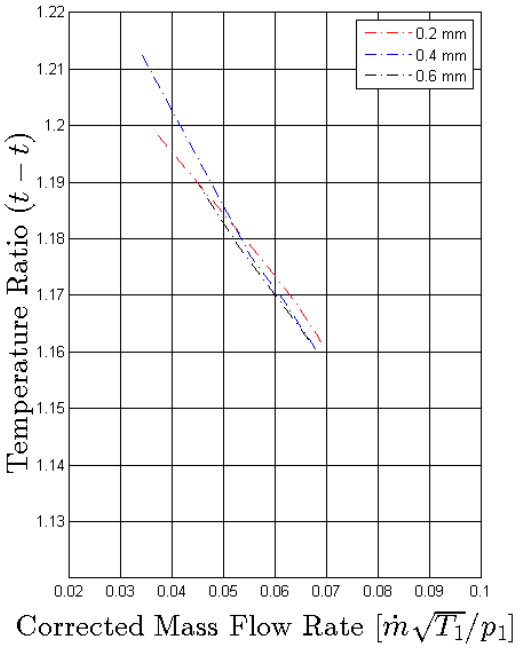

(c)

Figure 6.4: Impeller with Cross-Over diffuser a)Total-to-Total Pressure Ratio, b) Total-to-Total Isentropic Efficiency and c) Total-to-Total Temperature Ratio for 0.2 mm, 0.4 mm and 0.6 mm blade tip clearance

6.1.3 Comparison between Experimental and Numerical Results

Figures 6.5a, 6.5b and 6.6 below show the compressor total-to-total pressure ratio at the diffuser outlet compared with the numerical solutions obtained from NUMECA for the respective blade tip clearances. The experimental results compare well with the numerical, with each intersection on each graph being near the operating point of the compressor. When operating the impeller with a 0.2 mm tip clearance (Figure 6.5a) it is observed that the experimental results closely follow the numerical results. There is however a small offset in results when comparing the choke margin. The operating points of both the 0.4 mm and 0.6 mm tip clearance results coincide well with the numerical results. However, the deviation between experimental and numerical choke margins become greater as the blade tip clearance is increased, although the trend of the numerical results is still closely followed.

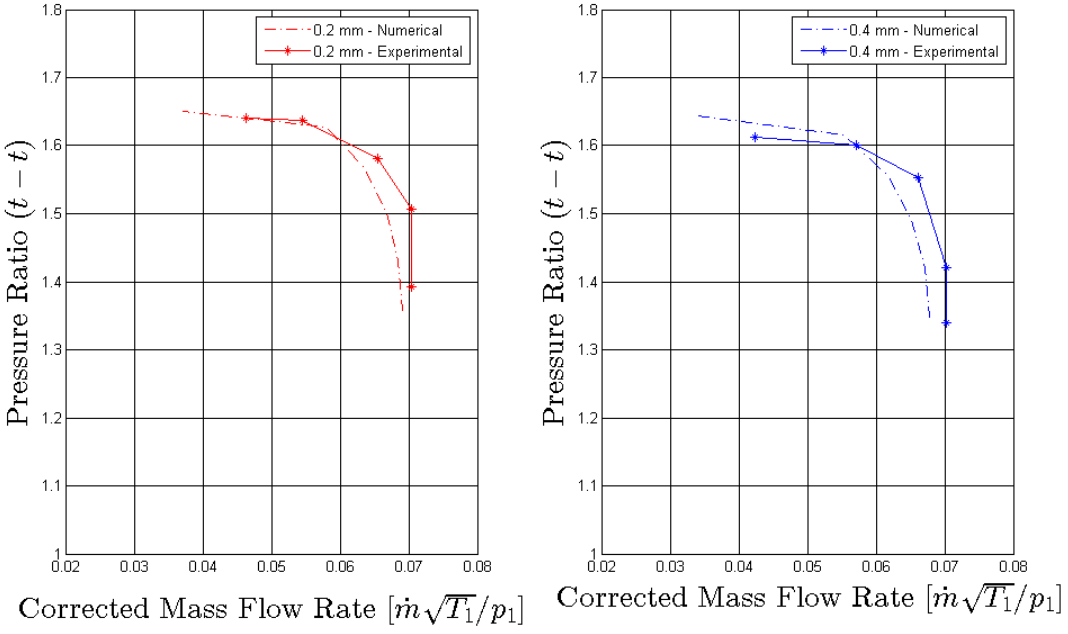

(a) 0.2 mm (b) 0.4 mm

Figure 6.5: Compressor Total-to-Total Pressure Ratio at the Cross-over diffuser outlet with Blade Tip Clearance of: a) 0.2 mm and b) 0.4 mm

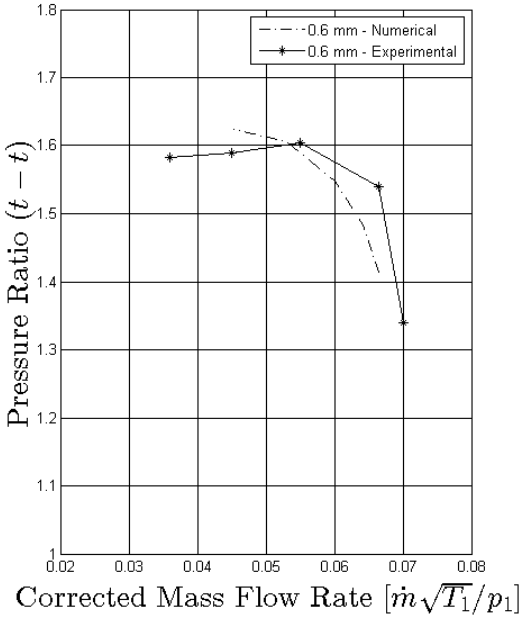

Figure 6.6: Compressor Total-to-Total Pressure Ratio at the Cross-over diffuser outlet with Blade Tip Clearance of 0.6 mm

The comparison between the experimental and numerical total-to-total efficiencies are given in figures 6.7a, 6.7b and 6.7c below. Contrary to the experimental pressure ratio results, the total-to-total isentropic efficiencies have a greater offset from the numerical results. From observation it is seen that the deviation decreases with an increase in blade tip clearance. Besides the offset, the trend of the numerical curves is still followed by the experimental.

The difference in results can be attributed to NUMECA overestimating the isentropic efficiency due to the applied adiabatic assumption within the numerical setup. The adiabatic assumption does not hold for the experimental setup as energy is lost in the system before reaching the pressure measurement station.

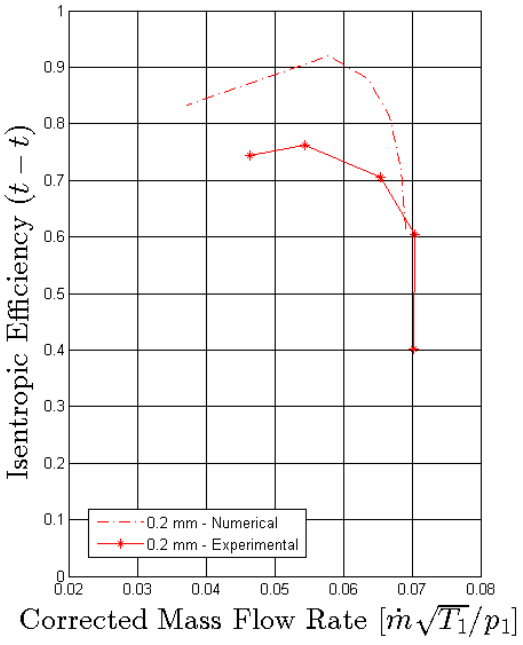

(a) 0.2 mm

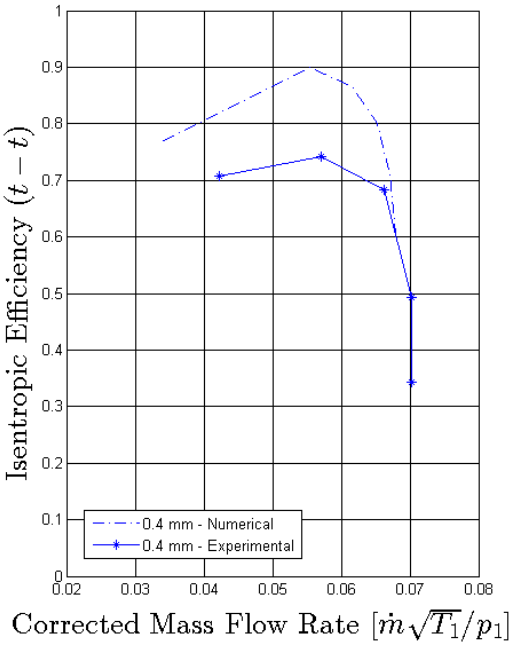

(b) 0.4 mm

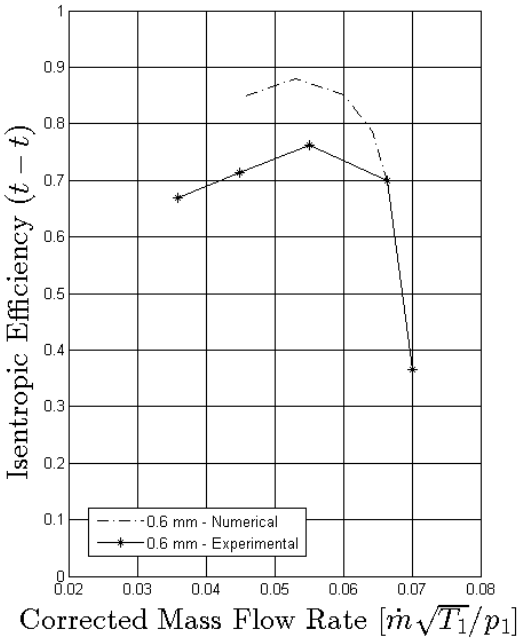

(c) 0.6 mm

Figure 6.7: Compressor Total-to-Total Isentropic Efficiencies at the Cross-over diffuser outlet with Blade Tip Clearance of: a) 0.2 mm, b) 0.4 mm and c) 0.6 mm

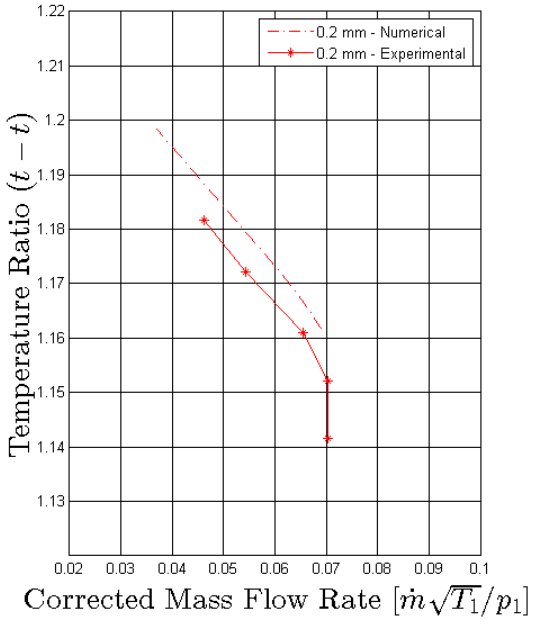

(a) 0.2 mm

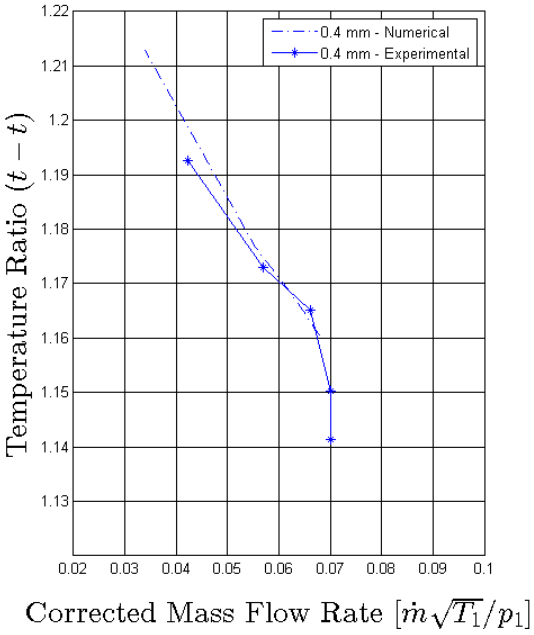

(b) 0.4 mm

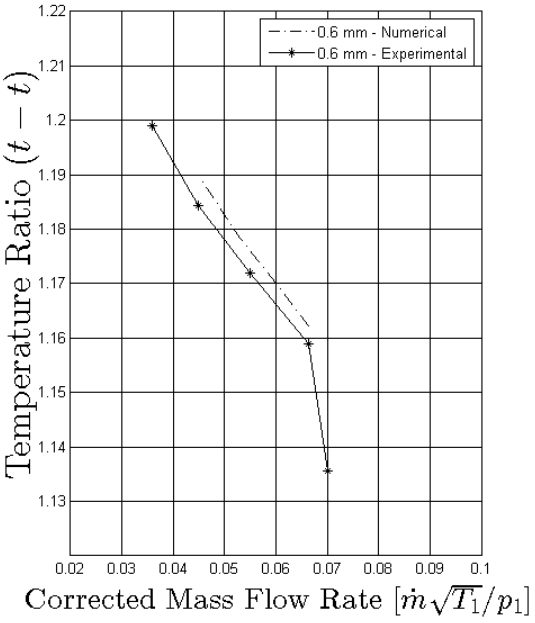

(c) 0.6 mm

Figure 6.8: Compressor Total-to-Total Temperature Ratio at the Cross-over diffuser outlet with Blade Tip Clearance of: a) 0.2 mm, b) 0.4 mm and c) 0.6 mm

The total-to-total temperature ratios (TR_{t-t}) at the cross-over diffuser outlet are represented in Figures 6.8a, 6.8b and 6.8c above. Comparing the numerically predicted TR_{t-t} with that of the experimental at 0.2 mm tip clearance, one can see an offset in results which is greater than that of the 0.4 mm and 0.6 mm tip clearances. This offset has been attributed to the change in compressor inlet conditions during the experimental phase as mentioned above. For the 0.4 mm tip clearance the experimental results closely follow that of the numerical prediction with a minimal deviation at lower mass flow rates. With the 0.6 mm tip clearance, the experimental results show a small offset from the numerical results as seen with the 0.2 mm tip clearance.

Overall the experimental results agree well with the numerical results, with both methods capturing the effect that the trailing edge blade tip clearance has on the performance of the impeller with cross-over diffuser. The effect of trailing edge blade tip clearance on impeller performance agrees well with the work of Danish (2006) and Pandurangadu (2014).

Summarising the results, the maximum PR_{t-t} obtained experimentally for the 0.2 mm blade tip clearance was 1.64. A design point PR_{t-t} of 1.637 and an isentropic efficiency of (η_{t-t}) of 76% was obtained corresponding to a mass flow rate ($\dot{m}$) of 0.30 kg/s. The experimental results of the cross-over diffuser at best efficiency point (BEP) are summarised in Table 6.1 below:

Table 6.1: Summary of Impeller with Cross-over diffuser Performance (BEP)

Blade Tip Clearance	PR_{t-t}	η_{t-t}	$\dot{m}_{design}[kg/s]$	Operating range
0.2 mm	1.63	76.3%	0.30	34.1%
0.4 mm	1.60	74.1%	0.32	39.8%
0.6 mm	1.60	76.0%	0.30	48.8%

6.2 Vaneless Diffuser

6.2.1 Experimental Results

Figures 6.9a, 6.9b and 6.9c represent the total-to-static pressure ratios (PR_{t-s}) at the impeller, diffuser and volute outlets at blade tip clearances of 0.2 mm, 0.4 mm and 0.6 mm respectively for the vaneless diffuser. It is noted that the choke margin remains the same in all three instances with only the surge margin increasing with an increase in blade tip clearance. All three graphs exhibit the same results w.r.t. PR_{t-s}, regardless of the blade tip clearance, which was not predicted by the numerical solution.

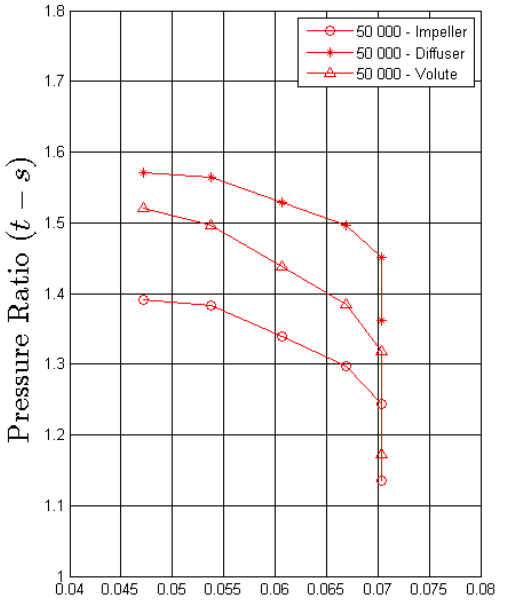

(a) 0.2 mm

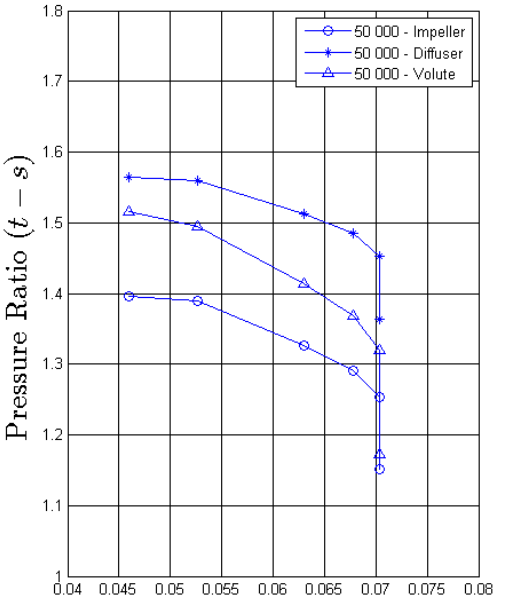

(b) 0.4 mm

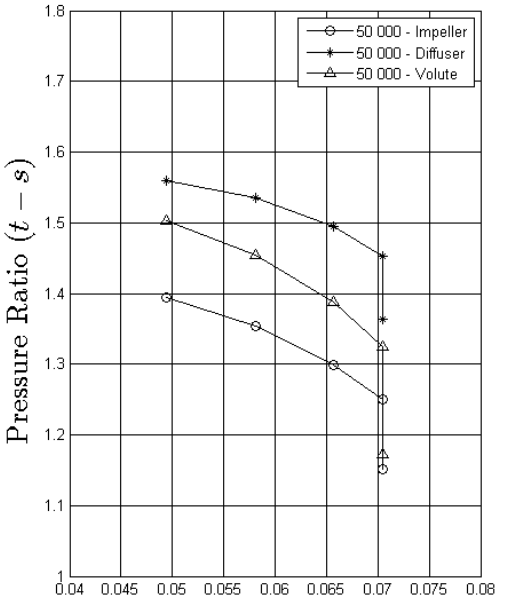

(c) 0.6 mm

Figure 6.9: Impeller with Vaneless diffuser Total-to-Static Pressure Ratio with Blade Tip Clearance of: a) 0.2 mm, b) 0.4 mm and c) 0.6 mm

Further examination of the test bench found that there was a 1.5 mm step within the vaneless diffuser geometry at the impeller outlet which was unaccounted for during preliminary numerical analysis. The step in the geometry is a result of manufacturing tolerances not being met. The manufacturing deficit caused the whole diffuser shroud to be shifted 1.5 mm in the negative x direction as seen in Figure 6.12 (section 6.2.2). This creates a larger vaneless space for the flow to diffuse which allows more energy to be dissipated due to swirl. The step also creates a recirculation bubble at the impeller-outlet diffuser-inlet intersection which further dissipates the flow energy. Further details regarding the step within the channel geometry are discussed in chapter 6.2.2.

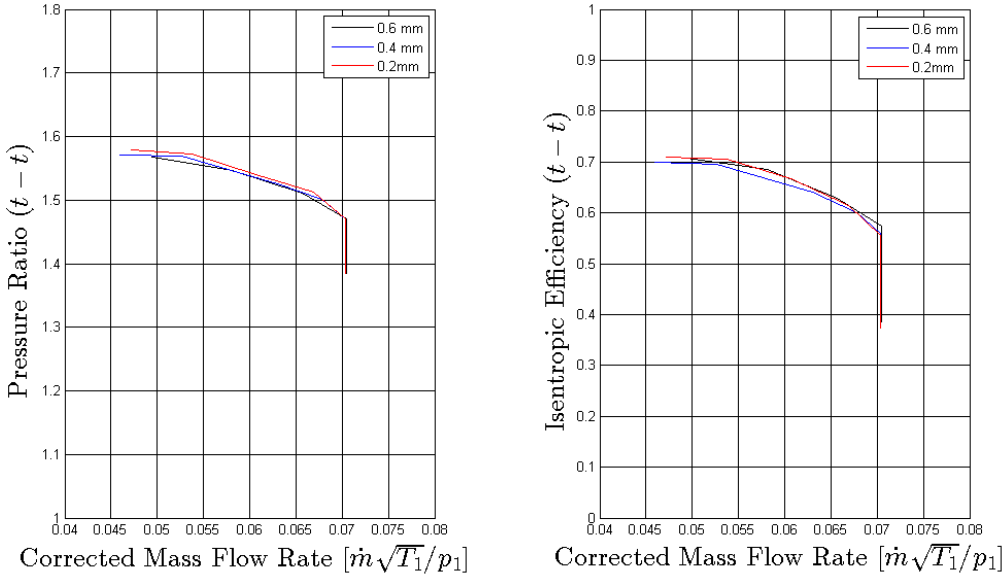

(a) (b)

Figure 6.10: Impeller with Vaneless diffuser a) Total-to-Total Pressure Ratio and b) Total-to-Total Isentropic Efficiency for 0.2 mm, 0.4 mm and 0.6 mm blade tip clearances

The influence of the step within the geometry can be seen more clearly from Figures 6.10a and 6.10b above, as both graphs indicate a negligible difference in impeller performance regardless of blade tip clearance. The same negligible effect on impeller performance w.r.t. TR_{t-t} can be seen in Figure 6.11 below. From the Figure it is seen that only the 0.6 mm blade tip clearance showed an effect on the impeller performance, which could be attributed to sufficient blade tip leakage at the trailing edge, allowing the air to lose its thermal energy.

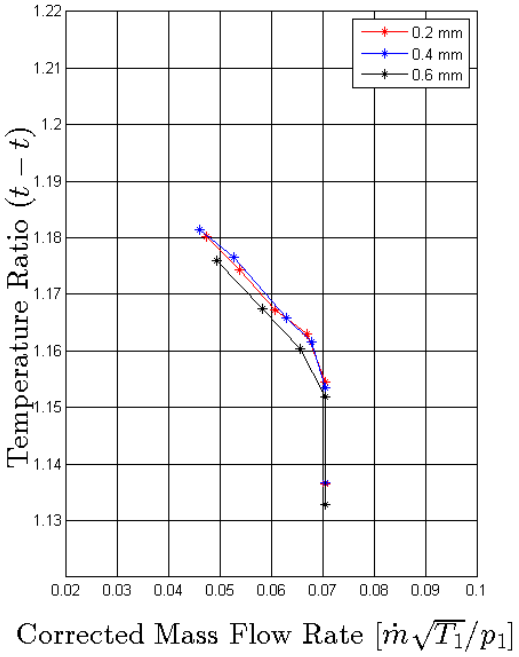

Figure 6.11: Impeller with Vaneless diffuser Total-to-Total Temperature Ratio for 0.2 mm, 0.4 mm and 0.6 mm blade tip clearances

6.2.2 Numerical Results

A step within the diffuser geometry exists in the experimental setup as mentioned in the above section. The step is found at the impeller-inlet diffuser-outlet intersection. The step was reconstructed within the numerical flow domain as shown in Figure 6.12.

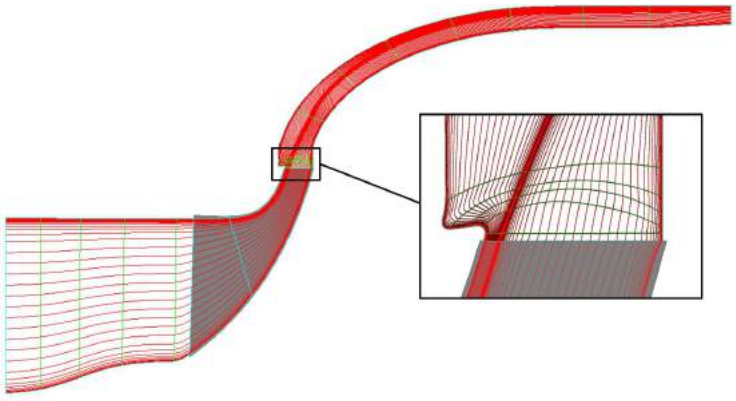

Figure 6.12: Modified Numerical Channel Geometry

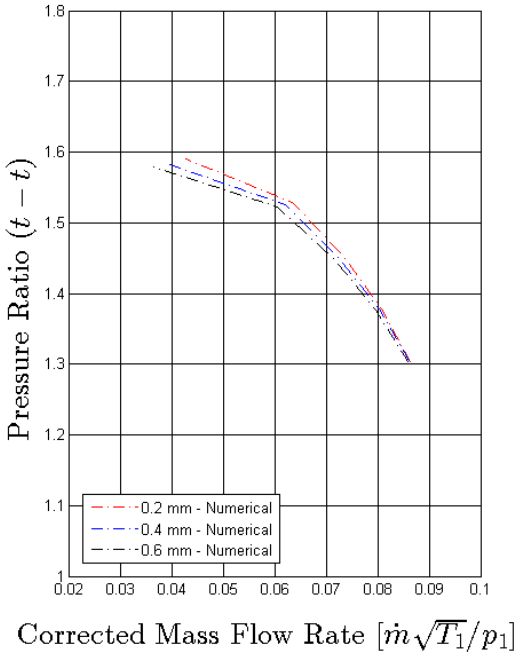

(a)

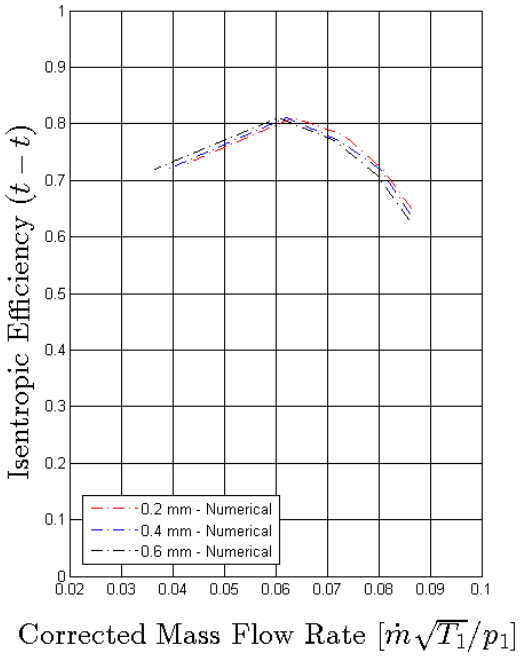

(b)

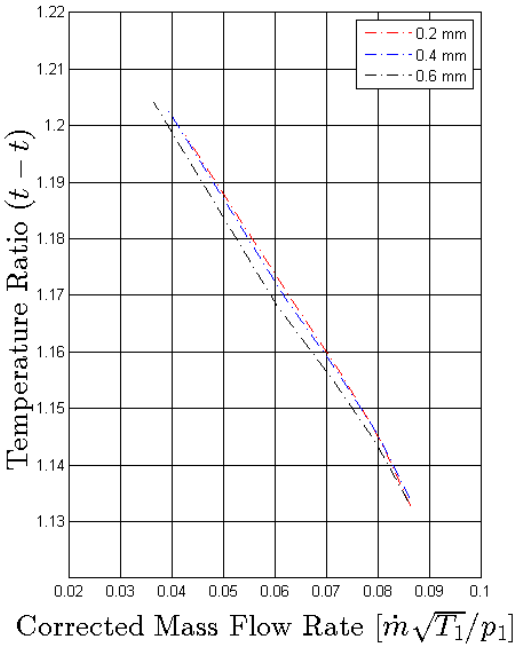

(c)

Figure 6.13: Impeller with Vaneless diffuser a)Total-to-Total Pressure Ratio, b) Total-to-Total Isentropic Efficiency and c) Total-to-Total Temperature Ratio for blade tip clearances of 0.2 mm, 0.4 mm and 0.6 mm

Figures 6.13a, 6.13b and 6.13c above represent the numerical results of the total-to-total pressure ratio (PR_{t-t}), isentropic efficiency (η_{t-t}) and total-to-total temperature ratio (TR_{t-t}) with the step within the diffuser geometry included for the respective blade tip clearances. Even though the step is included, the numerical results predict a wider operating range than what is seen from the experimental results above. By comparing the numerical results with the experimental results, the same behaviour that the effect the blade tip clearance has on impeller performance is witnessed, namely the close grouping of the results.

It is seen from the numerical graphs that the choke margin decreases incrementally as the blade tip clearance increases. This decrease in choke margin is due to the increase in blade tip leakage which leaves less room for the flow within the blade channels and heads to earlier choking of the flow.

Quantifying the numerical results, a performance decrease of 0.18% is found when increasing the blade tip clearance from 0.2 mm to 0.4 mm, with a further decrease of 0.24% when increasing the tip clearance to 0.6 mm. Therefore it can be concluded that the effect of blade tip clearance on impeller performance is negligible due to the step within the diffuser. The step creates a recirculation bubble where energy is expended and thus negates the effect of the smaller trailing edge blade tip clearance on the impeller's performance.

6.2.3 Comparison between Experimental and Numerical Results

Figures 6.14a, 6.14b and 6.14c compare the experimental with the numerical results at the diffuser outlet. From the Figures it is seen that the experimental results coincide well with the numerical results with only the experimental choke margin deviating from the numerical choke margin. Furthermore the numerical results predict a greater effect caused by blade tip clearance on impeller performance than what was experimentally captured. This discrepancy might be related to the heat soak methodology followed for the compressor test bench. By conducting tests successively after one another, the test bench does not have enough time to dissipate the remaining heat in the components from the previous test. Therefore the remaining heat in the system is added to the fluid through the surrounding components, thereby influencing the results.

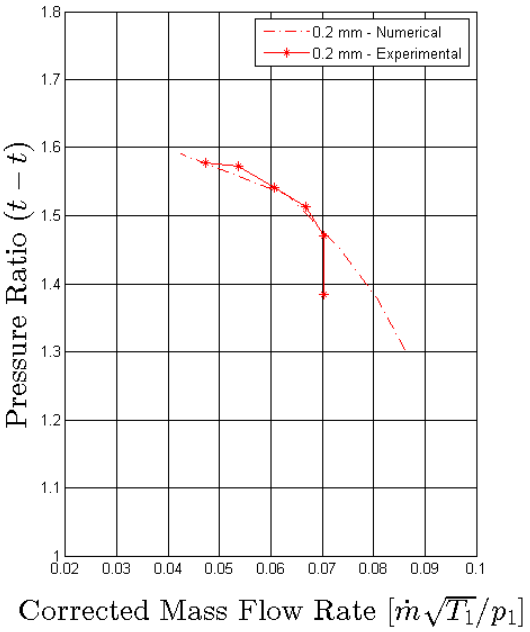

(a) 0.2 mm

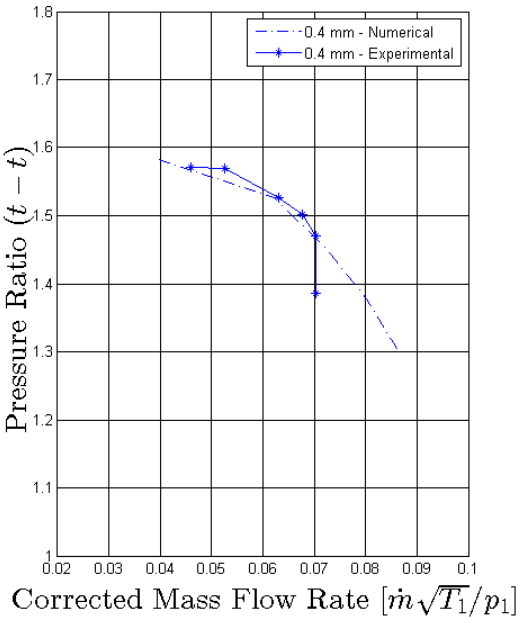

(b) 0.4 mm

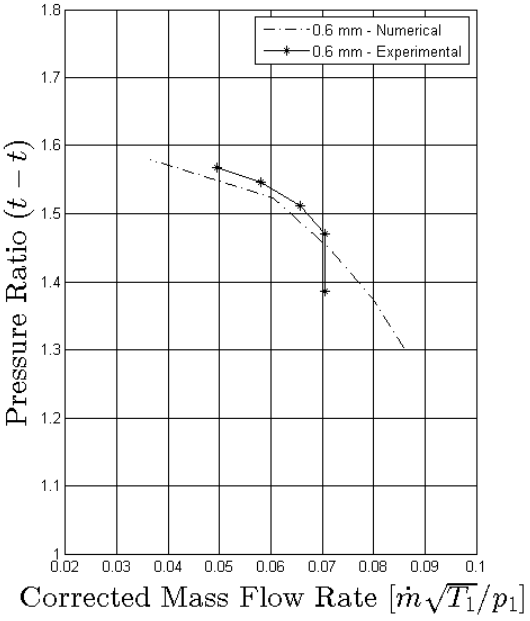

(c) 0.6 mm

Figure 6.14: Compressor Total-to-Total Pressure Ratio at the Vaneless diffuser outlet with Blade Tip Clearance of: a) 0.2 mm, b) 0.4 mm and c) 0.6 mm

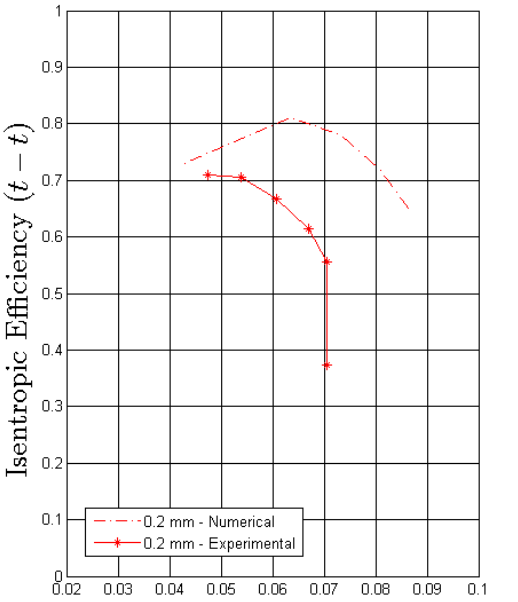

(a) 0.2 mm

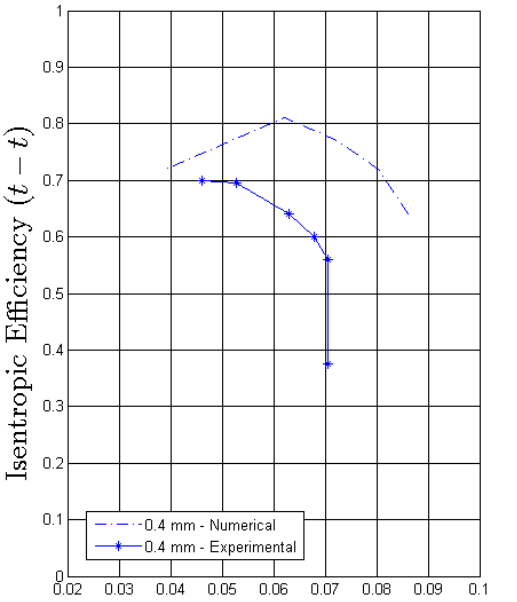

(b) 0.4 mm

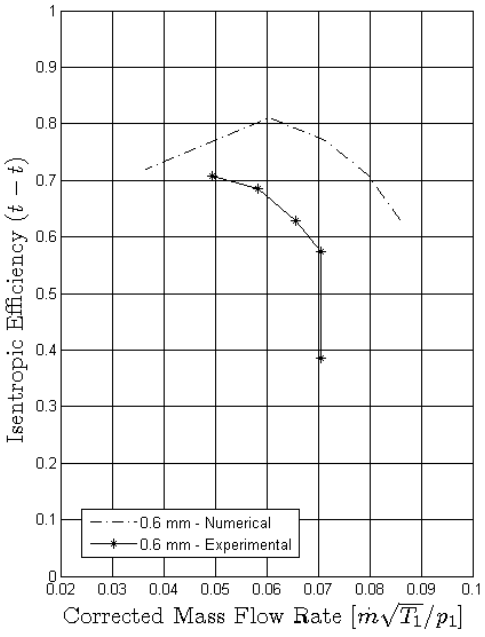

(c) 0.6 mm

Figure 6.15: Compressor Total-to-Total Isentropic Efficiencies at the Vaneless diffuser outlet with Blade Tip Clearance of: a) 0.2 mm, b) 0.4 mm and c) 0.6 mm

The experimental and numerical total-to-total efficiencies are given in Figures 6.15a, 6.15b and 6.15c above. As with the cross-over diffuser, it is seen that there is a larger offset between the experimental and numerical total-to-total efficiency results compared to the pressure ratio results. This offset decreases due to the blade tip clearance having a negligible effect on the impeller's performance experimentally. Thus the experimental curve remains stationary while the numerical curve is affected by the blade tip clearance. Although experimentally the effect of the blade tip clearance on the impeller's performance remains negligible, the trend of the curves follows that of the numerical results.

A comparison between the experimental and numerical total-to-total temperature ratios are represented in Figures 6.16a, 6.16b and 6.17 below. From observation it is seen that all three experimental curves agree with numerical results at a corrected mass flow rate of 0.066 and then deviate from the numerical results as the mass flow rate decreases. Increasing the corrected mass flow rate beyond that of 0.066, the agreement between the experimental and numerical results are interrupted by the early onset of choke. It is interesting to note that the deviation from the numerical results at lower mass flow rates decreases as the tip clearance is increased, which could also be attributed to the remaining thermal energy in the system affecting the experimental results.

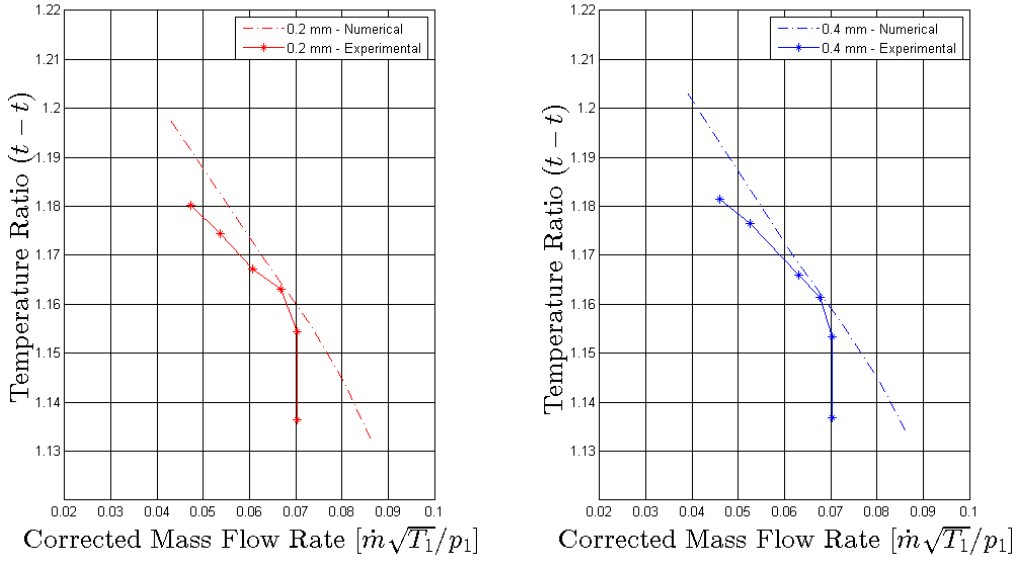

(a) 0.2 mm (b) 0.4 mm

Figure 6.16: Compressor Total-to-Total Temperature Ratio at the Vaneless diffuser outlet with Blade Tip Clearance of: a) 0.2 mm, b) 0.4 mm and c) 0.6 mm

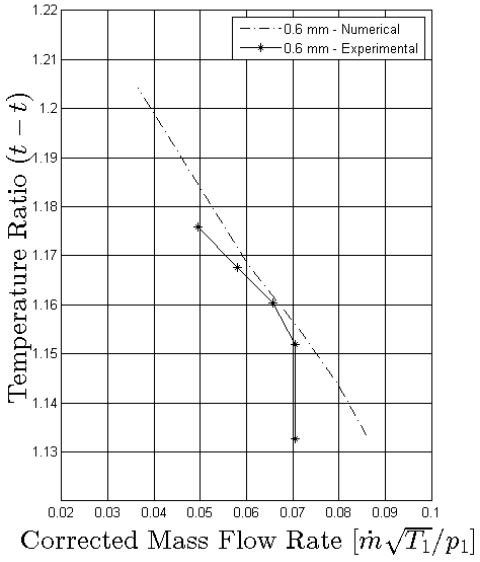

Figure 6.17: Compressor Total-to-Total Temperature Ratio at the Vaneless diffuser outlet with Blade Tip Clearance of 0.6 mm

The results obtained from the experimental setup agree reasonably well with the numerical results after the step within the vaneless diffuser geometry was included. The design point pressure ratio (PR_{t-t}) obtained experimentally is found to be 1.57 corresponding to an isentropic efficiency η_{t-t} of 71% at a mass flow rate ($\dot{m}$) of 0.26 kg/s. Table 6.2 below summarises the experimental results obtained from the compressor test bench.

Table 6.2: Summary of Impeller with Vaneless diffuser Performance (BEP)

Blade Tip Clearance	PR_{t-t}	η_{t-t}	$\dot{m}_{design}[kg/s]$	Operating range
0.2 mm	1.57	71.0%	0.26	32.8%
0.4 mm	1.57	70.0%	0.25	34.6%
0.6 mm	1.56	70.1%	0.27	29.9%

Observing the experimental results for the cross-over and vaneless diffuser it is seen that the choke margin for both diffusers are the same. This was further investigated and realised that the mass flow rate through the compressor test bench is limited by the cross-sectional area of the outlet control valve when fully open. The cross-sectional areas of the diffuser and volute outlets as well as the pressure measurement station are all larger than that of the valve. It is therefore a possible explanation for the deviation of the experimental choke margin from that of the numerical value for the vaneless diffuser.

The experiments were conducted successfully and showed a reasonable correlation with the numerical results for both diffuser types. Both diffusers performed optimally when the blade tip clearance was set at 0.2 mm, which validates Diener's numerical predictions. At 50 000 rpm the vaneless diffuser delivered a total-to-total pressure ratio of 1.57 with an efficiency of 71.0% and mass flow rate of 0.26 kg/s. The cross-over diffuser delivered a total-to-total pressure ratio of 1.63 with an efficiency of 76.3% and mass flow rate of 0.3 kg/s. Thus the cross-over diffuser is able to convert more kinetic energy into pressure energy than the vaneless diffuser, which is consistent with literature (Dixon, 2005).

Chapter 7

Conclusion and Recommendations

7.1 Conclusion

A mixed flow compressor impeller and cross-over diffuser was designed and manufactured by Diener (2016) and Kock (2016) respectively. The project set out to successfully test these MGT components using the blow down facility at Stellenbosch University. A compressor test bench designed by Struwig (2014) was utilised with in-house components designed and manufactured by Thomas (2016) surrounding the compressor and diffusers. The bearing housing manufactured by Thomas was designed to accommodate different impellers and diffusers. As the assembly and testing of the components progressed, certain components were modified or redesigned to enable the successful operation of the test bench. Some of the major components which were modified were the bearing housing and turbine shaft. The turbine shaft was modified to allow the compressor side bearings to press against a shoulder which allowed the shaft to be axially constrained. The size of the turbine and air receiver capacity limited the operational speed of the test bench to 50 000 rpm. The numerical model was recreated independently and validated with the numerical results obtained from Kock at an operational speed of 95 000 rpm. The vaneless diffuser designed by Thomas was also numerically analysed at 95 000 rpm. The numerical model was also analysed at 50 000 rpm for both the cross-over diffuser and vaneless diffuser. Different tip clearances were also analysed numerically and tested experimentally. The tip clearances for both diffusers were increased from 0.2 mm to 0.6 mm with an incremental increase of 0.2 mm.

Experimentally, blade tip clearance had a notable effect on the performance of the cross-over diffuser whereas with the vaneless diffuser the results remained the same regardless of the trailing edge blade tip clearance. After further investigation into the discrepancy in the vaneless diffuser results, a step within the geometry of the vaneless diffuser was found. This was then numerically recreated and analysed and compared with the experimental results. The ex-

perimental results correlated reasonably well with the numerical results for both diffuser types, with small deviations from the numerical values as the tip clearance was increased. The experimental efficiencies however indicated a greater deviation from the numerical predictions. This indicates that more thermal energy is lost in the system than predicted by the numerical solution. Both diffuser types performed optimally with a blade tip clearance of 0.2 mm with the cross-over diffuser delivering the highest total-to-total pressure ratio (PR_{t-t}) of 1.63 and isentropic efficiency (η_{t-t}) of 76.3% at a mass flow rate of 0.3 kg/s. This confirms the importance of the blade tip clearance at the trailing edge of the impeller and to avoid excessive high pressure blade tip leakages.

The modifications to the compressor test bench proved to be successful as all the test were conducted successfully with no damage to the compressor test bench. The impeller however did suffer slight damage on the blade tips at the leading edges as the combination of centrifugal force and thermal loading caused the blades to interfere with impeller shroud. The damage was considered negligible and easily repaired. A trailing edge blade tip clearance of 0.2 mm was achieved due to the test bench modifications and use of the copper strands mentioned in Chapter 5. Thus very small blade tip clearances are achievable practically in experimental set-ups. Concentricity of the shrouds were also achieved by means of the copper strands.

7.2 Recommendations on Improving the Compressor Test Bench

7.2.1 Lubrication

The following improvements to the bearing housing may allow easier control and better operation of the lubrication feed to the bearings:

- Pressure, temperature and flow rate sensors should be included on the lubrication inlet and outlet of the bearing housing. This will also help prevent unnecessary strain on the bearings and leakage to the compressor section.
- The lubricant pathways within the bearing housing should be designed with an increased diameter as it approaches the outlet. This is to prevent pressure build up of the lubricant.
- The bearing housing should include an oil sump at the bottom before the outlet to act as safety buffer against pressure build up.

- Alternatively a pressurised oil feed to the bearing housing could be used which bypasses the bearings completely. The pressurised oil feed then has small oil injectors which stems off from the main pressurised feed and is aimed at the bearings. This way small amounts of oil are continually sprayed on the bearing while the majority of the oil completes the lubricant circulation loop. This will then reduce the strain on the bearings.

To find the best possible solution the approach could be to use rapid prototyping techniques like 3-D printing. The main focus for improving the lubrication method is to reduce the strain on the bearings during operation and to prevent excess lubricant leakage into the compressor section.

7.2.2 Compressor Test Bench Setup

The following improvements to the compressor test bench setup will enable more precise assembly of compressor parts:

- The diffuser (5.2b) should be designed with an extra annular surface on the shroud flange, slightly smaller than the outside diameter of the shroud flange, which fits into the scroll assembly to ensure concentricity of the diffuser shroud. This will enable the impeller shroud to be assembled concentric around the impeller.
- A thicker O-ring should be used to seal the diffuser back plate.
- Thicker fastening plates should be used to secure the diffuser back plate to the shroud as the current plate deforms when fastened.
- The addition of an extra split ring at the rear of the turbine shaft would further reduce oil leakage at the turbine outlet.
- When flanges are wielded to piping, the holes made for the bolts should be positioned far enough from the welds in order to prevent interference with the bolts to be fastened.
- Thread should be added to the annular surface of the impeller shroud and to the inside of the annular surface of the diffuser shroud (which is flush to the impeller shroud). This will allow easy adjustment of the tip clearance, which will prevent the need to apply modifications to the design when the specified tip clearance is not achieved.
- The bearing housing should be designed with enough room to add circlips to secure the bearing outer races.

- Care should be taken where the lubricant inlet and outlet is located to ensure that all the bolts of the turbine volute can be secured to prevent compressed air leakage.
- The optical switch should be cooled as the voltage intensity would deteriorate as the temperature increases. Alternatively, the switch should not be fastened to the compressor shroud but kept in position by other means.
- A specially designed optical switch holder would prove beneficial to allow faster and precise placing of the switch after assembling the test bench or adjustment of testing equipment.
- Heat sinks could be added to eliminate heat build up in the system. This is to prevent addition of heat to the fluid and temperature probes when operating at a lower mass flow rate. This will ensure that the temperature probe only measures the fluid temperature and not that of the surroundings.

Appendices

Appendix A

Compressor Assembly Procedure

A.1 Assembly Procedure

The compressor is assembled following the guidelines laid out by Thomas (2016). The parts that make up the assembly are laid out in order of assembly from Figure A.1-A.20. (All Figures are from Thomas (2016)).

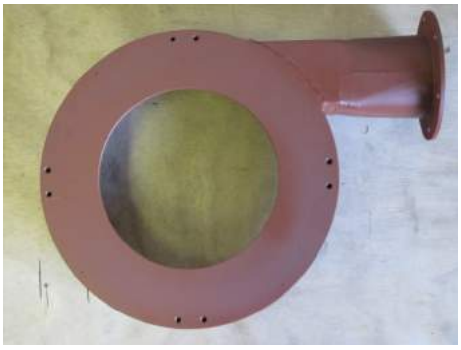

Figure A.1: Volute

Figure A.1 is the custom housing for the compressor which will be referred to as the volute. The volute forms part of the exhaust flow path of the compressor section. The diffuser housing, shown in Figure A.2, is attached to the volute and houses the diffuser.

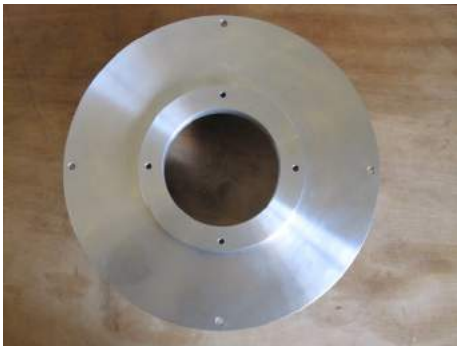

Figure A.2: Diffuser Housing

Figure A.3 shows the diffuser housing attached to the volute with the Festo pressure fittings added. The impeller housing is then bolted to the volute-diffuser assembly. Figure A.4 shows the impeller housing that houses the impeller.

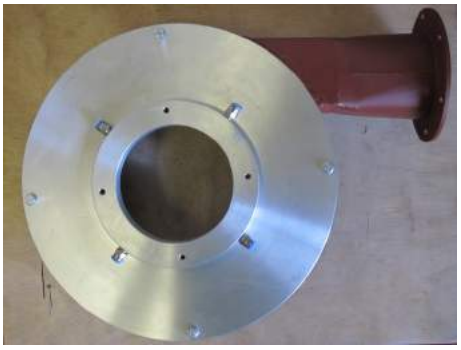

Figure A.3: Diffuser shroud and Volute Assembly

Figure A.4: Impeller Shroud

The above mentioned parts shown in Figures A.1-A.4 form part of the volute-housing assembly. Next the parts that are part of the Bearing Housing assembly are displayed. Figure A.5 displays the bearing housing for the turbine side. Both bearings for the turbine and compressor side use continuous oil lubrication. The turbine bearing housing uses one GRW D6903 15^o bearing which is displayed in Figure A.6 below. The turbine bearing housing is then sealed off using the turbine oil seal displayed in Figure A.7, with a 55 mm inside diameter (ID) O-ring shown in Figure A.8.

Figure A.5: Turbine Bearing Housing

Figure A.6: GRW D6903 15^o

(a)

(b)

Figure A.7: Modifications: a) Outside and b) inside of Turbine Oil Seal

Figure A.8: O-ring ID 55x2 mm

Two *Xtreme 012 7002-15º UL/CSB P4* bearings (Figure A.6) are used to secure the shaft in the compressor bearing housing shown in Figure A.9.

Figure A.9: Compressor Bearing Housing

The parts that make up the diffuser assembly are discussed next. Figure A.10 shows the rear diffuser adapter plate with Festo pressure fittings. The pressure fittings connects the pressure transducers via tubing with the compressor outlet to take air pressure measurements.

Figure A.10: Rear Diffuser Adapter Plate with Festo pressure fittings

A 160 mm ID O-ring (Figure A.11) is inserted on the back of the Diffuser adapter plate.

Figure A.11: O-ring ID 160x2 mm

The diffuser (Figure A.12b) and the spacer (Figure A.12b) are assembled with the rear diffuser adapter plate (Figure A.10) to form the diffuser assembly as shown in Figure A.13.

(a) (b)

Figure A.12: a) Diffuser and b) Spacer

Figure A.13: Diffuser Assembly

The diffuser assembly (Figure A.14a) and the bearing housing assembly (Figure A.14b) are assembled together to form the diffuser and bearing housing assembly.

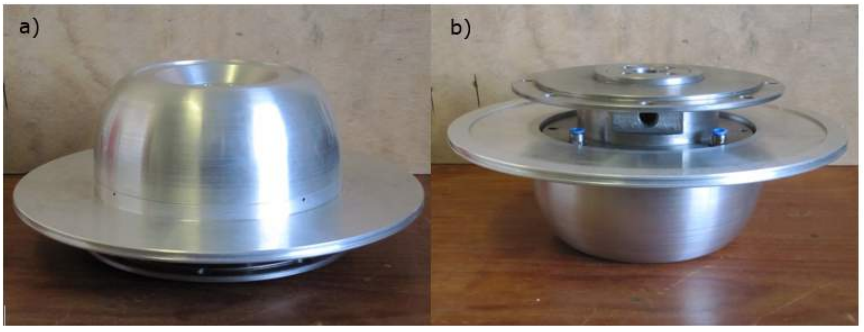

Figure A.14: Diffuser and Bearing housing Assembly

The rotating assembly comprises of a turbine spacer (Figure A.15a), the Schwitzer turbine shaft (Figure A.15b) and a Airsearch heat sink (Figure A.15c). Assembling these parts along with the diffuser and bearing house assemblies forms

the Shaft assembly as shown in Figure A.16. The Schwitzer turbine is right hand rotation, e.i. rotates anti-clockwise when looking down the shaft from the compressor side. Dimensions of the Schwitzer shaft are shown in Section A.2.

Figure A.15: Turbine spacer (a), Airsearch Turbine shaft (b) and Heat sink (c)

Figure A.16: Complete Shaft Assembly

The impeller (Figure A.17a) is fastened to the shaft assembly to form the rotating assembly (Figure A.17b).

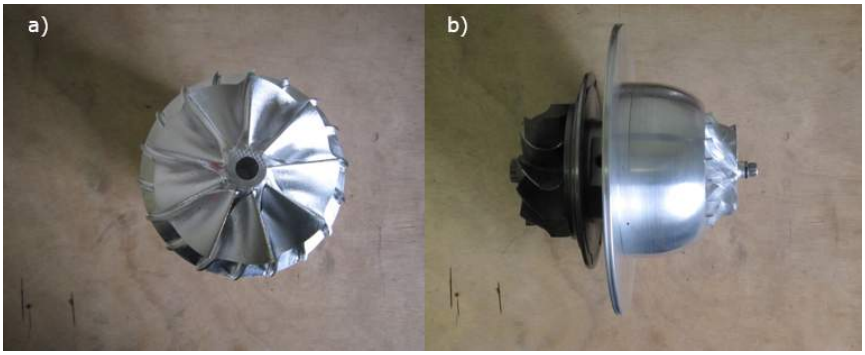

Figure A.17: Impeller and Rotating Assembly Respectively

The rotating assembly is inserted into the scroll diffuser housing assembly (Figure A.3) to form the scroll rotating assembly, as shown in Figure A.18 below.

Figure A.18: Scroll Rotating Assembly

Figure A.19: Airsearch Turbine casing

The Airsearch turbine casing (Figure A.19) is bolted to the scroll rotating assembly (Figure A.18) to form the complete assembly of the compressor test bench as shown in Figure A.20 below.

Figure A.20: Complete Assembly of Compressor

A.2 Shaft Dimensions

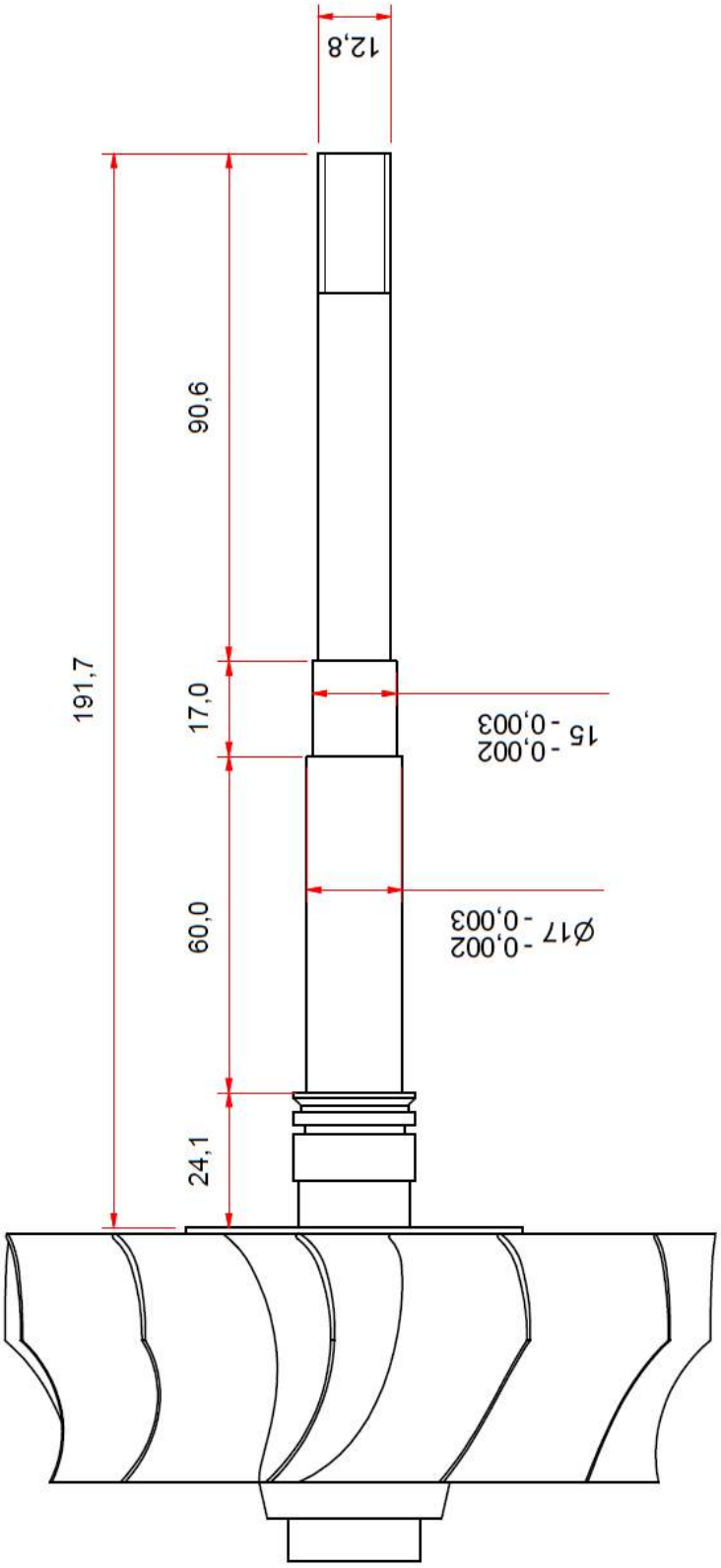

Figure A.21: Schwitzer Shaft Dimensions

Appendix B

LabView Default Polynomial Functions for Thermocouples

B.1 Polynomial Functions

The FPGA chip samples the raw temperature readings from the thermocouples and scales it via the real-time processor. Each thermocouple is individually sampled and the data is sent to the real-time processor. The raw temperature data is measured in micro-volts (μV) and then grouped depending on the type of thermocouple. The voltage readings are then arranged into a single data array and processed by a for loop (Struwig, 2014). The for loop converts the voltage reading of each thermocouple to Kelvin using the standard LabView^{TM} polynomial functions (Eq. B.1.1 - B.1.3).

For J-Type thermocouples between a temperature range of -210^{o}C and 0^{o}C the polynomial equation is:

$$\begin{aligned} T = {} & V((1.9528268 \times 10^{-2}) + V((-1.2286185 \times 10^{-6}) + V((-1.0752178 \times 10^{-9}) \\ & + V((-5.9086933 \times 10^{-13}) + V((-1.7256713 \times 10^{-16}) \\ & + V((-2.8131513 \times 10^{-20}) + V((-2.3963370 \times 10^{-24}) \\ & + V((-8.3823321 \times 10^{-29}))))))))) \end{aligned} \tag{B.1.1}$$

(accurate to a range of -0.05^{o}C to 0.03^{o}C)

For temperatures between 0^{o}C to 760^{o}C:

$$\begin{aligned} T = {} & V((1.978425 \times 10^{-2}) + V((-2.001204 \times 10^{-7}) + V((1.036969 \times 10^{-11}) \\ & + V((-2.549687 \times 10^{-16}) + V((3.585153 \times 10^{-21}) \\ & + V((-5.344285 \times 10^{-26}) + V((5.099890 \times 10^{-31})))))))) \end{aligned} \tag{B.1.2}$$

(accurate to a range of -0.04^{o}C to 0.04^{o}C).

For T-Type thermocouples between a temperature range of 0^{o}C and 400^{o}C the polynomial equation is:

$$\begin{aligned} T = V((2.592800 \times 10^{-2}) + V((-7.602961 \times 10^{-7}) + V((4.637791 \times 10^{-11}) \\ + V((-2.165394 \times 10^{-15}) + V((6.048144 \times 10^{-20}) \\ + V((-7.293422 \times 10^{-25})))))))) \end{aligned} \tag{B.1.3}$$

(accurate to a range of -0.03^{o}C to 0.03^{o}C).

Appendix C

NUMECA Set-up

C.1 Blade Grid point Distribution

The following grid point distribution has been chosen for the impeller's main and splitter blade respectively.

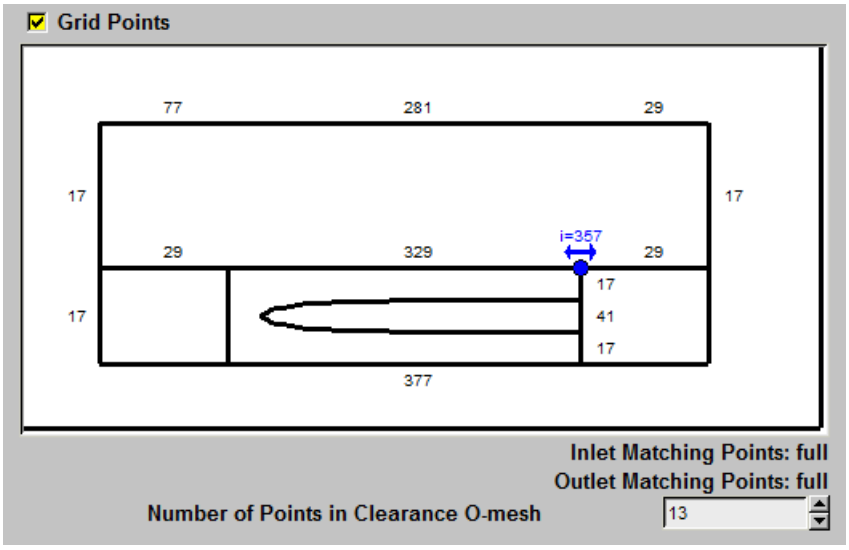

Figure C.1: Impeller Main Blade Grid Distribution

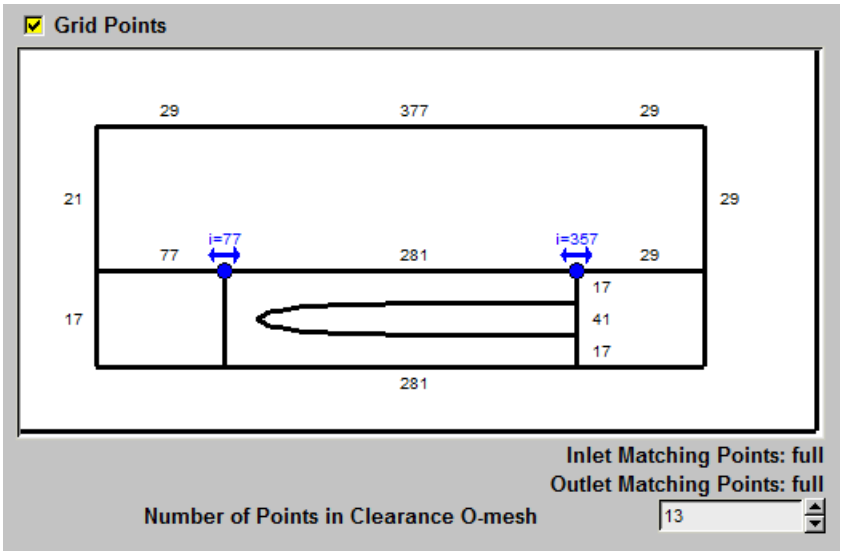

Figure C.2: Impeller Splitter Blade Grid Distribution

The default topology was chosen for the diffuser grid point distribution.

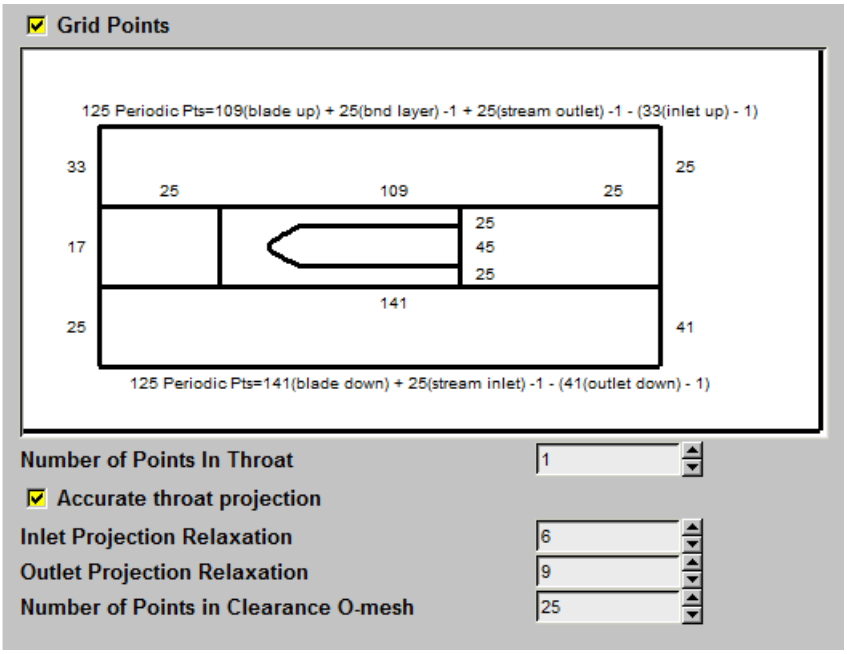

Figure C.3: Diffuser Blade Grid Distribution

C.2 Blade Topology

Figure C.4 below is used as an example for the B2B topology settings.

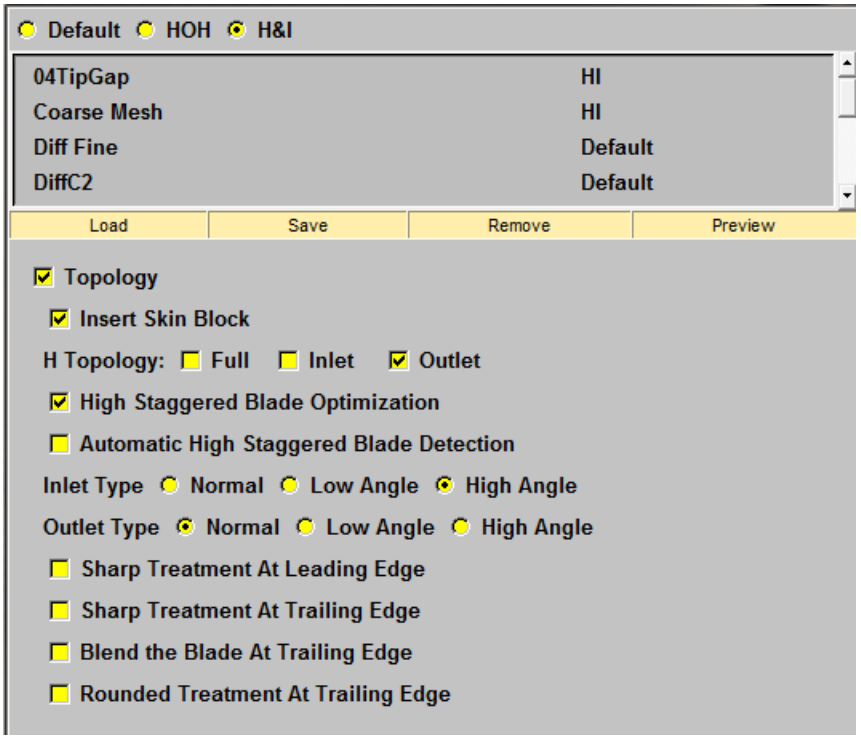

Figure C.4: Impeller Main Blade Topology

C.3 NUMECA FINE Configuration

Configuration of FINE^TM parameters regarding the numerical investigation of the impeller and diffuser performance is shown in Table C.1 below.

Table C.1: Flow Solver Configuration

Configuration	**Fluid Model**			AIR (Perfect)
	Flow Model		Modeling of Turbulence:	Spalart-Allmaras
			Characteristic Length:	0.0555 m
			Characteristic Velocity:	552 m/s
			Mathematical Model:	Turbulent Navier-Stokes
	Rotating Machinery	Rotating Blocks	Rotational Speed: Impeller	95000rpm
			Rotational Speed: Diffuser	0
		Rotor-Stator		Left as is.
Boundary Conditions	***Inlet***		Total Quantities Imposed	Velocity Direction
	Outlet		Pressure Imposed	Avg Static Pressure: 260-425kPa
	Periodic		All has been selected:	Matching
	Solid	Cross-over Diffuser	hub:	Constant Rotational Speed: 0rpm
			shroud:	
			Blades	
		Impeller	hub:	Area Defined: Speed 1 = 0Speed 2 = 95000. Lower Radius Limit = 0, Higher Radius Limit = 0.0555, Lower/Higher axial limit = -0.04/0.04
			shroud:	Constant Rotational Speed: 0rpm
			Blades	Constant Rotational Speed: 95000rpm
Numerical Model	***CFL Number***			3
	Current grid level			1 1 1
	Number of Grid Levels			2
	Coarse Grid initialization			Yes
Initial Solution	***Blocks and Groups***	For turbomachinery	Inlet: Estimated Static Pressure	90000 Pa
			Outlet: Estimated Static Pressure	100000 Pa
Outputs	***Computed Variables***	Thermodynamics	Temperature	All Selected
			Pressure	All Selected
			Properties	Only Density Selected
			Pressure Coefficients	None selected
		Velocities	Absolute Velocities	Vxyz & Mach number selected
			Relative Velocities	Wxyz & Mach number selected
		Solid Data		Static Pressure
				Cf
				y+
				staticTemperature
		Turbulence		Wall Distance
				Turbulent Viscosity
				y+ (3D Field)
	Azimuthal Average Variables	Same as Computed Variables		
	ANSYS	Leave as is		
Computational Steering	***Control Variables***	Iterations	Maximum no. of iter:	4000
			Convergence Criteria	-8
		Output Files	Save Solution every	200 iterations
		Solver Precision		Single

Appendix D

Compressor Test Bench Calibration

This section discusses the calibration of the pressure transducers and thermocouples.

D.1 Pressure Transducer Calibration

The pressure transducers were recalibrated on the cRIO-9073 data acquisition system with the NI-9207 C-Series Analogue Input modules using an air pump and a 1000 kPa WIKA absolute pressure gauge as reference for the measured pressure. The differential pressure transducer at the bellmouth was calibrated using a Betz micro-manometer. Table D.1 contains the Pressure Calibration curve equations.

Table D.1: Pressure Calibration Curve Equations

Transducer	Index	Equation	R^2
Bellmouth	dp	$y = 0.9985x + 0.0027$	1
Compressor inlet	1	$y = 0.9804x + 2.6191$	1
Impeller outlet	2	$y = 0.9974x + 0.1308$	1
Diffuser outlet	3	$y = 1.0069x - 2.4834$	1
Volute outlet	4	$y = 1.002x + 1.074$	1
Orifice inlet	5	$y = 0.997x - 7.5739$	1
Orifice outlet	6	$y = 0.9966x + 1.436$	1
Turbine inlet	7	$y = 1.005x + 3.3124$	0.997
Turbine outlet	8	$y = 0.9976x + 2.1754$	1

D.2 Thermocouple Calibration

Table D.2 presents the thermocouple calibration curve equations found at each measurement station.

Table D.2: Thermocouple Calibration Curve Equations

Thermocouple	Index	Equation	R^2
Bellmouth	1	$y = 1.0076x + 0.1474$	0.99
Volute outlet	4	$y = 1.006x + 0.4723$	0.99
Orifice	5	$y = 0.8818x + 36.62$	0.99
Turbine inlet 1,2	7	$y = 1.001x - 14.433$	0.99
Turbine inlet 3	7	$y = 0.8307x + 47.73$	0.99
Turbine outlet	8	$y = 1.0116x - 9.255$	0.99

Appendix E

Tachometer Design and Coding

E.1 Arduino Design and Construction

The components consist of an Arduino Uno Micro programmable board, 16 bit Liquid Crystal Display, colour coded connecting wires and the OPTEK technology OPB732 Long Distance infra-red Reflective Switch. The number 3 pin (Orange wire) on the Arduino board is an interrupt pin and capable of taking high frequency digital signal which is converted from Hz to RPM. The completed design can be seen in figures E.1 and E.2 below. The Arduino has a built in function which allows it to determine whether the incoming signal is rising or falling.

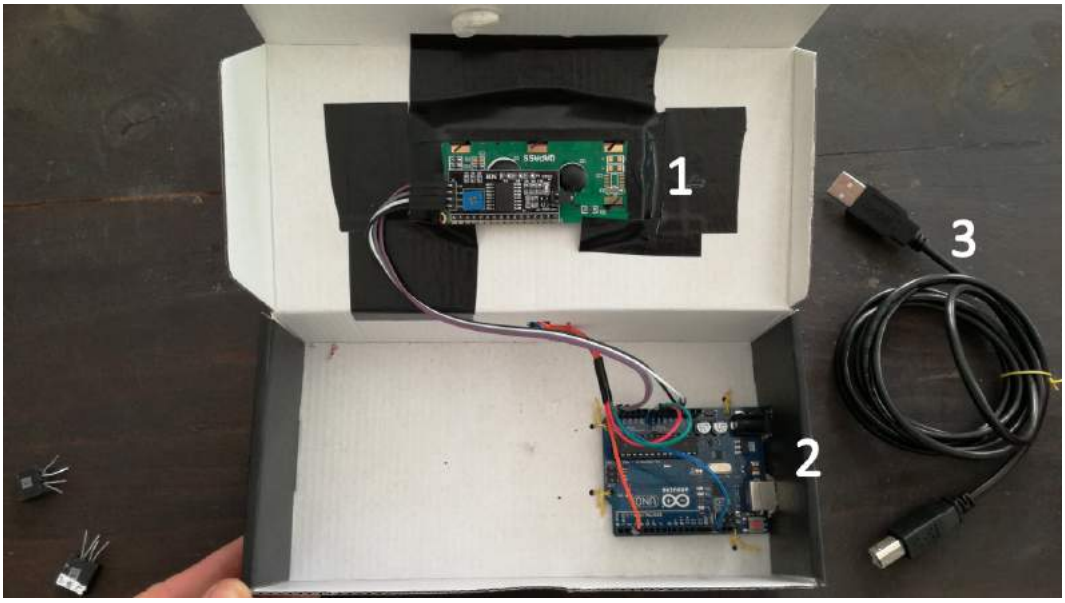

Figure E.1: Tachometer Hardware: 1. LCD screen, 2. Arduino Uno, 3. Power cable

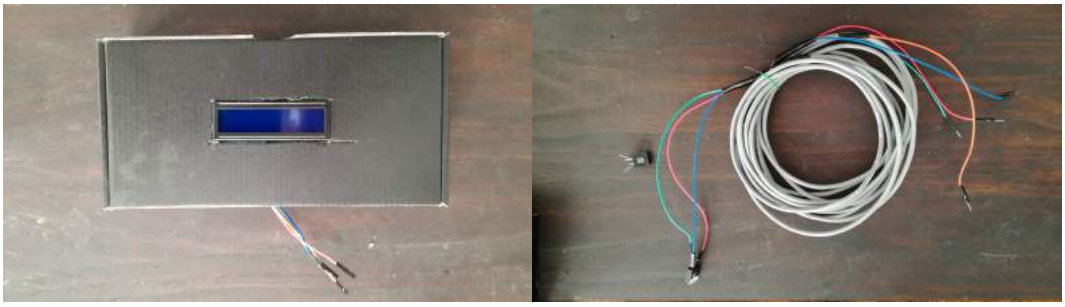

(a) (b)

Figure E.2: a) LCD screen, finished product b) Wiring to Optical Switch

The Arduino tachometer functioned correctly until 14 kRPM was reached. The signal strength diminished as the rotating frequency increased, to a point where the Arduino could no longer interpret the rising signal correctly. It is therefore recommended not to use the Arduino power supply (5V) for the optical switch but rather have an individual power supply powering the optical switch. The resistance should also be increased on the optical switch wiring to increase the breakdown voltage on the switch which will allow a clearer signal. An oscilloscope was used to ensure that the Arduino had the correct interpretation of the signal. The set-up of the oscilloscope is shown below in figure E.3 a) and b) respectively.

(a) (b)

Figure E.3: a) Oscilloscope, b) Oscilloscope Measuring wires

E.2 Arduino Uno Code

The following Arduino code adapted from arduinoprojects101 (2018) has been used to program the Tachometer.

```
#include <ShiftLCD.h>
#include <Wire.h>
#include <LCD.h>
#include <LiquidCrystal_I2C.h>



#define I2C_ADDR    0x3F // <<----- Add your address here.  Find it from I2C Scanner
#define BACKLIGHT_PIN     3
#define En_pin  2
#define Rw_pin  1
#define Rs_pin  0
#define D4_pin  4
#define D5_pin  5
#define D6_pin  6
#define D7_pin  7

LiquidCrystal_I2C  lcd(I2C_ADDR, En_pin, Rw_pin, Rs_pin, D4_pin, D5_pin, D6_pin, D7_pin);

volatile byte rpmcount;
unsigned int rpm;
unsigned long timeold;

void rpm_fun()
 {
      rpmcount++;
 }



void setup()
 {
   lcd.begin(16, 2);  // intialise the LCD
   lcd.setBacklightPin(BACKLIGHT_PIN, POSITIVE);
   lcd.setBacklight(HIGH);
   lcd.home (); // go home

   //Interrupt 0 is digital pin 2, so that is where the IR detector is connected
   //Triggers on FALLING (change from HIGH to LOW)
   attachInterrupt(2, rpm_fun, FALLING);

   rpmcount = 0;
   rpm = 0;
   timeold = 0;
 }
```

```
void loop()
{
  //Update RPM every second
  delay(1000);
  //Don't process interrupts during calculations
  detachInterrupt(0);
  //Note that this would be 60*1000/(millis() - timeold)*rpmcount if the interrupt
  //happened once per revolution instead of twice. Other multiples could be used
  //for multi-bladed propellers or fans
  rpm = (30*1000/(millis() - timeold)*rpmcount)*2;
  timeold = millis();
  rpmcount = 0;

  //Print out result to lcd
  lcd.clear();
  lcd.print("RPM =");
  lcd.setCursor(7,0);
  lcd.print(rpm);

  //Restart the interrupt processing
  attachInterrupt(0, rpm_fun, FALLING);
 }
```

Appendix F

Sample Data and Calculations

F.1 Experimental Sample Calculations

This section gives the sample calculation for a single operating point of the impeller with the cross-over diffuser at 50 000 rpm and 0.2 mm blade tip clearance. The corresponding mass flow rate at this operating condition is $\dot{m} = 0.3$ kg/s. All the sample data is found in Section F.2 below. The values used for the sample calculations correspond to the average sample values after the calibration equations in Appendix D were applied to each measurement instrument. The mass flow rate is calculated through the differential pressure measured across the bellmouth.

Table F.1: Constant Properties

Discharge coefficient parameters	L_1, L_2	=	1, 0.47
Molar weight of dry air	M	=	28.96 kg/mol
Reference temperature for air	T_0	=	297 K
Reference viscosity for air	μ_0	=	1.71×10^{-5} $kg/s.m$
Sutherland temperature for air	S	=	110.40 K
Temperature probe dynamic correction factor	K	=	0.96
Viscosity of air at 20^oC	μ_0	=	1.71×10^{-5} $kg/s.m$
Universal gas constant of dry air	R	=	287 $J/kg.K$

Specific heat at constant pressure is calculated as a function of temperature:

$$C_p = (a + bT + cT^2 + dT^3)/M \tag{F.1.1}$$

With constants $a = 28.11$, $b = 0.1967 \times 10^{-2}$, $c = 0.4082 \times 10^{-5}$ and $d = -1.966 \times 10^{-9}$. Dimensions of the pressure measurement station are given

below with Figure F.1 indicating the measurement station:

Pipe length	ΔL_4	=	$0.92\ m$
Pipe valve outlet diameter	d_4	=	$0.088\ m$
Pipe valve outlet cross-sectional area	A_4	=	$6.082 \times 10^{-3}\ m^2$
Pipe internal surface roughness	ϵ_4	=	$0.046 \times 10^{-3}\ m$
Bellmouth outlet diameter	d	=	$0.0773\ m$

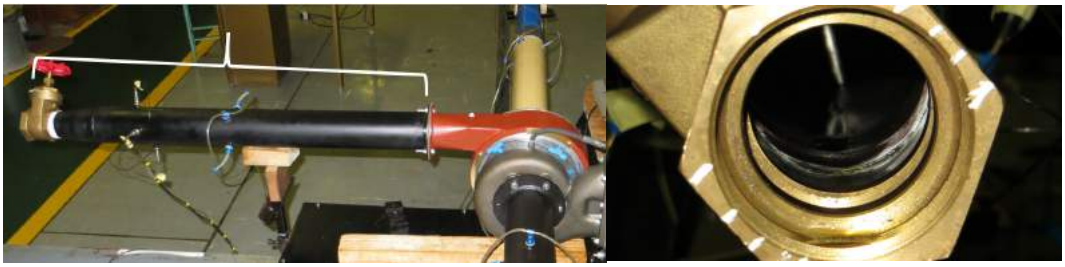

(a) (b)

Figure F.1: a) Pressure measurement station b) Outlet valve

The pipe valve outlet dimensions were used for calculation purposes as the valve had the smallest cross-sectional area and limited the mass flow rate as mentioned in chapter 6. The average quantities from the experimental data after the calibration equations were applied are given below:

Ambient Pressure	P_{amb}	=	$95.217\ kPa$
Ambient temperature	T_{amb}	=	$297.39\ K$
Differential Pressure at Bellmouth	dP	=	$1.8536\ Pa$
Impeller inlet total temperature	T_{t1}	=	$299.8\ K$
Impeller outlet static pressure	P_{s2}	=	$126.78\ kPa$
Diffuser outlet static pressure	P_{s3}	=	$155.04\ kPa$
Volute outlet static pressure	P_{s4}	=	$146.13\ kPa$
Volute outlet probe temperature	T_{s4}	=	$351.98\ K$

Using the sample data above a compressor operating point is calculated. First the ambient air density is calculated from equation F.1.2:

$$\begin{aligned}\rho_{amb} &= \frac{P_{amb}}{RT_{amb}} \\ &= \frac{95.217}{(0.278)(297.39)} \\ &= 1.152 \quad kg/m^3\end{aligned} \tag{F.1.2}$$

Next the bellmouth velocity (V_{bm}) and Reynolds number (Re_{bm}) is calculated.

$$\begin{aligned}V_bm &= [\frac{2dP}{\rho_{amb}(1 - D^4d^4)}]^{0.5} \\ &= [\frac{2(1853.6)}{(1.152)(1)}]^{0.5} \\ &= 56.73 \quad m/s\end{aligned} \tag{F.1.3}$$

The coefficient of discharge is calculted from the bellmouth calibration equations determined by Struwig (2014):

$$\begin{aligned}C_d &= \exp^{\frac{-1500}{Re_{bm}}} \\ &= \exp^{\frac{-1500}{280654.65}} \\ &= 0.99\end{aligned} \tag{F.1.4}$$

The mass flow rate can now be determined:

$$\begin{aligned}\dot{m} &= C_dE\epsilon\frac{\pi}{4}d^2\sqrt{2dP\rho_{amb}} \\ &= (0.99)(1)(1)(\pi/4)(0.0773^2)\sqrt{2(1853.6)(1.152)} \\ &= 0.3036 \quad kg/s\end{aligned} \tag{F.1.4}$$

Where $E = 1$ is the velocity of approach factor and $\epsilon = 1$ is the expandability factor. Next the conditions at the pressure measurement station is calculated and used to determine the total-to-static pressure ratio and total-to-total efficiency at the pressure measurement station and diffuser outlet. The initial static temperature is approximated by the probe temperature at the pressure

measurement station:

$$\begin{aligned} T_{s4} &= T_{p4} \\ &= 351.98 \quad K \end{aligned} \tag{F.1.4}$$

The initial conditions at the pressure measurement station is calculated:

$$\begin{aligned} C_{p,4} &= (a + bT_{s4} + cT_{s4}^2 + dT_{s4}^3)/M \\ &= \frac{(a + b(351.98) + c(351.98)^2 + d(351.98)^3)}{28.96 \times 10^{-3}} \\ &= 1009.05 \quad J/kg.K \end{aligned} \tag{F.1.4}$$

$$\begin{aligned} \gamma_4 &= C_{p,4}/(C_{p,4} - R) \\ &= 1009.05/(1009.05 - 287) \\ &= 1.397 \quad J/kg.K \end{aligned} \tag{F.1.4}$$

$$\begin{aligned} \rho_4 &= P_{s4}/(RT_{s4}) \\ &= 146.13/((0.287)(351.96)) \\ &= 1.447 \quad kg/m^3 \end{aligned} \tag{F.1.4}$$

The absolute gas velocity and Mach number can be determined:

$$\begin{aligned} c_4 &= \dot{m}/(\rho_4 A_4) \\ &= 0.3036/((1.447)(6.082 \times 10^{-3})) \\ &= 34.51 \quad m/s \end{aligned} \tag{F.1.4}$$

$$\begin{aligned} Ma_4 &= c_4/\sqrt{\gamma_4 T_{s4} R} \\ &= 34.51/\sqrt{(1.39)(351.96)(287)} \\ &= 0.0921 \end{aligned} \tag{F.1.4}$$

The total temperature at the pressure measurement station is determined:

$$\begin{aligned} T_{t4} &= T_{s4} + \frac{(1 - K)c_4^2}{2C_{p,4}} \\ &= 351.96 + \frac{(1 - 0.96)(34.51^2)}{2(1009.05)} \\ &= 351.98 \quad K \end{aligned} \tag{F.1.4}$$

The new static temperature is calculated:

$$\begin{aligned} T_{s4,new} &= \frac{T_{t4}}{1+\frac{(\gamma_4-1)Ma_4^2}{2}} \\ &= \frac{351.98}{1+\frac{(1.39-1)0.0921^2}{2}} \\ &= 351.39 \quad K \end{aligned} \tag{F.1.4}$$

The new static temperature (eq F.1.4) is compared with the initial static temperature (eq F.1.4). While the difference between the old and new static temperature remains greater than 1.6×10^{-6} K the new static temperature will be substituted back into equation F.1.4 and reiterated.

$$\begin{aligned} \Delta T_{s4} &= |T_{s4} - T_{s4,new}| \\ &= |351.96 - 351.39| \\ &= 0.57K >> 1 \times 10^{-6} \quad K \end{aligned} \tag{F.1.4}$$

The total pressure is calculated next:

$$\begin{aligned} P_{t4} &= P_{s4}[1+\frac{(\gamma_4-1)Ma_4^2}{2}]^{\frac{\gamma_4}{\gamma_4-1}} \\ &= 146130[1+\frac{(1.39-1)0.0921^2}{2}]^{\frac{1.39}{1.39-1}} \\ &= 146.993 \quad kPa \end{aligned} \tag{F.1.4}$$

Thus the new static and total conditions were calculated as follow:

$$\begin{aligned} T_{s4} &= 351.39 \quad K \\ C_{p4s} &= 1009.05 \quad J/kg.K \\ \gamma_4 &= 1.39 \\ \rho_{4s} &= 1.447 \quad kg/m^3 \\ c_4 &= 34.51 \quad m/s \\ Ma_4 &= 0.921 \\ T_{t4} &= 351.98 \quad K \\ P_{t4} &= 146.993 \quad kPa \end{aligned} \tag{F.1.4}$$

Once all the quantities are known for the pressure measurement station, the total conditions at the volute outlet can be determined by using compressible pipe flow theory with friction. The following equation is used to determine the Mach number at the volute outlet:

$$\frac{\bar{f}L^*}{d} = \frac{1 - Ma_4^2}{\gamma_4 Ma_4^2} + \frac{\gamma_4 + 1}{2\gamma_4} \ln \frac{(\gamma + 1)Ma_4^2}{2 + (\gamma - 1)Ma_4^2} \tag{F.1.4}$$

$$\frac{\bar{f}\Delta L}{d} = (\frac{\bar{f}L^*}{d})_{vo} - (\frac{\bar{f}L^*}{d})_{pm} \tag{F.1.4}$$

The right hand side of equation F.1.4 is calculated with known conditions Ma_4 and γ_4 at the pressure measurement station:

$$\begin{aligned}(\frac{\bar{f}L^*}{d})_{pm} &= \frac{1 - 0.0921^2}{1.39(0.0921)^2} + \frac{1.39 + 1}{2(1.39)} \ln \frac{(1.39 + 1)(0.0921)^2}{2 + (1.39 - 1)(0.0921)^2} \\ &= 80.145\end{aligned} \tag{F.1.4}$$

The fluid viscosity is determined next:

$$\begin{aligned}\mu_4 &= \mu_0(\frac{T_{s4}}{T_0})^{3/2}(\frac{T_0 + S}{T_{s4} + S}) \\ &= 1.71 \times 10^{-5}(\frac{351.39}{299.8})^{3/2}(\frac{299.8 + 110.4}{351.39 + 110.4}) \\ &= 1.896 \times 10^{-5} \quad kg/m.s\end{aligned} \tag{F.1.4}$$

The friction factor on the left hand side of equation F.1.4 is iteratively calculated as it is dependent on the average fluid velocity (Struwig, 2014). The absolute velocity at the pressure measurement station is used as the average fluid velocity at the volute outlet. The Reynolds number for the volute outlet is now calculated:

$$\begin{aligned}Re_{d4} &= \frac{\rho_4 \bar{c}_4 d_4}{\mu_4} \\ &= \frac{(1.447)(34.51)(0.088)}{1.896 \times 10^{-5}} \\ &= 231770.32\end{aligned} \tag{F.1.4}$$

The friction factor is calculated by using an explicit formula given by Halaand:

$$\begin{aligned} f &= [-1.8log(\frac{6.9}{Re_{d4}} + (\frac{\epsilon_4/d_4}{3.7})^1.11)]^{-2} \\ &= [-1.8log(\frac{6.9}{231770.32} + (\frac{5.227 \times 10^{-4}}{3.7})^1.11)]^{-2} \\ &= 0.018535 \approx 1.85 \times 10^{-2} \end{aligned} \tag{F.1.4}$$

Now the term on the right hand side of equation F.1.4 can be calculated with the known pipe geometry:

$$\begin{aligned} (\frac{\bar{f}L^*}{d})_{vo} &= \frac{\bar{f}\Delta L}{D} + (\frac{\bar{f}L^*}{d})_{pm} \\ &= \frac{0.018535(0.92)}{0.088} + 80.145 \\ &= 80.338 \end{aligned} \tag{F.1.4}$$

Equation F.1.4 is substituted back into equation F.1.4 and solved iteratively using the bisection method to obtain the Mach number at the volute outlet. The upper limit is set at $Ma_{max} = 0.5$ and the lower limit is set at $Ma_{min} = 1 \times 10^{-6}$ with the mid point determined by $Ma_{mid} = (Ma_{max} - Ma_{min})/2$ and is used as an initial value. The right hand side of equation F.1.4 is then solved until the error is less than 1×10^{-6}. The Mach number at the volute outlet is determined to be 0.092. Using compressible duct flow the absolute velocity at the volute outlet plane is calculated:

$$\frac{c}{c^*} = \frac{1}{Ma}[\frac{2 + (\gamma - 1)Ma^2}{\gamma + 1}]^0.5 \tag{F.1.4}$$

$$\begin{aligned} c_{vo} &= c_4 \frac{c_{vo}/c^*}{c_4/c^*} \\ &= 34.51 \frac{15.546}{15.512} \\ &= 34.59 \quad m/s \end{aligned} \tag{F.1.4}$$

Equation F.1.4 is substituted back into equation F.1.4 and iterated until the error is less than 1×10^{-6}. Once the solution has converged the static and

total conditions at the volute outlet is calculated from the critical ratios found from compressible duct flow theory (White, 2006). The final static and total conditions at the volute outlet were calculated as:

$$\begin{aligned} T_{s,vo} &= 351.39 \quad K \\ \rho_{4s} &= 1.447 \quad kg/m^3 \\ c_{vo} &= 34.59 \quad m/s \\ Ma_{vo} &= 0.92 \\ T_{t,vo} &= 351.98 \quad K \\ P_{t,vo} &= 147 \quad kPa \end{aligned} \tag{F.1.4}$$

Finally the total-to-static pressure ratio and total-to-total efficiency can be calculated:

$$\begin{aligned} PR_{t-s} &= \frac{P_{s,vo}}{P_{t1}} \\ &= \frac{147}{95.214} \\ &= 1.54 \end{aligned} \tag{F.1.4}$$

$$\begin{aligned} \eta_{t-t} &= [(\frac{P_{t,vo}}{P_{t1}})^{(\gamma-1)/\gamma} - 1][\frac{T_{t1}}{T_{t,vo} - T_{t1}}] \\ &= [(1.54)^{(0.39)/1.39} - 1][\frac{299.8}{351.39 - 299.8}] \\ &= 0.748 \end{aligned} \tag{F.1.4}$$

F.2 Sample Data

Table F.2: Sample Data of Cross-Over Diffuser with 0.2 mm Blade Tip Clearance at 50 000 rpm: Columns 1 - 5

P_{amb}	T_{amb}	$\dot{m}$	P_{01}	P_{02}
95,209451	297,419609	0,302038	98,575317	127,102365
95,209451	297,409286	0,302044	98,575317	127,102365
95,277015	297,464249	0,301871	98,519548	127,007598
95,277015	297,372772	0,301843	98,519548	127,007598
95,18226	297,350914	0,301987	98,602598	127,223335
95,18226	297,391922	0,301998	98,602598	127,223335
95,24955	297,429451	0,301873	98,54864	127,216355
95,24955	297,429459	0,301854	98,54864	127,216355
95,248039	297,354996	0,301757	98,61437	127,11451
95,248039	297,451347	0,301794	98,61437	127,11451
95,212609	297,344429	0,301737	98,649235	127,038294
95,212609	297,388458	0,301791	98,649235	127,038294
95,238014	297,418678	0,301585	98,63335	126,96313
95,238014	297,34671	0,301569	98,63335	126,96313
95,140514	297,424294	0,301725	98,607239	127,014578
95,140514	297,416275	0,301686	98,607239	127,014578
95,242821	297,401405	0,301659	98,565129	127,173417
95,242821	297,399117	0,301667	98,565129	127,173417
95,238701	297,479187	0,301582	98,471891	127,022037
95,238701	297,356903	0,301541	98,471891	127,022037
95,219476	297,340401	0,301641	98,657235	127,008745
95,219476	297,460609	0,301649	98,657235	127,008745
95,258064	297,400597	0,301518	98,475966	127,123977
95,258064	297,457336	0,301548	98,475966	127,123977
95,238426	297,349693	0,30152	98,557658	126,990193
95,238426	297,309334	0,301479	98,557658	126,990193
95,238426	297,418289	0,3015	98,557658	126,990193
95,195581	297,391762	0,301451	98,53649	127,017065
95,195581	297,369087	0,301464	98,53649	127,017065

Table F.3: Sample Data Continued: Columns 6 - 10

P_{03}	P_{04}	T_{01B1}	T_{01B2}	T_{01B3}
156,672025	145,960179	297,504578	297,49054	297,377167
156,672025	145,960179	297,506348	297,39151	297,423645
156,685248	145,918874	297,506287	297,437927	297,337128
156,685248	145,918874	297,46463	297,429565	297,381378
156,507266	145,72313	297,632507	297,493439	297,441132
156,507266	145,72313	297,52417	297,312347	297,367859
156,60439	145,787424	297,436523	297,3255	297,291901
156,60439	145,787424	297,599609	297,426636	297,396851
156,552926	145,901513	297,501038	297,428284	297,395844
156,552926	145,901513	297,59845	297,434845	297,456757
156,430308	145,71941	297,464813	297,331573	297,331879
156,430308	145,71941	297,424316	297,340454	297,258057
156,430308	145,71941	297,538025	297,392792	297,426971
156,409856	145,73162	297,584595	297,339752	297,292999
156,409856	145,73162	297,471649	297,408234	297,33374
156,608861	145,722749	297,465637	297,328888	297,327454
156,608861	145,722749	297,603882	297,307007	297,301758
156,528669	145,799634	297,599915	297,396271	297,33548
156,528669	145,799634	297,459473	297,365997	297,380005
156,539609	145,810604	297,374939	297,286987	297,301025
156,539609	145,810604	297,56781	297,387238	297,435181
156,545031	145,758997	297,452637	297,39566	297,351837
156,545031	145,758997	297,588104	297,41629	297,333893
156,509644	145,787615	297,488739	297,429718	297,353455
156,509644	145,787615	297,654785	297,431	297,413452
156,628742	145,657882	297,572021	297,397583	297,374786
156,628742	145,657882	297,586426	297,39505	297,42749
156,482818	145,687454	297,580963	297,456787	297,395416
56,482818	145,687454	297,565948	297,430359	297,442932
156,553117	145,798013	297,604706	297,396088	297,315155
156,553117	145,798013	297,602051	297,391663	297,396942
156,643868	145,715308	297,589722	297,4328	297,530701
156,643868	145,715308	297,592133	297,454224	297,454529
156,497753	145,607229	297,448181	297,450806	297,298004
156,497753	145,607229	297,463196	297,229431	297,356262
156,442675	145,745261	297,619995	297,317322	297,378662
156,442675	145,745261	297,48822	297,394745	297,39444
156,494233	145,659504	297,562256	297,462341	297,368835
156,494233	145,659504	297,545258	297,362366	297,331696
156,340984	145,617245	297,505615	297,370941	297,369171
156,340984	145,617245	297,483917	297,386322	297,389252
156,50641	145,665704	297,510895	297,330933	297,363953
156,50641	145,665704	297,693817	297,40863	297,408356
156,426027	145,516034	297,517609	297,373566	297,305786
156,426027	145,516034	297,502869	297,371094	297,291351
156,549882	145,714354	297,549866	297,352936	297,316986

Table F.4: Sample Data Continued: Columns 11 -16

T_{01B4}	T_{04CO1}	T_{04CO2}	T_{04CO3}	T_{04CO4}	dP
297,401703	348,228271	347,999451	1473,150024	347,838562	1,868491
297,362396	348,16684	347,983276	1473,150024	347,841736	1,868491
297,414062	348,193787	347,985443	1473,150024	347,905151	1,867705
297,258453	348,19812	347,931213	1473,150024	347,784119	1,867705
297,217682	348,108215	347,835571	1473,150024	347,778442	1,867336
297,386444	348,118317	347,845673	1473,150024	347,796844	1,867336
297,42807	348,231415	347,931061	1473,150024	347,881958	1,867242
297,273224	348,186188	347,980743	1473,150024	347,905426	1,867242
297,240173	348,134979	347,915314	1473,150024	347,784241	1,86599
297,428772	348,239136	347,960724	1473,150024	347,883453	1,86599
297,273499	348,10437	347,910919	1473,150024	347,80249	1,865479
297,317383	348,132294	347,994049	1473,150024	347,867645	1,865479
297,325317	348,184601	347,999054	1473,150024	347,864685	1,864883
297,318878	348,138947	347,874603	1473,150024	347,785187	1,864883
297,32489	348,182465	347,938477	1473,150024	347,863434	1,864506
297,343597	348,236176	348,010803	1473,150024	347,795563	1,864506
297,32428	348,140167	347,945618	1473,150024	347,833313	1,863996
297,320892	348,221069	347,901031	1473,150024	347,78183	1,863996
297,34967	348,275482	347,977081	1473,150024	347,932373	1,8637
297,223236	348,202454	347,972168	1473,150024	347,827026	1,8637
297,307678	348,1586	347,980164	1473,150024	347,870331	1,863015
297,419342	348,210388	347,930542	1473,150024	347,874268	1,863015
297,277222	348,216461	347,971008	1473,150024	347,928497	1,862741
297,339294	348,241302	348,08316	1473,150024	347,89386	1,862741
297,270508	348,162781	347,915283	1473,150024	347,813721	1,862249
297,214508	348,151337	347,974701	1473,150024	347,739319	1,862249
297,315369	348,138672	347,949097	1473,150024	347,874023	1,862249
297,349701	348,117279	347,938751	1473,150024	347,902039	1,861916
297,262726	348,196899	347,892487	1473,150024	347,825439	1,861916
297,200348	348,182953	347,924622	1473,150024	347,790497	1,861097
297,25589	348,157959	347,989227	1473,150024	347,890442	1,861097
297,188538	348,266327	347,967804	1473,150024	347,835907	1,860434
297,381195	348,189392	347,923767	1473,150024	347,872711	1,860434
297,234711	348,142517	347,96701	1473,150024	347,823792	1,859821
297,415894	348,277893	348,032166	1473,150024	347,939148	1,859821
297,287842	348,130615	347,977753	1473,150024	347,851349	1,859145
297,392914	348,246826	348,005493	1473,150024	347,892639	1,859145
297,352875	348,127991	347,979523	1473,150024	347,861694	1,858904
297,338379	348,237885	348,04007	1473,150024	347,87146	1,858904
297,3479	348,194519	348,045227	1473,150024	347,91333	1,858374
297,416656	348,263184	348,053589	1473,150024	348,022125	1,858374
297,367676	348,243317	348,017792	1473,150024	347,883698	1,858025
297,32489	348,173767	348,02597	1473,150024	347,934357	1,858025
297,327728	348,227936	348,026428	1473,150024	347,952484	1,857439
297,330597	348,188263	348,035217	1473,150024	347,887878	1,857439
297,396301	348,308258	348,082642	1473,150024	347,929749	1,857144
297,487244	348,286987	348,049347	1473,150024	347,917145	1,857144

Appendix G

MATLAB Coding for Data Processing

MATLAB was used to do all the calculations that were needed to process the experimental results. The code can be found below.

```
function [PR_ts2, PR_ts3, PR_tt3, PR_ts4, PR_tt, eta_tt, eta_tt3, mdot2, N]
 = Quantities( C10kR )

%------------------------------------------------------------------------%
% Editor:       PC Swanepoel
%               16622766
%               M.Eng Research Student
%
% Thesis Title: The Experimental Evaluation of a Mixed-Flow Compressor
%               Impeller and Cross-Over Diffuser.
%
% Purpose:      Simplified processing of the Compressor Test Bench Data
%------------------------------------------------------------------------%

% Declaration of Variables
i = 1;
k = 1;
count = 0;
err = 1;
count2 = 0;
err2 = 1;


% Variables for Pressure Measurement Station
rho_amb(1:5,:) = 0;
V_bm(1:5,:) = 0;
```

```
Re_bm(1:5,:) = 0;
Cd(1:5,:) = 0;
mdot(1:5,:) = 0;
Cp_4(1:5,:) = 0;
gamma_4(1:5,:) = 0;
rho_4(1:5,:) = 0;
C_4(1:5,:) = 0;
Ma_4(1:5,:) = 0;
T_t4(1:5,:) = 0;
T_s4_new(1:5,:) = 0;


% Decleration of Constants
R_g = 287;                      % J/kg.K      Universal Gas Constant
M_air = 28.96;                   % kg/mol      Molar Weight of Dry Air
S = 110.4;                       % K           Sutherland temperature for Air
T_o = 297;                       % K           Reference temperature for air
mu_Ref_air = 1.71*10^(-5);       % kg/s.m      Reference Viscosity of air
mu_air = 1.8*10^(-5);            % kg/s.m      Viscosity of Air
C_p = 1005;                      % J/kg.K      Specific heat @ constant pressure
gamma = 1.4;                     %             Ratio of Specif Heats
K = 0.96;                        %             Temperature Probe, Dynamic
 Correction factor
L_1 = 1;                         %             Discharge Coefficient Parameters
L_2 = 0.47;                      %             Discharge Coefficient Parameters

% Specific Heat Constants
a = 28.11;
b = 0.1967e-2;
c = 0.4082e-5;
d2 = -1.966e-9;

% Physical Dimensions of Test Setup
d = 77.3*10^(-3);                  % m         Bellmouth outlet Diameter

% Static pressure measurement station
L_4 = 0.92;                        % m         Pipe Length
d_4 = 0.088;                       % m         Pipe Internal Diameter
%d_4 = 0.058;
A_4 = (pi)*(d_4/2)^2;              % m^2       Pipe Internal Cross-sectional Area
Eps_4 = 0.046*10^(-3);             % m         Pipe internal Surface roughness
%A_4 = 4.94e-3
% ---------------Processing Compressor Exerimental Data-----------------%
% -----Calculation of Points 1 - 5 on Compressor Performance curve------%
```

```
%-------------------------------------------------------------------------%

for i = 1:5

%-------------------------------------------------------------------------%
%------------Average Quantities from Experimental Data--------------%
%-------------------------------------------------------------------------%

% Properties assigned for 10 kRPM and calibrated simultaniously
P_amb(i,:) = C10kR(i,1);
            % Ambient Pressure [kPa]
T_amb(i,:) = C10kR(i,2);
            % Ambient Temperature [K]
dP(i,:) = (0.9985*C10kR(i,16)*1000) + 0.0027;
% Differential Pressure [Pa]
P_s2(i,:) = 0.9974*C10kR(i,5) + 0.1308;
% Compressor Pressure Outlet [kPa]
%P_s3(i,:) = 0.9992*C10kR(i,6) - 3.9681;
P_s3(i,:) = 1.0069*C10kR(i,6) - 2.4834;
% Diffuser Outlet
P_s4(i,:) = 1.0017*C10kR(i,7) + 0.2119;
% Compressor Pressure Outlet [kPa]
T_t1(i,:) = 1.0076*(mean(C10kR(i,8:11),2)) +0.1474;
% Compressor inlet total temperature - From Bellmouth [K]
T_p5(i,:) = 1.0101*((mean(C10kR(i,12:13),2) + C10kR(i,15))/2) + 0.4723;
% Compressor outlet probe temperature [K]


end

%-------------------------------------------------------------------------%
%-----------Calculation of New Static and Total Quantities-----------%
%-------------------------------------------------------------------------%

for k = 1:5

% Calculations for 10 kRPM
rho_amb(k,:) = P_amb(k,:)/((R_g/1000)*T_amb(k,:));
% Ambient Density [kg/m^3]
V_bm(k,:) = ((2*dP(k,:))/(rho_amb(k,:)))^0.5;
% Bellmouth Velocity [m/s]
Re_bm(k,:) = (V_bm(k,:)*rho_amb(k,:)*d)/mu_air;
% Reynolds Number at Bellmouth
Cd(k,:) = exp((-1500)/Re_bm(k,:));
```

```
% Coeficient of Discharge
mdot(k,:) = Cd(k,:)*(pi/4)*(d^2)*sqrt(2*(dP(k,:))*rho_amb(k,:));
% Mass flow rate [kg/s]
mdot2(k,:) = mdot(k,:)*(sqrt(T_amb(k,:))/(P_amb(k,:)));

% T_s4 = T_p5
% Calculating initial static conditions at Pressure measurment station
% /Station Point 4

err = 1;
j = 1;
T_s4_10(1) = T_p5(k,:);

% Initialise variables
Cp_4(1) = (a + b*T_s4_10(1) + c*(T_s4_10(1))^2
+ d2*(T_s4_10(1))^3)/(M_air/1000);
% Constant Speific Heat @ point 4 [J/kg.K]
gamma_4(1) = Cp_4(1)/(Cp_4(1) - R_g);
% Ratio of specific heats
rho_4(1) = P_s4(k,:)/((R_g/1000)*T_s4_10(j));
% Density @ Point 4 [kg/m^3]
C_4(1) = mdot(k,:)./(rho_4(j).*A_4);
% Absolute Gas Velocity [m/s]
Ma_4(1) = C_4(j)/sqrt(gamma_4(j)*T_s4_10(j)*R_g);      % Mach Number
T_t4(1) = T_s4_10(j) + ((1-K)*C_4(j)^2)/(2*Cp_4(j));
% Total temperature @ point 4 [K]

% Iterate until correct value is found
while err(j) > (1*10^-6)

Cp_4(j+1) = (a + b*T_s4_10(j) + c*(T_s4_10(j))^2
+ d2*(T_s4_10(j))^3)/(M_air/1000);
% Constant Speific Heat @ point 4 [J/kg.K]
gamma_4(j+1) = Cp_4(j)/(Cp_4(j) - R_g);
% Ratio of specific heats
rho_4(j+1) = P_s4(k,:)/((R_g/1000)*T_s4_10(j));
% Density @ Point 4 [kg/m^3]
C_4(j+1) = mdot(k,:)./(rho_4(j).*A_4);
% Absolute Gas Velocity [m/s]
Ma_4(j+1) = C_4(j)/sqrt(gamma_4(j)*T_s4_10(j)*R_g);
% Mach Number
T_t4(j+1) = T_s4_10(j) + ((1-K)*C_4(j)^2)/(2*Cp_4(j));
 % Total temperature @ point 4 [K]
T_s4_10(j+1) = T_t4(j)/(1+(((gamma_4(j)-1)*Ma_4(j)^2)/2));
```

```
% New Static Temperature [K]

err(j+1) = abs(T_s4_10(j+1) - T_s4_10(j));
j = j+1;
count = count +1;

end

T_s4_new(k,:) = T_s4_10(j);
Cp_4_new(k,:) = Cp_4(j);
gamma_4_new(k,:) = gamma_4(j);
rho_4_new(k,:) = rho_4(j);
C_4_new(k,:) = C_4(j);
Ma_4_new(k,:) = Ma_4(j);
T_t4_new(k,:) = T_t4(j);
T_s4_new(k,:) = T_s4_10(j);

% Total Pressure [kPa]
P_t4(k,:) = P_s4(k,:)*(1+(((gamma_4_new(k,:)-1)*(Ma_4_new(k,:)^2))/2))
^(gamma_4_new(k,:)/(gamma_4_new(k,:)-1));

% Assuming minimal temperature loss from point 3 to point 4
% It is assumed that T_s4 = T_s3 and thus that the Ratio used for
% calculating Point 4 total pressure can be used for Point 3
% total pressure?

P_t3(k,:) = P_s3(k,:)*(1+(((gamma_4_new(k,:)-1)*(Ma_4_new(k,:)^2))/2))
^(gamma_4_new(k,:)/(gamma_4_new(k,:)-1));


% /Use total conditions to calculate the Mach number at the volute exit
% /at the pressure measurement station.

fld_pm(k,:) = ((1-(Ma_4_new(k,:)^2))/(gamma_4_new(k,:)*(Ma_4_new(k,:)^2)))
+((gamma_4_new(k,:)+1)/(2*gamma_4_new(k,:)))*log(((gamma_4_new(k,:)+1)
*(Ma_4_new(k,:)^2))/(2+(gamma_4_new(k,:)-1)*(Ma_4_new(k,:)^2)));
mu_4(k,:) = mu_Ref_air*((T_s4_new(k,:)/T_o)^(3/2))*((T_o + S)
/(T_s4_new(k,:) + S));    % Dynamic visosity of air

%-------------------------------------------------------------------------%
%-Iteration Process for final results-----------------------------------%
%-------------------------------------------------------------------------%

err2 = 1;
```

```
l = 1;

Re_d4(l) = (rho_4_new(k,:)*C_4_new(k,:)*d_4)/mu_4(k,:);       % Reynolds number

% Using the explicit formula, the friction factor is calculated
f_10(l) = (-1.8*log10((6.9/Re_d4(l))+((Eps_4/d_4)/3.7)^1.11))^-2;
fld_known = (f_10(l)*L_4)/d_4;
fld_vo(l) = fld_known + fld_pm(l);

tr = @(Ma_10) (((1-(Ma_10.^2))./(gamma_4_new(k,:).*(Ma_10.^2)))
+ ((gamma_4_new(k,:)+1)./(2.*gamma_4_new(k,:))).
*log(((gamma_4_new(k,:)+1).*(Ma_10.^2)).
/(2+(gamma_4_new(k,:)-1).*(Ma_10.^2))))/fld_vo(l);
Ma_discov_10 = bisection(tr, 1e-6, 0.5, 1e-6);

if Ma_discov_10 == 'Error'

Ma_vo_10(l) = Ma_4_new(k,:);

else

Ma_vo_10(l) = Ma_discov_10;

end

Cvo_Cstr(l) = (1/Ma_vo_10(l))*(((2+(gamma_4_new(k,:)-1)*(Ma_vo_10(l)^2))
/(gamma_4_new(k,:)+1))^0.5);
C4_Cstr(l) = (1/Ma_4_new(k,:))*(((2+(gamma_4_new(k,:)-1)*(Ma_4_new(k,:)^2))
/(gamma_4_new(k,:)+1))^0.5);
C_vo(l) = C_4_new(k,:)*(Cvo_Cstr(l)/C4_Cstr(l));

while err2(l) > (1*10^-6)

Re_d4(l+1) = (rho_4_new(k,:)*C_vo(l)*d_4)/mu_4(k,:);       % Reynolds number
gamma_4_vo_10(l) = gamma_4_new(k,:);
% Using the explicit formula, the friction factor is calculated
f_10(l+1) = (-1.8*log10((6.9/Re_d4(l))+((Eps_4/d_4)/3.7)^1.11))^-2;
fld_known = (f_10(l)*L_4)/d_4;
fld_vo(l+1) = fld_known + fld_pm(k,:);

tr = @(Ma_10) (((1-(Ma_10.^2))./(gamma_4_vo_10(l).*(Ma_10.^2)))
+ ((gamma_4_vo_10(l)+1)./(2.*gamma_4_vo_10(l))).
*log(((gamma_4_vo_10(l)+1).*(Ma_10.^2)).
/(2+(gamma_4_vo_10(l)-1).*(Ma_10.^2))))/fld_vo(l);
```

```
Ma_discov_10 = bisection(tr, 1e-6, 0.5, 1e-6);

if Ma_discov_10 == 'Error'

Ma_vo_10(l+1) = Ma_4_new(k,:);

else

Ma_vo_10(l+1) = Ma_discov_10;

end

Cvo_Cstr(l+1) = (1/Ma_vo_10(l))*(((2+(gamma_4_new(k,:)-1)*(Ma_vo_10(l)^2))
/(gamma_4_new(k,:)+1))^0.5);
C4_Cstr(l+1) = (1/Ma_4_new(k,:))*(((2+(gamma_4_new(k,:)-1)*(Ma_4_new(k,:)^2))
/(gamma_4_new(k,:)+1))^0.5);
C_vo(l+1) = C_vo(l)*(Cvo_Cstr(l)/C4_Cstr(l));

err2(l+1) = abs(C_vo(l+1) - C_vo(l));
l = l+1;
count2 = count2 +1;

end

Re_d4_new(k,:) = Re_d4(l);
f_new(k,:) = f_10(l);
fld_vo_new(k,:) = fld_vo(l);
Ma_vo_new(k,:) = Ma_vo_10(l);
C_vo_new(k,:) = C_vo(l);

PR_ts2(k,:) = P_s2(k,:)/P_amb(k,:);
PR_ts3(k,:) = P_s3(k,:)/P_amb(k,:);
PR_tt3(k,:) = P_t3(k,:)/P_amb(k,:);
PR_ts4(k,:) = P_s4(k,:)/P_amb(k,:);
PR_tt(k,:) = P_t4(k,:)/P_amb(k,:);
eta_tt(k,:) = (((P_t4(k,:)/P_amb(k,:))^((gamma_4_new(k,:)-1)
/gamma_4_new(k,:))-1))*(T_t1(k,:)
/(T_t4_new(k,:)-T_t1(k,:)));
eta_tt3(k,:) = (((P_t3(k,:)/P_amb(k,:))^((gamma_4_new(k,:)-1)
/gamma_4_new(k,:))-1))*(T_t1(k,:)
/(T_s4_new(k,:)-T_t1(k,:)));
N(k,:) = 50/sqrt(T_amb);
end
```

Appendix H

Test bench Operating Procedure

The following set of instructions are given by Struwig (2014) and adapted as a strictly-to-follow guideline to prevent harm to any person operating the test bench or to the components of the test bench itself.

Test Briefing

1. Ear protection should be worn for the duration of the test procedure.
2. Check the integrity of all the pressure connections and tubing.
3. Ensure that all instrumentation is connected (Fibre connection to PC is still connected to DAQ).
4. Switch on power supply to DAQ and lubrication system.
5. Check that the telemetry readings on the UI are correct (Temperature, pressure and speed). Small amount of value jumping is normal, values should not be negative.
6. Ensure that all the valves upstream of the turbine are closed, primary header ball valve, secondary safety valve and flow control butterfly valve.
7. Open throttle valve downstream of compressor fully.
8. Set the oil heater thermostat to 60 ^oC and switch on lubrication system with the bypass valve open to allow the oil to circulate bypassing the compressor test bench while heating up. (This is to prevent the oil from burning while heating up.)
9. Keep oil flow rate at 0.5 l/min and at a pressure of 100 kPa to ensure there is no strain on the oil filter and on the bearing once the bypass valve is closed. The low pressure also limits the amount of oil leakage into the impeller and turbine section of the test bench.

10. Once oil temperature has stabilised, close the bypass valve to allow the oil to lubricate and heat up the compressor test bench.
11. Open the primary valve.
12. Open the secondary valve.
13. Slowly open butterfly flow control valve, until compressor starts rotating and check whether speed is being measured. Once speed measurement is confirmed continue increasing speed to 20 000 rpm.
14. Idle compressor at 20 000 rpm for 5 min to ensure all components are functioning correctly.
15. Increase speed to 30 000 rpm and idle for 5 min again ensuring all components are functioning correctly.
16. Increase speed to 40 000 rpm and idle for 10 min to ensure integrity of test bench and heat soak of temperature probes.
17. Decrease speed to 0 rpm to allow air receiver to refill.
18. Once the air receiver is full, increase the speed to 30 000 rpm for 1 min.
19. Increase speed to 40 000 rpm for 1 min.
20. Increase speed to 50 000 rpm to commence testing of impeller and diffusers.
21. Decrease speed once 5-7 test points were taken or if receiver has reached 600 - 500 kPa and allow for receiver to refill.

Test Debriefing

1. Decrease speed to 20 000 rpm and keep idle.
2. Shut the primary valve.
3. Allow remaining air to discharge through the turbine.
4. Once all the air has discharged, close secondary ball valve and butterfly control valve.
5. Open the throttle valve downstream of the compressor fully.
6. Switch off oil thermostat.
7. Open oil bypass valve to bypass test bench again.
8. Switch off lubrication system.

9. Ensure data samples are correct and good condition.
10. Switch of DAQ and lubrication system power supply. (Only necessary after final tests).

List of References

(2004). *Application of a Multipoint Optimization to the Design of Turbomachinery Blades*, 1. American Society of Mechanical Engineers, ASME Turbo Expo.

arduinoprojects101 (2018).
Available at: `www.instructables.com/id/Arduino-Based-Optical-Tachometer/`

Aungier, R. (2000). Centrifugal compressors: a strategy for aerodynamic design and analysis. *ASME*.

Benedict, R. (1977). *Fundamentals of Temperature, Pressure and Flow Measurements*. 2nd edn. John Wiley & Sons, Inc., Philadelphia.

Brun, K. and Nored, M. (2006 August). *Guideline for field testing of Gas Turbine and Centrifugal Compressor Performance*. Guideline Release 2.0.

Burger, C. (2016). *Design procedure of a Compact Aerodynamic Crossover Diffuser for Micro Gas Turbine application*. Master's thesis, Stellenbosch University.

Cengel, Y.A. and Boles, M.A. (2006). *Thermodynamics: An Engineering Approach*. 5th edn. McGraw-Hill.

Danish, S.N. (ed.) (2006 August). *The Influence of Tip Clearance on Centrifugal Compressor Stage of a Turbocharger*, 4. School of Mechanical and Vehicular Engineering, Beijing Institute of Technology.

Diener, O. (2016 jun). *Multi-Disciplinary Optimization of a Mixed-Flow Compressor Impeller*. Master's thesis, Department of Mechanical and Mechatronic Engineering, University of Stellenbosch.

Dixon, S. (2005). *Fluid Mechanics and Thermodynamics of Turbomachinery*. 5th edn. Elsevier Butterworth-Heinemann. ISBN 0-7506-7870-4.

Hall, N. (2015 May). Turbine thermodynamics.
Available at: `https://www.grc.nasa.gov/www/k-12/airplane/powtrbth.html`

Japikse, D. and Baines, N. (1994). *Introduction to Turbomachinery*. NREC.

Kock, P. (2016 April). *Optimization of a Vane Guided Diffuser*. Master's thesis, Faculty of Mechanical Engineering at Stellenbosch University.

Menter (1992). Performance of popular turbulence model for attached and separated adverse pressure gradient flow. *AAIA Journal*, vol. 30, no. 8, pp. 2066–2072.

Niewoudt, A. (1987). Turbo-aanjaer toetsbank. Tech. Rep., University of Stellenbosch.

NUMECA (2014a). *NUMECA Fine/Turbo v10.1 User Manual*. NUMECA International.

NUMECA (2014b). *AutoGrid5v9*. NUMECA International.

Pandurangadu, V. (2014 January). Tip clearance effects on perfomance of a centrifugal compressor. *International Journal of Scientific and Engineering Research*, vol. 5, no. 1, pp. 1027 – 1034.

Reneau, L., Johnston, J. and Kline, S. (1967). Performance of straight, two-dimensional diffusers. *Journal of Basic Engineering*, vol. 89, no. 1, pp. 141–150.

Simpson (2012). Desin and testing of multistage centrifugal compressor with small diffusion ratios. *Journal of Turbomachinery*, vol. 134, no. 1, pp. 1–8.

Struwig, D.J. (2014 April). *The Development and Verification of a Centrifugal Compressor Test Bench*. Master's thesis, Faculty of Mechanical Engineering at Stellenbosch University.

Thomas, K. (2016 June). *180kW Compressor Assembly Procedure*. University of Stellenbosch, Department of Mechanical and Mechatronic Engineering, University of Stellenbosch, Private Bag X1, Matieland 7602, South Africa., 1st edn.

Versteeg, H. and Malalasekera, W. (2007). *An Introduction to Computational Fluid dynamics: The Finite Volume Method*. Pearson Education.

Vick, A Heyes, K.P. (ed.) (2009). *Design Overview of a Three-Kilowatt Recuperated Ceramic Turboshaft Engine*. American Society of Mechanical Engineers, ASME Turbo Expo 2009: Power for Land, Sea and Air.

Warming, R. and Beam, R.M. (1976). Upwind second-order difference schemes and applications in aerodynamic flows. *AAIA Journal*, vol. 14, no. 9, pp. 1241–1249.

White, F. (2006). *Fluid Mechanics*. 6th edn. McGraw-Hill.